# Effect of reduced gravity and weightlessness on vapor bubble dynamics and heat transfer in boiling liquid

K. V. Rusanov and N. S. Shcherbakova

*B. Verkin Institute for Low Temperature Physics and Engineering, National Academy of Sciences of the Ukraine, Ukraine, 310164, Kharkov, 47 Lenin Ave*
Fiz. Nizk. Temp. **24**, 140–142 (February 1998)

The results on boiling of liquids and gas bubbling under simulated long-term reduced gravity are reported. The possibility of extrapolating these results to the real spacecraft conditions is considered and the program of on-board space experiments is proposed to test the current theory at the relative accelerations $10^{-4}$–$10^{-6}$ which are unattainable in a laboratory. Tests in free-fall towers, in aircraft, or in ballistic rockets are inadequate since only prolonged (over one hour) experiments in the Earth's orbit can provide reliable data. The advantage of cryogenic liquids, helium, in particular, in space experiments is discussed. © *1998 American Institute of Physics.* [S1063-777X(98)01002-0]

## INTRODUCTION

In the orbit some processes occur in the vapor-liquid and gas-liquid systems, which are related to heat transfer and to the formation and motion of bubbles and drops. The influence of microgravity on the processes in tanks and pipelines with liquid fuel for rocket engines or in various boilers-condensers attracted keen interest in the 1950s and 1960s when practical space exploration advanced quickly.[1]

High costs of space experiments, however, called for various methods of simulation of reduced gravity. Many of them (in ballistic rockets, aircraft, free fall towers) were still expensive and permitted only short-term simulation of microgravity. Low-cost methods of long-term laboratory simulation of microgravity for vapor-liquid and gas-liquid systems were developed at the Special Research and Development Bureau (Institute of Low Temperature Physis and Engineering). They are applicable at relative accelerations $\eta = 1 - 10^{-2}$. One of them involves compensation of weight force that acts on liquid oxygen by a nonuniform magnetic field and the other uses the weight force decomposition in inclined thin containers.[2]

Extensive studies of the effect of reduced gravity on heat transfer and boiling in liquids (including liquid oxygen) were performed. The results and conclusions were employed in Soviet space vehicles and partially (but insufficiently) tested in on-board experiments in the beginning of the 1970s. There are still some questions concerning extrapolation of these conclusions to lower relative accelerations ($\eta = 10^{-4} - 10^{-6}$). This region is realizable only in long-term orbital flights and cannot be simulated by other methods. Laboratory results should therefore be tested in orbital experiments. Such experiments have never been performed either in the USSR or (as far as we know) in other ''space-exploring'' countries, despite the advent of numerous on-board cryogenic-cooled instruments (e.g., IR telescopes) and a wide use of cryogenic liquids for experiments in the 1980s and 1990s. Researchers plunged into fundamentals of physics of low-temperature liquids under microgravity. We shall try to show that now, with large liquid-helium cryostats frequently sent into orbit, the time is right to complete the long-standing work and to answer the questions which are still open.

## LABORATORY RESULTS FOR $\eta = 1 - 10^{-2}$

The experimental objects were the growth, departure, and motion of vapor or gas bubbles, heat transfer coefficient $\alpha$ under nucleate and film boiling, and critical heat flux densities $q_{cr}$ in liquid oxygen, water, and organic liquids.[2] The true range of $\eta$-values was $1 - 10^{-2}$ and the highest simulation error was $\pm 10^{-2}$. Oxygen boiled on platinum wires (0.05–0.15 mm in diameter); water and organic liquids also boiled at the edge of a steel tape 0.1 mm wide. Pressure varied in the range 6–700 kPa. The gas (helium or nitrogen) bubbled into liquid through orifices of various sizes. Rapid filming technique (30 000 frames per sec.) was used to investigate the bubble dynamics.

Experimental results were presented as exponential $\eta$-functions of corresponding quantities.[2] The bubble departure diameter $D$ was $D(\eta)/D(1) = \eta^k$, where $k = -0.33$ at the atmospheric pressure, and $k = -0.23$ and $-0.31$ under reduced and elevated pressures, respectively. For the bubble departure frequency at these pressures the $k$-values were 0.67, 0.57, 0.63, respectively.

The dependence of the velocity of the bubbles is described as $w(\eta)/w(1) = \eta^{0.33}$.

The dependence on $\eta$ of heat flux density $q_{cr}^k$ corresponding to the nucleate film boiling transition is influenced greatly by pressure; the $k$ values are 0.36, 0.26, and only 0.05 under elevated, atmospheric, and reduced pressures, respectively. During film boiling $\alpha(\eta)/\alpha(1) = \eta^{0.18}$. During nucleate boiling the dependence of the heat transfer on the relative acceleration, in contrast, was weak: $k = -0.05$ at the atmospheric pressure and $k = -0.01$ under lower pressures. Nucleate boiling under elevated pressure deteriorated the heat transfer as $\alpha$ decreased with increasing growing heat flux density $q$.

Larger scattering and uncertainty are observed in the $k$ values on approaching the lower boundary of the simulated relative acceleration range. This occurs as the ''infinite-heater-in-infinite-liquid'' condition is violated at small $\eta$ val-

ues when bubble sizes become comparable with the volume of the liquid in the experimental cell and exceed the heater size. Simultaneously, the bubble growth at the heater takes more time and considerably prolongs the characteristic times of the transition process that occurs at the beginning of the experiment. To check the above formulas, we must increase the size of the cell and the heater and the time constant of the experiment at small $\eta$ values in order to match the bubble size and the growth times. It is obvious that these requirements are even more severe at $\eta=10^{-4}-10^{-6}$. In boiling water at $\eta=1$ the bubble diameter is $D=2.5$ mm; at $\eta=10^{-6}$ it increases to 250 mm. The characteristic growth time $\tau$ increases 10 000-fold.

## THE ADVANTAGE OF USING LIQUID HELIUM FOR ON-BOARD MICROGRAVITY EXPERIMENTS

To study boiling at $\eta=10^{-4}-10^{-6}$, we should choose the liquid with the lowest $D$ and $\tau$ under standard conditions, i.e., liquid helium-I with $D=0.05-0.1$ mm and $\tau\cong 0.003$ s at $\eta=1$ and atmospheric pressure.[3] Since on-board sources are limited in power, it is important that among cryogenic liquids helium has the lowest characteristic heat flux densities (cf. the standard values $q_{cr}\cong 10\,000$ W/m$^2$ for helium and $q_{cr}\cong 1\,000\,000$ W/m$^2$ for water). The lowest values of the characteristic times, sizes, and thermal power of helium are due to its low viscosity, surface tension, and latent heat of vaporization.

The ideal capability of liquid helium to wet any solid and the low surface tension ensure the slightest distortion of the free surface of the liquid under microgravity and hence the smallest change in pressure when the amount of the vapor in the liquid increases. The low density of liquid helium (as compared to water) partially counterbalances the cryostat mass (if the volume of the liquid in the on-board experiment is large).

Vaporized helium is safe for the spacecraft crew: it is nontoxic for breathing, noncombustible, and nonexplosive. As a result, on-board experiments do not need special safety systems.

## POSSIBLE EXPERIMENTS ON LIQUID HELIUM BOILING AND BUBBLING UNDER MICROGRAVITY

The main goal of the experiments proposed is an accurate test of the relations derived for bubble dynamics and heat transfer characteristics during boiling under microgravity simulated in the laboratory with $\eta=10^{-4}-10^{-6}$. The size (volume) and time scales of the experiment must be held consistent with the expected size of the bubble and the time of its growth under microgravity in order to keep the ''infinite-heater-in-infinite-liquid'' condition undisturbed.

The research program may include the following on-board experiments:

1. Videorecording of helium gas (vapor) bubbling into liquid through orifices of various diameters at various velocities.

2. Videorecording of active vapor nucleation sites (especially the homogeneous sites) in heated liquid helium; bubble growth, departure and motion during nucleate and film boiling.

3. Temperature measurement in the liquid and of the solid heating surface at various heat flux densities, including stable and transient states of the ''liquid-heater'' system. It is desirable to use several heating surfaces that differ appreciably in thermal conductivities and roughness since these factors control extensively the bubble nucleation and growth at the heater.

4. Pressure measurement in the liquid to study acoustic waves generated by nucleation and growth of the vapor phase.

The on-board helium cryostat with the experimental cell submerged in liquid helium must be equipped with an optical image output system (through a window or a fiberguide). The electric heater of the cell should have three or four surfaces of boiling with the characteristic size no smaller than 100 mm ($>10D$ at $\eta=10^{-6}$). Our estimation of the total heater operation time is 1.5 h. With the mean heat flux of $10^2$ W/m$^2$ ($0.5\,q_{cr}$ at $\eta=10^{-6}$) the total heat input in the liquid during the experiment is then about 25 kJ and the volume of evaporated liquid helium is about 10 liters.

The total liquid helium volume in the cryostat must be about 100 liters to keep the conditions invariable during the whole experimental period. Liquid helium cryostats of this (and larger) capacity have been developed and used in some experimental projects on-board a space shuttle.

Important elements used to mount the experimental heater in the cryostat include a special suspension damping small vibrations and a high-sensitivity, three-axial accelerometer.

In conclusion, we note that the program proposed will advance our understanding of physics of boiling and will be helpful in solving certain applied problems of on-board experiments. For example, it is known that bubble-generated acoustic waves in the liquid-cooled, high-sensitivity detectors (infra red., magnetic, etc.) carry considerable noise in the signals. Reliable information about the spectrum of boiling under microgravity will permit researchers to filter out the noise.

[1] R. Siegel, Adv. Heat Transfer **4**, 162 (1970).
[2] B. I. Verkin, Yu. A. Kirichenko, and K. V. Rusanov, *Boiling Heat Transfer in the Mass Force Fields of Various Intensity*, Naukova Dumka, Kiev (1988).
[3] Yu. A. Kirichenko and K. V. Rusanov, *Heat Transfer in a Liquid-Helium*, Naukova Dumka, Kiev (1983).

This article was published in English in the original journal. It was edited by S. J. Amoretty.

# Detection of absolute rotation using superfluid $^4$He

K. Schwab

*California Institute of Technology, Pasadena CA 91125, USA*

N. Bruckner and R. Packard

*Physics Department, University of California, Berkeley CA 94720, USA**
Fiz. Nizk. Temp. **24**, 143–146 (February 1998)

We have developed the superfluid analog of the superconducting rf SQUID. Such a device is a quantum mechanically based, absolute gyroscope and has been used to sense the rotation of the Earth. Our device is fabricated using silicon processing techniques and forms a planer sensing loop of superfluid helium which couples to the applied rotation. A much more sensitive superfluid gyroscope based on the principle's demonstrated with this device, might ultimately be used to detect the precession of our local inertial frame with respect to the fixed stars by the gravitomagnetic field of the rotating Earth. We compare the superfluid gyroscope against two other experiments aimed at detecting this general relativistic effect.  [S1063-777X(98)01102-5]

## INTRODUCTION

It has long been appreciated that superfluid $^4$He could be used as a reference to an absolute inertial frame.[1–3] In this paper we outline how we exploit the quantum properties of superfluid $^4$He to construct an absolute gyroscope, discuss the recent success in observing the rotation of the Earth using a device which behaves similarly to an rf SQUID,[4–6] and discuss the possibility of using a much improved superfluid gyroscope to observe the Lense-Thirring Effect of the rotating Earth.

## CIRCULATION QUANTIZATION IN SUPERFLUIDS

Here we show that if a Schrödinger-like equation of motion is assumed for the macroscopic order parameter of a superfluid, one concludes that circulation is quantized in units of $\kappa_0$ in the local inertial frame, where $\kappa_0 = h/m_4$ and $m_4$ is the bare mass of the helium atom. Anandan[7] gives an elementary argument where one begins with the Gross-Pitaevsky equation for the superfluid order parameter $\Psi(r,t)$:

$$i\hbar \frac{\partial \Psi}{\partial t} = -\frac{\hbar^2}{2m_4}\nabla^2\Psi + V\Psi + g|\Psi|^2\Psi, \tag{1}$$

where $g$ is the strength of the self interactions of the superfluid and $V$ is from external potentials. We assume this to be true in the local inertial frame. In the usual way, if we evaluate the time derivative of this equation and of the complex conjugate equation, we can identify a continuity equation and a mass current density operator:

$$\frac{\partial}{\partial t}(\Psi^*\Psi) + \nabla\cdot\left[\frac{\hbar}{2im_4}(\Psi^*\nabla\Psi - \Psi\nabla\Psi^*)\right] = 0, \tag{2}$$

where we interpret the term on the left hand side to be the time derivative of the superfluid density, $\Psi^*\Psi$, and the next term to the divergence of the superfluid mass current. If we assume a stationary wave function of the form $\Psi(\mathbf{r},t) = \Psi_0(\mathbf{r})\exp(-iEt/\hbar)$, where $E$ is a constant and $\Psi_0 = \sqrt{\rho}\exp(i\varphi)$, then the current operator becomes

$$j = \frac{\hbar}{2im_4}(\Psi^*\nabla\Psi - \Psi\nabla\Psi^*) = \rho\frac{\hbar}{m_4}\nabla\varphi. \tag{3}$$

Thus the superfluid velocity is $v_s = (\hbar/m_4)\nabla\varphi$. If we evaluate the path integral of the velocity around a closed contour, we find

$$\oint \mathbf{v}\cdot\mathbf{dl} = \frac{\hbar}{m_4}\oint \nabla\varphi\cdot\mathbf{dl} = \frac{\hbar}{m_4}2\pi n = n\kappa_0, \tag{4}$$

that circulation is quantized in units of $\kappa_0$. This is required if the complex order parameter $\Psi$ is to be single valued as we traverse around the path of integration.

Following from fundamental quantum mechanical assumptions, that is, the existence of a macroscopic order parameter and a Schrödinger-like equation of motion, it is found that circulation in a superfluid is quantized, and this quantization is with respect to a local inertial frame. By measuring these circulation states, we can use the superfluid as a reference to an absolute, non-rotating frame.

## SUPERFLUID GYROSCOPE

An annular container with a septum and an aperture provide a means to exploit the quantization of circulation to measure rotation of the container with respect to the local inertial frame. If this container is rotating with angular velocity $\omega$, one finds that the superfluid will undergo essentially solid body motion along a contour between the inner and outer radius of the annulus.[6] In order that the circulation is to be quantized along a path threading the annulus and the aperture, a back-flow through the aperture is required:

$$v_a = n\frac{\kappa_0}{l_a} - \omega R\frac{2\pi R_a}{l_a}, \tag{5}$$

where $n$ is an integer, $l_a$ is the hydrodynamic length of the aperture, and $R_a$ is the radius of the annulus.

In our device, this back-flow is detected by measuring the apparent change in the onset of vortex nucleation in the aperture. These vortices nucleate at a superfluid velocity

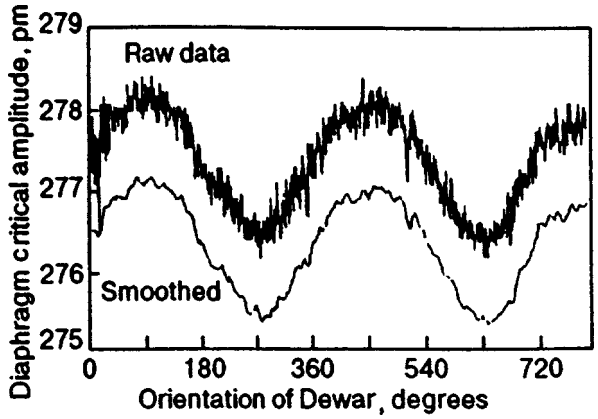


FIG. 1. Modulation of diaphragm critical amplitude from Earth's rotation. Smoothed curve has been shifted down 0.5 pm for visibility.

$v_c \pm \Delta v_c$, where $v_c$ is relative to the walls of the aperture, and $\Delta v_c$ is the spread in velocity from the stochastic (thermal or quantum) nucleation mechanisms. One can see that the superfluid gives a reference to an absolute, non-rotating, inertial frame, since the apparent change in the apparent critical velocity in the aperture will be zero in this frame.

Free vortices which are inevitably created when the superfluid sample cools through $T_\lambda$, will produce a non-zero bias through the aperture when the gyroscope is at rest. By making measurements at two opposing orientations of the sensing loop, one can reject this bias and detect only the signal from absolute rotation. This is the same technique used to make an absolute magnetometer using a superconducting rf SQUID.[8]

We have demonstrated a device which is very similar in dynamics and operation to a superconducting rf SQUID. The device is a two hole, diaphragm-aperture superfluid oscillator and is fabricated from a 1.5 cm silicon square. It has a perimeter sensing loop with an area of $\approx 1\times 10^{-4}$ m$^2$. By utilizing silicon processing techniques,[9] we are able to integrate the submicron sized aperture with a patterned, thin sensing loop (80 $\mu$m thick). Also, the superfluid flow field is easily calculated in this two dimensional geometry using commercial partial differential equation solving software.

This device shows a staircase response which is characteristic of an rf SQUID. By reorienting the sensing loop with respect to the Earth's rotation vector, we find that the apparent critical velocity in the aperture is modulated as expected Fig. 1. We drove the superfluid oscillator onto the first step and continuously recorded the apparent critical amplitude while reorienting the Dewar. This reorientation was at a rate of 1 rev/h and had the effect of changing the Earth's rotational ''flux'' through the perimeter sensing loop.

The noise in this gyroscope originates from the uncertainty in the superfluid critical velocity at which a vortex is nucleated. Typically, $\Delta v_c$ is $\sim 2\%$ of $v_c$. One can show that the rotation resolution in rad/s per $\sqrt{\text{Hz}}$, given this uncertainty in critical velocity, is

$$\sqrt{S_\omega} = \frac{1+R}{R}\,\frac{l_a}{A_{\text{eff}}\sqrt{8\pi\nu_H}}\,\Delta v_c, \tag{6}$$

where $R$ is the ratio of the hydrodynamic inductances of the two hole oscillator, $A_{\text{eff}}$ is the effective sensing area, and $\nu_H$ is the oscillator resonance. In our case, $l_a = 0.25\times 10^{-6}$ m, $R = 7$, $A_{\text{eff}} = 9.8\times 10^{-5}$ m$^2$, $\nu_H = 66.5$ Hz, $v_c = 8.4$ m/s, $\Delta v_c = 0.22$ m/s, thus $\sqrt{S_\omega} = 15\times 10^{-6}(\text{rad/s})(1/\sqrt{\text{Hz}})$.

## SUPERFLUID GYROSCOPES AND THE LENSE-THIRRING EFFECT

It is predicted that the local inertial frame is not the same frame as that attached to the fixed stars. The relative rotation between these two frames is expected to be at the level of tens of milli-arcsec per year, and arises from the general relativistic effect of the rotating Earth on the local inertial frame, the gravitomagnetic field.[10] Motivations for detecting this gravitomagnetic field are found at the most fundamental level of physics. Detection of this effect would provide information to basic questions concerning general relativity and the origins of inertia.[11]

Currently, there are two active experiments which intend to measure this new field: LAGEOS[12] and Gravity Probe B (GPB).[13] The LAGEOS experiments involves the tracking of Earth orbiting satellites. The gravitomagnetic field should precess the plane of the orbit. The GPB experiment uses spinning quartz sphere gyroscopes on an Earth orbiting satellite. In this case, the measurement is of the precession of the gyro axis. Although a superfluid gyroscope is very far from possessing the sensitivity required to detect this effect, it is interesting to compare it to these existing projects.

One could imagine three superfluid gyroscopes oriented mutually perpendicular, attached to a platform carrying a pointing telescope. These gyroscopes provide a measure of absolute rotation about any axis and by combining the output of these gyroscopes with a feedback loop and actuators, one could hold the platform non-rotating with respect to our local inertial frame. Using the telescope to provide a reference to the inertial frame of the distant universe, it is predicted that the observed star would drift as viewed by the telescope at a rate consistent with the Earth's gravitomagnetic field. This experiment is essentially the inverse of the GPB experiment.

In comparison to LAGEOS, both the superfluid gyroscope and GPB are less sensitive to effects which cause additional rotations, such as the non-spherical mass distribution of the Earth. For LAGEOS, one must model these effects to a precision better that one part in $10^7$ to resolve the small residual rotation caused by the general relativistic effect. For GPB, the rotation caused by the Earth's oblateness is about one third the rate of rotation caused by the gravitomagnetic field. A superfluid gyroscope would have a similar low sensitivity to such a non-ideality, and thus would provide a much more direct measurement as compared to the LAGEOS experiment.

As compared to the spinning quartz balls used for GPB, the superfluid gyroscope has a much more relaxed constraint on the physical environment: fewer ''Near Zero'' requirements. The spinning sphere gyroscope requires: exotic fabrication, extreme vacuum, a method to spin-up and suspend the spheres, and ultra-low ambient magnetic and electric field. The superfluid gyroscope does not require such ex-

treme experimental conditions: helium couples very weakly to electromagnetic fields through the small dielectric polarizability; a superfluid gyroscope will never ''spin down'' since the measured effect is given by a quantum constraint.

The superfluid gyroscope is a rate sensor, while the GPB scheme is an angle sensor. If one used the superfluid gyroscope in a feedback loop as described, the error in the angular orientation will grow with time, $\tau$: $\sigma_\theta = \sqrt{\tau S_\omega}$. Thus, the signal-to-noise ratio will grow only as the square root of time. To obtain a resolution of 1 milli-arcsec after a measurement time of 1 year, a superfluid gyroscope with spectral noise density of $\approx 1\times 10^{-12}(\mathrm{rad/s})(\sqrt{\mathrm{Hz}})$ is required. This requires an improvement of a factor of $\approx 5\cdot 10^6$ over our demonstrated gyroscope.

As for GPB, the signal from the precessing spinning spheres increases linearly with the measurement time, but only if the spurious torques are negligible. The axis of the spinning sphere is taken to be the reference to the nonrotating inertial frame. If this axis is perturbed the measurement can be lost. With a superfluid gyroscope one is always measuring with respect to the inertial frame, and this frame cannot be ''lost'' due to some perturbation midway through the measurement or by an unknown torque during the time of measurement.

It is essential to note that we make this comparison to existing experiments with caution. The superfluid gyroscope has only been recently demonstrated with a modest level of sensitivity and it is as yet unclear what problems will be encountered as one attempts to achieve higher sensitivities. Fundamental measurement issues such as low-frequency noise and stability are not yet known.

## CONCLUSIONS AND FUTURE DIRECTIONS

The superfluid gyroscope offers a technique to measure absolute rotation. Given the sensitivity of the first realized devices, it is very interesting to continue to develop increasingly sensitive superfluid gyroscopes. Research efforts to improve the sensitivity of the superfluid gyroscope should be focused in two areas as indicated by Eq. (6): increasing the coupling with larger sensing loops, and finding ways to decrease the uncertainty in the critical velocity for vortex nucleation.

The first step to improve rotational coupling would be to wind a much larger area, multi-turn, sensing loop. If we limit the size of the loop to fit into our current apparatus (10 cm dia. Dewar), we could increase the rotational coupling by 1000 in comparison to our current apparatus. Ideally, if one could suppress all forms of non-fundamental noise and disturbance, one could achieve a sensitivity of $5\cdot 10^{-6}$ of the rotation of the Earth with a measurement time of 1 h. This would be a significant step toward realizing a superfluid gyroscope which could sense the Earth's gravitomagnetic field.

This work is supported by the Office of Naval Research and the National Science Foundation.

*E-mail: packard@socrates.berkeley.edu

[1] J. Anandan, Phys. Rev. Lett. **47**, 463 (1981).
[2] M. Gerdonio and S. Vitale, Phys. Rev. B **29**, 481 (1984).
[3] R. E. Packard and S. Vitale, Phys. Rev. B **46**, 3540 (1992).
[4] O. Avenel and E. Varoquaux, Czech. J. Phys. **46**, 3319 (1996).
[5] K. Schwab, N. Bruckner, and R. E. Packard, Nature (London) **386**, 585 (1997).
[6] K. Schwab, Ph.D. thesis, University of California, Berkeley, USA (1996).
[7] J. Anandan, J. Phys. A **17**, 1367 (1984).
[8] B. Cabrera, in *Near Zero: New Frontiers of Physics*, J. Fairbank, J. B. S. Deaver, C. Everitt, and P. F. Michelson (eds.), W. H. Freeman and Company, New York (1988), pp. 312–322.
[9] K. Schwab, J. Steinhauer, J. Davis, and R. Packard, J. Microelectromechanical Systems **5**, 180 (1996).
[10] J. Lense and H. Thirring, Phys. Z. **29**, 156 (1918).
[11] I. Cuifolini and J. A. Wheeler, *Gravitation and Inertia*, Princeton University Press, Princeton, New Jersey (1995).
[12] D. Smith and P. Dunn, J. Geophys Res. Lett. **7**, 437 (1980).
[13] C. W. F. Everitt, same as Ref. 8, pp. 587–639.

This article was published in English in the original journal.

# Thermal conductivity measurements and self-organized criticality very close to the superfluid transition in $^4$He

W. A. Moeur, P. K. Day, F.-C. Liu, and R. V. Duncan

*University of New Mexico, New Mexico, USA**

Fiz. Nizk. Temp. **24**, 147 (February 1998)

[S1063-777X(98)01202-X]

We would like to present the results of thermal conductivity measurements in $^4$He very close to the superfluid transition in a range of heat flux $5\ \mathrm{nW/cm^2} < Q < 100\ \mathrm{nW/cm^2}$. These measurements were performed in an experimental cell which employs a unique side-wall probe geometry. These side-wall probes allow us to circumvent the boundary effects usually associated with measurements made with end cap thermometer probes. These side-wall probes also facilitated a single probe measurement technique that allowed measurements of thermal conductivity to within several nanoKelvin of the superfluid transition temperature. In this region of temperatures, the thermal conductivity is predicted to display a dependence on the heat flux applied.

In addition to the thermal conductivity measurements, we report on an experimental observation of self-organized criticality in $^4$He very close to its superfluid transition. A constant temperature gradient, independent of the heat flux $Q$ through the sample, is created along a vertical column of $^4$He by applying heat to the top of the column. This constant temperature gradient equals the gravity-induced gradient in the superfluid transition temperature, indicating that the thermal conductivity of the sample has self-organized. The closeness to criticality in this state is the same throughout most of the sample, and it depends only on $Q$. These measurements have been made in a range of $Q$ from 0.04 to 6.5 $\mathrm{mW/cm^2}$ in the absence of convection.

This work was accomplished with support from the NASA Microgravity Science and Applications Division as part of the DYNAMX flight project. This project intends to measure the thermal conductivity of $^4$He close to the superfluid transition in a microgravity environment aboard a NASA space shuttle.

*E-mail: duncan@coffee.phys.unm.edu

This article was published in English in the original journal.

  

# Low temperature physics without a cryostat: laser cooling and trapping of atoms

N. P. Bigelow

*Department of Physics and Astronomy, Laboratory for Laser Energetics and The Materials Science Center; The University of Rochester, Rochester, 14627 New York, USA**

Fiz. Nizk. Temp. **24**, 148–157 (February 1998)

In recent years, there has been significant interest in the laser manipulation of neutral atoms, and specifically in the use of light fields to manipulate not only the internal but also the external coordinates of an atom. Among the most dramatic results of this work have been the production of dense ultra-cold samples of trapped neutral atoms. These samples have been used to expand the horizons of fundamental physics and have made possible significant advancements in metrology. Furthermore, the ability to manipulate atomic motion with light has helped to create entirely new fields of research such as atom optics where matter wave analogues of light wave systems are investigated and optical where light is used to create a periodic array of atoms similar to crystals. 
[S1063-777X(98)01302-4]

## LASER COOLING: A HISTORICAL VIEW

The idea of manipulating atomic motion through the basic properties of the atom-field interaction represents a significant change in the paradigm of atomic physics. At the turn of the century, as physicists began to explore the idea which we now describe under the heading ''modern physics'', the focus of attention in describing the atom-field interaction was on the changes that photon absorption and emission caused in the atom's *internal* coordinates (the electronic quantum numbers). Energy conservation in the process is key; the change of the electronic energy must equal that of the absorbed or emitted photon ($E_{\rm ph}=hf_{\rm ph}$) and the selection rules for various possible and forbidden transitions reflect the constraint of the conservation of angular momentum of the atom+laser field system. Starting with de Broglie, the idea that a photon carries linear momentum ($p=h/\lambda$) as well as angular momentum was well established. However, it was not until the mid-to late 1970s that the consequence of linear momentum transfer in the atom-field interaction was considered as a viable means of manipulating atomic velocities. By the mid 1980s this possibility had been experimentally demonstrated and by the 1990 dozens of laboratories around the world were carrying out experiments on laser cooled and trapped atoms. Temperatures of microKelvins were being measured, and the very nature of the center-of-mass motion of the atom was shown to need a fully quantum treatment to explain many observed effects. At the time of this Workshop, the physics of laser cooling and atom trapping has already had an impact on a variety of problems: compact cold-atom clocks have been built which compete in accuracy with the worlds best time standards and are cheaper and more compact; novel forms of materials fabrication have been demonstrated and are under vigorous investigation in both academic and industrial settings; ultra-high precision gravitometers and accelerometers have been built and are constantly being improved. And these examples are only a small sample of the variety of work underway in LCAP laboratories.

## WHAT IS THE LIGHT PRESSURE FORCE?

There are two essential ideas which can be used to provide a fairly complete answer to this question. One relates to processes in which an atom absorbs a photon and then re-emits it some characteristic time $\tau_{\rm sp}$ later. The other relates to processes in which stimulated emission must be accounted for. In most situations the force experienced by a two level atom interacting with a monochromatic light field can be expressed as $F=F_{\rm sp}+F_{\rm st}$ where the first and second terms reflect the spontaneous and stimulated components of the force, respectively.

Stimulated forces arise from the interaction between the quadrature component of the dipole moment induced in the atom by the field and the gradient of the field. Unlike $F_{\rm sp}$, $F_{\rm st}$ is a conservative force and is often referred to as the dipole or gradient force because it changes sign with detuning and because it depends on the *gradient* of the field intensity. Because the dipole force is conservative, it can be expressed in terms of a potential $U(x)=-h\Delta\ \ln[1+p(x)]$ where

$$p(x)=I(x)/I_{\rm sat}(2)(\Gamma/2)^2/[\Delta^2+(\Gamma/2)^2],$$

$I_{\rm sat}$ is the two-level saturation intensity. Hence, for moderate field intensities or large detunings (compared to $I_{\rm sat}$) $F-\nabla I(x)$.

The spontaneous force is the workhorse of many laser cooling experiments and the so-called optical molasses. $F_{\rm sp}$ can be understood in terms of the momentum transferred to an atom as photons are absorbed and re-emitted spontaneously. When an atom absorbs a photon it receives a momentum kick and recoils along the wavevector $\mathbf{k}$ of the absorbed photon. If the subsequent reemission is via spontaneous emission, then the emission direction is randomly oriented in space. Averaged over many events, the momentum transfer to the atom on emission averages to zero, whereas the momentum transfer on absorption is cumulative, producing a finite average force along $\mathbf{k}$. The size of this force is of the order of the recoil momentum per absorption $h\mathbf{k}$ multiplied by the transfer rate (the inverse of the excited state lifetime for the driven transition). For sodium, this corresponds to

about 10–20 $N$, or an acceleration of $10^6$ m/s!. Note that the length scale over which $F_{sp}$ varies is determined by the variations in **k** (particularly its direction) and by the spatial variations in the field intensity.

If the light field is an optical standing wave, and the field frequency is tuned below (to the red off) the two level transition frequency, then spontaneous processes can give rise to a damping of atomic velocities. The velocity damping (cooling) arises from the fact that an atom with a finite velocity will be Doppler shifted into resonance with the traveling wave component of the standing wave which is directed opposite to the atomic motion. The atom will therefore absorb and re-emit more photons from this wave than a slower atom with a smaller Doppler shift. Clearly then, the faster atom will generally experience the larger force. The result is a velocity dependent photon scattering rate. Moreover, this velocity dependent force will be directed opposite to the atom's velocity, causing the atom to decelerate. This configuration is referred to as optical molasses and can readily be generalized to three dimensions. The ''terminal'' velocity or temperature for an atom in equilibrium with optical molasses is determined by the balance between the Doppler cooling and the spontaneous or diffusive heating associated with the individual random velocity recoil kicks experienced during spontaneous emission. In other words, by equating the time averages: $\langle$heating due to diffusive random spontaneous kicks$\rangle$=$\langle$cooling rate in molasses$\rangle$. In the limit where the atom is modeled as a simple two-level system (ground and excited states) it is expected that the atomic sample will equilibrate at the so-called Doppler temperature $T_D = h\Gamma/2k_B$ which, for sodium, is 240 $\mu$K. To the surprise of many researchers, it was discovered by the group at NIST[1] that, in fact, the atoms in optical molasses were cooled to well below this temperature by the molasses. More recently, for Cs atoms, temperatures below 2 $\mu$K (barely a few photon recoil kicks of average momentum!) have been achieved using optical molasses. The microscopic explanation for this remarkable supercooling power of optical molasses involves two facts: first, the atoms are rarely two-level systems, and usually a complex magnetic substructure is present and cannot be neglected. Second, there are complex spatially varying intensities and polarizations of a three-dimensional optical molasses which cannot be neglected. These two facts, coupled with the effects of optical pumping give rise to a new time scale in the cooling problem: the internal time scale for motion of population amongst these internal states. The results is a beautiful mechanism,[2] now frequently referred to either as polarization gradient or ''Sisyphus'' cooling which explains the deep cooling. It is important to recognize the temperatures used to describe these laser cooled gasaes are *true kinetic temperatures*. In fact, the gas temperature is often measured by analyzing the ballistic motion of the atoms in the absence of the optical trap using a time-of-flight technique.

## CLOCK-TYPE MEASUREMENTS AND FUNDAMENTAL PHYSICS

Traditionally, one of the most important goals of research in atomic physics is the measurement of fundamental constants of nature. Among the most important atomic physics ''devices'' is the high-precision atomic clock. These clocks not only provide the standard by which we tell time, but are crucial to the way we communicate and navigate on earth and in the air: Without question, atomic clocks affect almost every aspect of modern life. Two vital concerns in the conception of such ultra-high precision devices are: (1) that the precision is inversely proportional to the observation time (this stems from the uncertainty relation $\Delta E \Delta t \geqslant h/2$) and (2) that the first and second order Doppler shifts associated with atomic motion can cause broadening of the atomic transition, thereby compromising the measurement accuracy and precision. Laser cooled atoms have significantly pushed back both of these limitations. This is because these atoms move *very* slowly and because they remain in a given observation volume for *very* long times. Indeed, compact cold atom clocks have already been built and have provided a short term stability that is significantly better than the commercial standards. Nevertheless, observation times in these clocks are still set by gravity: ultimately, the atoms fall out of the experiment under their own weight! Increased observation times are possible in microgravity and can result in at least one or two orders of magnitude further improvement. A long-term accuracy near a part in $10^{17}$ is expected—making these clocks three orders of magnitude better than accepted standards and several additional orders of magnitude better than current space-qualified clocks!

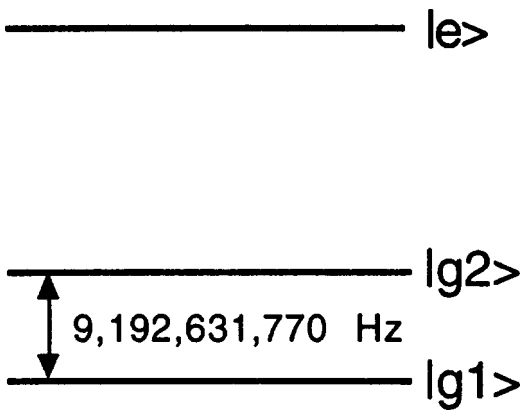


FIG. 1. The ground state hyperfine splitting of atomic cesium.

## THE ATOMIC FOUNTAIN CLOCK

The atomic beam frequency standards currently maintained by NIST and other laboratories around the world are based on measurements made using what is referred to as the Ramsey separated zone technique. Common atoms for use in these clocks are atomic rubidium (Rb) and cesium (Cs). Here the transitions between two hyperfine ground states form the atomic ''reference frequency.'' Consider for example cesium (see Fig. 1). To probe this ground state level splitting, transitions between $g1$ and $g2$ are induced as the atoms pass through a pair of spatially separated microwave cavities which are aligned along the atomic beam axis. In this type of separated zone measurement, the performance of the clock is strongly determined by the integration time which is set by

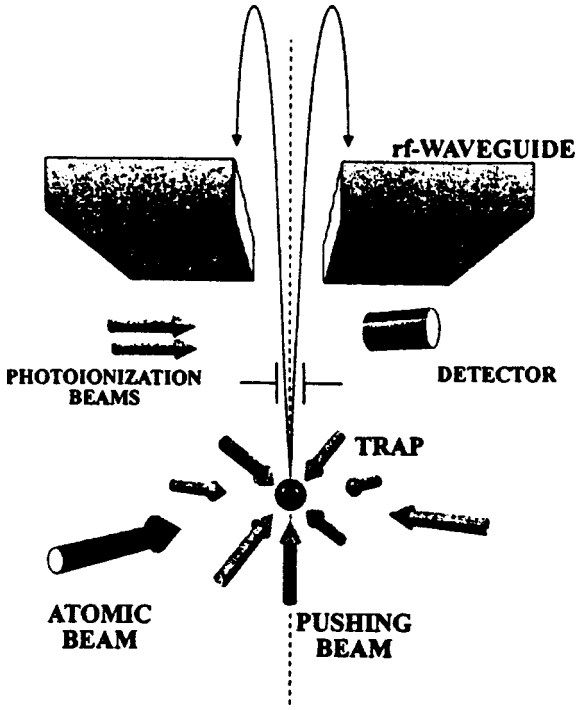


FIG. 2. A sketch of a cold-atom atomic fountain clock.

the time-of-flight of the atom between the two microwave cavities; the longer the time, the more accurate the final measurement.

In the cold-atom fountain clock, a significantly different geometry is used. First, a laser cooled sample of atoms is prepared and positioned below a single microwave cavity. By pushing on the bottom of the ultra-cold atomic sample with a pair of laser beams oriented along the vertical axis (see Fig. 2), the sample is launched upward, against the force of gravity, such that it passes through the cavity. The atoms then slow due to the acceleration of gravity, turn around, and eventually fall back downward through the microwave cavity. In this way, the atoms pass through the cavity twice and an effective ''two-zone'' measurement is made using only one true interaction zone.

One obvious advantage of the cold-atom fountain clock is that a two-zone measurement can be made *with only one cavity*. This leads to a reduction in the amount of hardware and has the additional advantage that systematics associated with possible differences between the cavities are reduced. However the most important advantage of the cold-atom fountain clock is that substantially longer integration times can be realized and that this can be achieved using a much smaller apparatus. For example, using a hot atomic beam (400 K) the typical measurement integration times are $\sim 10$ ms for a 2 m cavity separation whereas, for the cold source ($<1K$), an integration time of $\sim 0.5$ s is possible with a clock for which $h=0.3$ m! Using a cold-atom clock based on a laser cooled sodium vapor, the group at Stanford has reported[3] Ramsey fringe width measurements of $\sim 2$ Hz ($\sim 100$ times narrower than typical in ''hot'' atom clocks). Similar devices have been investigated using cesium atoms[4] yielding a $\delta\nu/\nu_{hf}$ of $\sim 10^{10}$. From this type of device, a meaningful performance figure of merit is given by the Allan variance $\sigma \approx 3\times 10^{-14}/\sqrt{\tau}$ or $10^{-16}$/day.[5] (This is a vast improvement over typical flight qualified clocks, which perform at a $10^{-12}$ level, and commercial atomic frequency standards which perform at about $10^{-14}$!) In microgravity, one can expect to take the performance of the cold-atom clock even further. In the terrestrial fountain clock, the interaction time is set by the size of the apparatus and most specifically by the fountain height $h$. In particular, $T_{\rm int}\sim\sqrt{h}$. In microgravity, the interaction times will be set instead by the ballistic expansion of the atoms within a single observation volume. An increase of performance to $\sim 10^{-17}$/day can be expected if nK temperature atoms are used. Experimental investigations of microgravity clocks have already begun in France[6] and a vigorous effort on cold-atom clocks is also currently underway within the NASA Microgravity Fundamental Physics program.

In order for cold atom space clocks to reach their full potential, one important problem that will have to be addressed will involve the management of collisional frequency shifts. Such shifts are particularly important problems for fountains based on ultracold atoms because in the low temperature limit $s$-wave scattering dominates and collisional crossections begin to scale as $\lambda_{dB}^2/\pi$ (where $\lambda_{dB}$ is the thermal de Broglie wavelength which *increases with decreasing temperature*). Indeed, the Stanford group have already used a cold atom fountain clock to directly measure mHz level collisional shifts.[7] Such shifts may not present fundamental limitations for cold-atom clocks, however, and several novel schemes utilizing coherent interference effects and/or multi-color laser excitation techniques have already been proposed to circumvent collisional shifts. Indeed, experiments are already underway to implement and test these strategies.

## FUNDAMENTAL CLOCK-TYPE EXPERIMENTS IN SPACE

Almost every measurement made in science ultimately traces to a time or frequency measurement (thermometry, distance measurement, pulsar period timing, etc.) and both terrestrial and deep space navigation rely crucially on precision clocks. However, the introduction of ultra-high precision cold atom clocks into the microgravity program is of deeper significance. At the heart of the atomic clock is a measurement of a carefully chosen energy level splitting within the atom. These splittings are not only nature's own reference ''standards'' but, at the resolution which can be expected using microgravity clocks, the splittings become measurably sensitive to subtle aspects of fundamental forces and to basic symmetries of nature. Usually, these last classes of questions are the realm of high-energy or ''particle'' physics. Ultra-high precision atomic measurements, however, can now make important contributions to answering these questions and microgravity fundamental physics can play a vital role in this contribution. For example, parity nonconservation experiments in atomic cesium already compete with accelerator based measurements for the determination of the Weinberg angle, a direct measure of the electroweak mixing angle in the Weinberg–Salam model (and a number which determines the ratio of the $W$ to $Z^*$ boson

masses). As with any clock type measurement, one important limitation of these experiments remains the observation time. It is natural then that these experiments should benefit from the use of laser cooled atoms and should benefit even more so from the microgravity environment of space.

#### Electric-dipole moment

An experiment closely related to PNC is the search for the permanent electric-dipole moment (EDM) of the electron. The existence of an EDM can be traced directly to T and/or CP violating interactions, or, in other words, to the most basic symmetry properties of nature. The EDM measurement consists of a *very precise* determination of the response of the atomic level splitting to an applied electric field. Essentially, this is a clock-type measurement: a state is prepared and allowed to evolve in the presence of an applied electric field. After some period the populations of the atomic states are then probed and used to determine level shifts and spacings. Using microgravity, a cold-atom EDM apparatus is predicted to provide at least *two orders of magnitude of improvement* over the current EDM measurements (to date these measurements have placed an upper bound on the possible moment). Regardless of the exact outcome of an improved EDM experiment, the results are essentially *guaranteed* to be significant: If this experiment detects no moment (with better than a precision of $\sim 10^{-17}$ e-cm—the expected accuracy of a microgravity EDM experiment) then several theories competing with the Standard Model can be eliminated: supersymmetry, flavor changing, etc. On the other hand, *if a moment is detected*, far reaching revisions in the foundations of physics will be required. The significance of such fundamental LCAP experiments is currently reflected in the support of ground based EDM experiments within the current Microgravity Fundamental Physics program.

#### General relativity

The clock itself reaches deeply into the foundations of physics. Clocks are central in the realm of general relativity and in questions concerning the very nature of gravity itself. Here the motivation for space based clocks is not only tied to the improved performance expected in a microgravity environment but because these clocks will have access *to fundamentally different positions in space-time than are available on earth*. An important example of this latter physics is that revealed in the comparison of an earth based clock with a space based clock. This comparison provides a direct measurement of the gravitational red-shift. Indeed, improvements of one to two orders of magnitude of the current accuracy of 100 parts per million can be expected using space based ultra-high precision clocks. Measurement of the gravitational red-shift test important aspects of the local position invariance part of Einstein's Equivalence principle and is tied to the possible spatial variation of the fine-structure constant $\alpha$—a parameter central to quantum electrodynamics.

#### Multiple clock experiments

The motivation for developing cold-atom clocks for use in a space environment goes beyond a desire for absolute performance. If performance were the only goal, then the demand would be to develop the best possible space qualifiable clock with no regard for laser cooling and the clocks underlying physical mechanism. However, there are important reasons for which this is not the case. The first example are the clock-type measurements (such as the search for the permanent dipole moment of the electron) as discussed above. There is no direct analogue of these experiments that can be carried out using ion clocks or superconducting cavity oscillators. However, there is a second important point: there is an important class of experiments that can be carried out *only if there are multiplicity of different types of high precision clocks available in space*. This class of measurements is based on systematic measurement of the mutual drift of clocks based on vastly different physical mechanisms. Indeed, such a measurement have been identified as an important issue earlier this century by leading physicists such as P.A.M. Dirac. The basic idea is that different clock designs can be sensitive to different fundamental forces. Consider, for example, the atomic clock. Here the hyperfine splitting (the frequency reference) is determined by both nuclear interactions (through the contact hyperfine interaction) and by electromagnetic interactions. By contrast, in many designs of flywheel type clocks, such as the high-$Q$ microwave resonator, the frequency is set by some mechanical dimensions of the clock and hence is mostly determined by electromagnetic forces and gravitational stresses. As a result, a comparison of the relative drifts of these clocks in a microgravity experiment could give unique insight into the relative drifts of the strong and electromagnetic forces.

### ATOM OPTICS AND ATOMIC INTERFEROMETRY

Atom optics is the field of research aimed at the development of devices and techniques for manipulating atoms in direct analogy with the systems used to manipulate light. Although progress in atom optics has not been limited to work with laser cooled atoms, the motivation for using cold atoms is clear: as the temperature is decreased, the de Broglie wavelength of the atom increase and so the wave nature of the atom emerges more and more dramatically in terms of the atomic center of mass motion. One of the hallmarks of progress in atom optics has been the development of the atom interferometer.

Conceptually, the atom interferometer is essentially identical to the light interferometer. An input beam is caused to split into two or more components which propagate over some distance in space and are then caused to recombine. If the net path traveled by one component differs from that traveled by the other, there will be a phase shift associated with the different path lengths and interference effects between the components can be observed when they recombine. In the atom interferometer, the splitting and subsequent recombination of the atomic wavepacket has been accomplished by using a variety of techniques. Both nanofabricated micro-structures (which act as amplitude gratings) and standing wave laser fields (phase-gratings) have been used as beam splitters. In addition, an interferometer using time dependent light (pulsed) fields has been realized. The interest in atom interferometers is fundamental—in terms of the in-

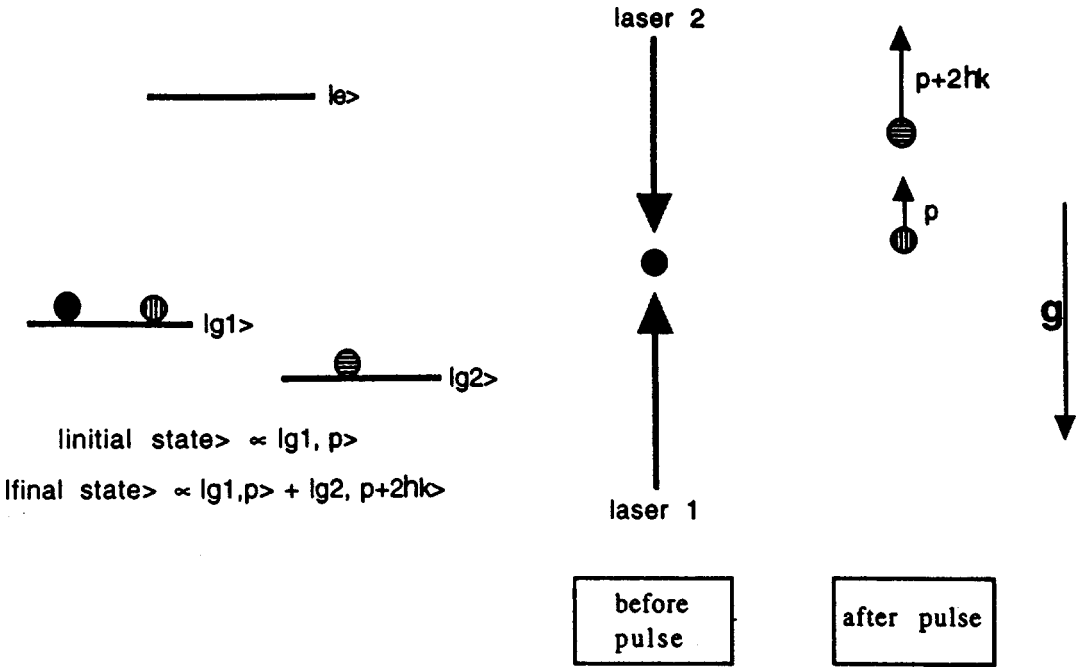


FIG. 3. The ''three-level'' atom (left). A depiction of the atomic momentum before and after the application of the first laser pulse (right). The two components of the wavepacket have different vertical momenta and therefore separate in space. Under the influence of gravity, these atoms slow as the move upward and the laser frequency must be adjusted to account for this velocity change. A measurement of the velocity change can be used to determine the acceleration due to gravity at the location of the experiment.

vestigation of interference of massive composite particles which possess a rich spectrum of internal degrees of freedom—and is motivated by potential applications. One of the applications most relevant to this workshop is the absolute measurement of the acceleration due to gravity.[8] In these experiments a sample of ''three-level'' atoms (see Fig. 3), is initially cooled and confined in an optical trap. The sample is then prepared in one of the two ground states and next it is irradiated with a pair of counterpropagating optical pulses (see Fig. 3, right). The light pulses are configured to act as $\pi/2$ pulse, transferring half of the population to the other ground state. The resulting state of the atom is a wavepacket which is a superposition of two internal states ($g1$ and $g2$) that differ by two photon recoil's worth of momentum. These two components of the atomic wavefunction therefore spread apart in space. In this way, the pulses serve as the beam splitter for the atom. Some time later a second pulse is applied in order to reverse this process and to cause the atomic wavepackets to interfere. Because the atoms simultaneously move under the acceleration of gravity, it becomes necessary to adjust the laser frequencies in order to keep in resonance with the atoms—if the frequency is adjusted to keep the atoms in resonance with the lasers, there will be no net phase shift when the atoms recombined. By measuring the frequency shift required, the acceleration of gravity can be measured. In the Kasevich experiment, the absolute value of $g$ was measured to a part in $10^{-6}$! In a related experiment, the single photon recoil momentum was measured to a part in $10^{-7}$!

## COLDER DENSER SAMPLES: OTHER COOLING AND TRAPPING SCHEMES

### Getting colder

The most common scheme for laser cooling and trapping atoms is the magneto-optical trap.[9] In this trap, a static magnetic field is combined with a three-dimensional optical molasses to yield both cooling (a damping of atomic velocities) and trapping (a restoring force about some fixed point in space). However, in the quest to achieve ever lower temperatures, cooling schemes that involve optical molasses (and hence which involve spontaneous emission) have one basic limitation: the lowest energy scale for the atom will be set by the single photon recoil energy. It is important to recognize that the maximal advantage of a microgravity environment for many LCAP experiments will be realized with the coldest possible atoms. For this reason, the cooling of atomic vapors below the recoil limit is of interest to this workshop.

To break this fundamental barrier—the single photon recoil limit—several techniques have already been investigated. One very elegant technique is referred to as velocity selective coherent population trapping.[10] This technique involves using laser fields to create a coherent superposition state of the atom which effectively turns-off the atom's ability to fluoresce (these states are named ''dark-states''). Using this approach, kinetic temperatures below the single photon recoil have already been achieved.[11] However, the technique has been less successful at increasing the phase space density of the atomic samples (density in configuration space and momentum space).

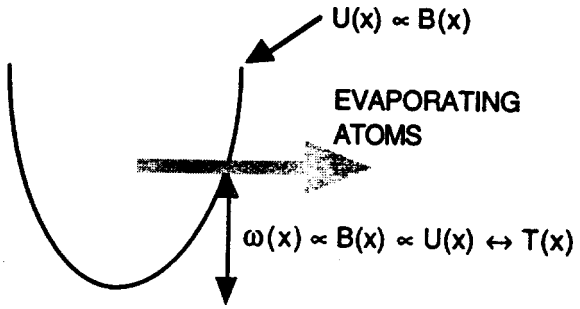


FIG. 4. The magnetic trap and rf forced evaporative cooling.

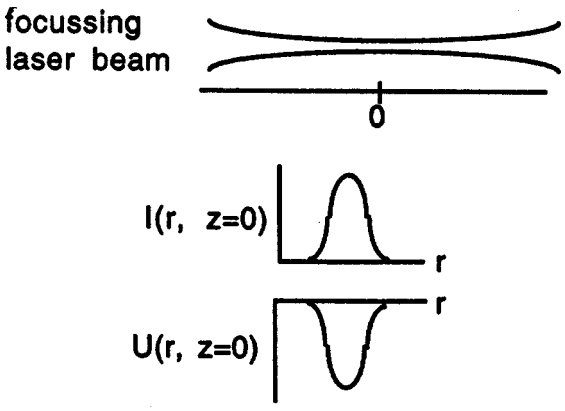


FIG. 5. Dipole (FORT) trap made from focused laser beam tuned below the atomic resonance frequency.

#### Conservative traps and evaporative cooling

A second strategy involves the deep cooling of the atoms by evaporation. In this scheme, the hottest atoms in the distribution are allowed to escape preferentially from the sample, leaving only the cold atoms behind. The basic ingredients for evaporative cooling are a conservative trap potential in which the atoms can be suspended and a means for removing or ''evaporating'' the most energetic atoms in the sample. Two popular schemes for creating such a potential are the magnetic trap and the dipole trap.

In the magnetic trap (see Fig. 4) a force is exerted on the atoms by coupling to the atomic magnetic moment. Depending on the alignment of the magnetic moment with respect to the field, there is an associated potential energy $U=-\mu \times B$. If a field configuration is used in which **B** varies in space, then there will be a gradient in this potential and hence a force on the atom. To induce evaporation an rf field $\omega$ is applied to the sample which induces atomic spin-flips. When the spin (magnetic moment $\mu$) of the atom is flipped, the magnetic energy for that atom changes sign, and the magnetic force on the atom ejects that atom from the trap. The technique can be used to select out the hottest atoms in the sample because the rf resonant frequency needed to flip the atomic spin is determined by the magnitude of the field **B** at the atomic coordinate, which is in turn determined by the position in the potential and hence by the kinetic energy (the temperature) of the atom. This technique for deep cooling has recently been used to increase the phase space density of cooled and trapped atoms to the point where Bose–Einstein condensation has recently been observed in a trapped atomic vapor.

#### Dipole traps and the FORT

An alternate trapping scheme is the far off resonance dipole trap (FORT).[12] In this scheme (Fig. 5) the electric dipole force $[F=-\nabla(\mathbf{p}\cdot\mathbf{E})=-\nabla U_{\rm dip}(x)$—see above] is used to confine the atoms in a tightly focused laser beam. By varying the laser beam parameters, the depth of the confining potential can be modified and evaporative cooling can be made to occur.[13] The dipole and FORT traps has also been used to carry out many elegant experiments on ultra-cold collisions among the trapped atoms.[14]

#### Gravity?

In addition to providing a potential from which the atoms can be evaporated, a prime *raison d'être* for each of these traps is to *balance the effects of gravity*: from the point of view of precision spectroscopy, the presence of the trap force can significantly perturb the sample, giving rise to incipient frequency shifts, distortions of the atomic cloud. Furthermore, the presence of gravity introduces limitations and the accuracy of ballistic expansion measurements and will limit the ultimate efficacy of additional deep cooling techniques (not discussed here) such as adiabatic expansion cooling.

#### Bose–Einstein condensation: new phase transitions, new states of matter and new superfluids

Perhaps one of the most dramatic developments of the 1990s has been the realization of Bose–Einstein condensation (BEC) in a dilute atomic vapor. Bose condensation is a phase transition that occurs in a gas of identical bosons when the interparticle spacing becomes comparable with the thermal de Broglie wavelength. At this point, the particles are no longer quantum mechanically distinguishable and a correct quantum treatment of the gas is made in terms of a fully symmetrized macroscopic wavefunction. From a statistical point of view, the condensate represents the macroscopic occupation of a single quantum state, usually thought of in terms of the ground momentum state of the system. The physics of these Bose condensed vapors is intimately tied to the physics of quantum fluids studied in the field of low temperature physics. Soon, BEC experiments will require microgravity and a strong synergy with related work in low temperature physics should come naturally. However, the need for microgravity BEC experiments may also be driven independently by efforts to achieve lower sample temperatures and higher densities. In particular, as noted earlier, forced evaporative cooling depends on the spatial distribution of the hot tail of the trapped atom sample and the shape of this distribution near the classical turning point in the confining trap potential. As the sample becomes colder and colder, and as the sample moves closer and closer to the

bottom of the trap well, the atomic distribution will be distorted by gravity, an effect that will disrupt the ability to control the cooling process.

In the current experiments, the pathway to BEC begins with a laser cooled sample ($-10^{10}$ atoms at $-20\ \mu$K). This sample is then loaded into a magnetic trap and evaporatively cooled until the system condenses. In the earliest experiments[15] this occurred at about 170 nK for $10^3$ atoms. In recent experiments sample sizes in excess of $10^6$ atoms have been condensed. The condensate in this work has been detected by releasing the atoms and examining the free expansion of the condensed cloud in order to determine the momentum distribution of the sample.

One of earliest successes of trapped alkali BEC has been in the excellent agreement between the experimental data and the theoretical results derived using a mean-field theory. A representation of the condensate wavefunction in the mean field picture can be derived from the Gross–Pitaevskii (GP) equation. Essentially, this is a Schrödinger equation for the many-particle ground state (the BEC) with an additional term in the Hamiltonian which is of the form: $U_0|\Psi|^2$. Here $\Psi$ is the BEC wavefunction and $U_0$ is the interaction potential between the atoms in the condensate. In many situations $U_0 \sim a_s$ where $a_s$ is the $s$-wave scattering length of the particles. Frequently it is simplest to solve the GP equation in the so-called Thomas–Fermi approximation which essentially means that the kinetic energy term of the Hamiltonian can be neglected. At Rochester, we have developed a new numerical technique based on a variational approach for solving the GP equation without making any approximations.[16] In most situations, the modifications to the shape of $\Psi$ due to the inclusion of the kinetic energy are small. In fact, only in regions where there is a large curvature in $\Psi$ (and hence a large contribution from the $\nabla^2\Psi$ term in the Hamiltonian) does the Thomas–Fermi approximation cause problems. It is not surprising that these problems can become most marked near the condensate boundaries.

With the advent of multi-species traps and the recent realization of a Bose condensate comprised of two different spin-states of a vapor of rubidium atoms[17] a new and important question has arisen: what is the nature of *a two-species Bose–Einstein condensate—the 2BEC?* In approaching this question it is important to realize that we cannot expect that each condensate will simply co-exist with the other condensate. The reason for this is that, even though the alkali BECs are very dilute ($\sim 10^{13}$ atom/cc) the role of interparticle interactions is still crucial. For a 2BEC, then, we must consider three classes of interactions: the two self-interactions of each species and a third ''cross-species'' interaction. In the mean field limit, this means that the 2BEC can be characterized by two coupled GP equations and three scattering lengths $a_{11}$, $a_{22}$, and $a_{12}$ (the cross species scattering length).[17]

A rich array of new phenomena have been predicted for this system including modifications to the ground state wavefunction profile, the excitation spectrum and even the essential stability of the condensate itself. We have been investigating the 2BEC using a modification of our variational technique.[16] In Fig. 6 we show the ground state condensate wavefunction for a mixture of sodium atoms and rubidium

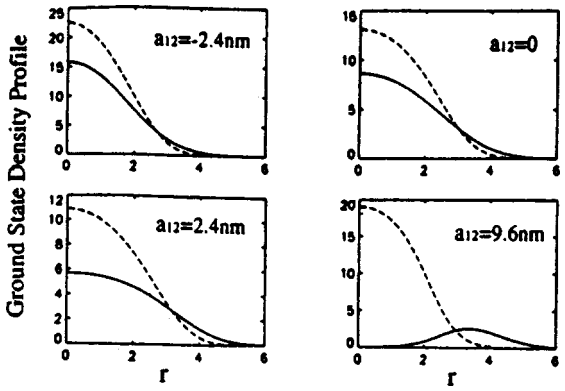


FIG. 6. The ground state density profiles of a two-species Bose–Einstein condensate (2BEC) for two different choices of cross-scattering length $a_{12}$. For this figure we consider a mixture of sodium (Na with $a_{11}=3$ nm) and rubidium ($a_{22}=6$ nm) atoms.

atoms contained in a spherically parabolic trap. The parameter that is varied between the different parts of this figure is the cross scattering length $a_{12}$. We see that for strong repulsive interactions (i.e., $a_{12}>0$) the ground state is definitely not a mixture of two overlapping condensates, but that instead the system has phase separated into two distinct condensates. Because the condensate wavefunction in the mean field is the state which minimizes the mean field energy we can provide a physical interpretation of the phase separation. When the system separates, the overlap between the condensates is reduced, and hence the cross-species mean field energy is decreased. Simultaneously, the outer species must be spread over a larger volume, which decreases its mean field energy. By contrast, the mean field energy of the core increases because the core atoms are now closer together (the core atoms are not ''diluted'' by the second species). Overall, the total system energy is determined by the interplay of these individual energies and in the phase separated state the total mean field energy is minimized. A careful analysis of the JILA two-spin state condensates has provided some evidence for the effective ''condensate repulsion,'' however a true two-species condensate has yet to be realized. At Rochester, an experimental effort on this problem is well underway.

## PERSPECTIVE

In many ways, there is a powerful case that the Laser Cooling and Atomic Physics (LCAP) community can benefit greatly from access to space and to a microgravity environment. Fundamental experiments can be and are being envisioned, experiments that can appreciate significant benefit from implementation in space. Furthermore, there are important fundamental LCAP experiments which *cannot* be realized in a terrestrial laboratory. In a broader framework, it is also clear that LCAP has natural ties to a broad variety of different areas of fundamental science and to the existing programs supported by NASA and other space agencies around the world. In return for the opportunity to carry out research in this new and exciting environment, LCAP research has much to offer to the countries' effort to explore and develop space, contributions ranging from advanced

navigation to high accuracy gravitometry. Furthermore, the support of LCAP activities within the NASA microgravity program has the promise of improving life on earth, for example, through better and more compact space based clocks for terrestrial navigation and geology.

*E-mail: nbig@lle.rochester.edu

[1] P. Lett, R. N. Watts, C. I. Westbrook, W. D. Phillips, P. L. Gould, and H. J. Metcalf, Phys. Rev. Lett. **61**, 169 (1988).
[2] J. Dalibard and C. Cohen-Tannoudji, J. Opt. Soc. Am. B **6**, 2023 (1989); P. J. Ungar, D. S. Weiss, E. Riis, and S. Chu, J. Opt. Soc. Am. B **6**, 2058 (1989).
[3] M. Kasevich, E. Riis, S. Chu, and R. De Voe, Phys. Rev. Lett. **63**, 612 (1989).
[4] A. Clairon, C. Salamon, S. Guellati, and W. D. Phillips, Europhys. Lett. **16**, 165 (1991).
[5] S. Lea, A. Clairon, C. Salomon, P. Laurent, B. Lounis, J. Reichel, and A. Nadir, Phys. Scr. **T51**, 78 (1994).
[6] B. Lounis, J. Reichel, and C. Salomon, C. R. Acad. Sci., Ser. II: Mec. Phys., Chim., Sci. Terre Univers **316 Serie II**, 739 (1993).
[7] K. Gibble and S. Chu, Phys. Rev. Lett. **70**, 1771 (1993).
[8] M. Kasevich and S. Chu, Phys. Rev. Lett. **67**, 181 (1991).
[9] E. Raab, M. Prentiss, A. Cable, S. Chu, and D. Pritchard, Phys. Rev. Lett. **59**, 2631 (1987).
[10] A. Aspect, E. Arimondo, R. Kaiser, N. Vansteenkiste, and C. Cohen-Tannoudji, Phys. Rev. Lett. **61**, 826 (1988).
[11] J. Lawall, S. Kulin, B. Subamea, N. Bigelow, M. Leduc, and C. Cohen-Tannoudji, Phys. Rev. Lett. **75**, 4194 (1995).
[12] J. D. Miller, R. A. Cline, and D. J. Heinzen, Phys. Rev. A **47**, R4567 (1993).
[13] C. S. Adams, H. J. Lee, N. Davidson, M. Kasevich, and S. Chu, Phys. Rev. Lett. **74**, 3577 (1995).
[14] P. Gould, P. D. Lett, P. S. Julienne, W. D. Phillips, H. R. Thorsheim, and J. Weiner, Phys. Rev. Lett. **60**, 788 (1988); J. D. Miller, R. A. Cline, and D. J. Heinzen, Phys. Rev. Lett. **71**, 2204 (1993).
[15] M. Anderson *et al.*, Science **269**, 198 (1995); C. C. Bradley *et al.*, Phys. Rev. Lett. **75**, 1687 (1995); K. B. Davis *et al.*, Phys. Rev. Lett. **75**, 3969 (1995).
[16] H. Pu and N. P. Bigelow, submitted to Phys. Rev. Lett. , (1997).
[17] C. J. Myatt *et al.*, Phys. Rev. Lett. **78**, 586 (1977).
[18] Tin-Lun Ho and V. B. Shenoy, Phys. Rev. Lett. **77**, 3276 (1996); B. D. Esry *et al.*, Phys. Rev. Lett. **78**, 3594 (1997); E. V. Goldstein and P. Meystre, Phys. Rev. A **55**, 2935 (1997).

The references presented here are by no means exhaustive and neither are they uniform in their distribution over the many important contributions made by groups all over the world. I apologize in advance for omissions of any sort. There are many excellent references, one being the *Laser Manipulation of Atoms and Ions*, CXVIII Int'l. School, Enrico Fermi, E. Arimondo, W. D. Phillips, and F. Strumia (Eds.), North-Holland (1992). Because of the rapid advancement in this field, these works are already somewhat outdated and a sample of additional newer results can be found in the bibliographies of the papers listed above.

This article was published in English in the original journal.

# Reconstruction of the charged surface of liquid hydrogen

G. V. Kolmakov, A. A. Levchenko, L. P. Mezhov-Deglin, and A. B. Trusov

*Institute of Solid State Physics, RAS, 142432, Chernogolovka, Moscow District, Russia**
Fiz. Nizk. Temp. **24**, 158–162 (February 1998)

The evolution of shape of the surface of equipotentially charged liquid hydrogen film condensed on the lower or upper plate of a horizontally placed diode in external electric fields has been studied experimentally under the condition of total compensation of the applied field by the surface charge. Reconstruction phenomenon—the formation of a solitary wave (soliton)—has been observed in an electric field higher than some critical value for the film that covers the lower plate. © *1998 American Institute of Physics.* [S1063-777X(98)01402-9]

## 1. INTRODUCTION

It is known that a charged flat surface of a liquid becomes unstable in an external, perpendicular, electric field $E$ that exceeds a critical value.[1] Until the time we began this study the reconstruction of a negatively charged surface of a thick layer of liquid helium (electrons above the helium) was studied experimentally and theoretically in detail in the case where the liquid depth $d$ (the distance from the free surface to the metallic control substrate placed in its interior) exceeded noticeably the capillary length, $\lambda=\sqrt{\alpha/\rho g}$. Here $\alpha$ and $\rho$ are the surface tension and the density of liquid helium, and $g$ is the free fall acceleration. The theoretical considerations were restricted to the case where the electrons that are localized above the surface do not compensate for the applied electric field. It was found that for $d\gg\lambda$ and a fixed number of charges above the surface, when the field exceeds the critical value, a periodic deformation, which is accompanied by the surface charge density modulation with a period of the order of $\lambda$ and finite amplitude (equal to $\lambda$ in order of magnitude), arises on the surface of the liquid (dimple crystal).[2–4] This phenomenon was studied experimentally in Refs. 5–7.

In the opposite case, at $d\ll\lambda$ the range of the wave numbers in which the instability develops starts at $k=0$ (Ref. 8). Theoretical investigations[9] show that in fields higher than the critical field the stationary structure can also appear on the charged surface, but the character of the reconstruction differs markedly from the previous situation: the amplitude of the deformation is proportional to the supercriticality level, while the period is inversely proportional to the supercriticality. Thus, at fields slightly exceeding the threshold value the amplitude of the structure is small with respect to the capillary length $\lambda$.

Theoretical estimates performed for the charged surface of liquid helium layer that has infinite horizontal dimensions and finite thickness $d\gg\lambda$ under the condition of complete compensation have shown that reconstruction to the steady state is impossible, and that the periodic discharge from the surface has to take place.

Until recently it was not clear whether the reconstruction can be observed on the surface under the conditions that the distance $d$ between the control electrode placed above the liquid and the charged liquid surface is nearly equal to $\lambda$, and the electric field is completely compensated for by charges localized below the surface. Preliminary results of our experiments were published in Ref. 10.

## 2. EXPERIMENTAL PROCEDURE

The experiments were performed using two different diodes D1 and D2 inserted into an optical container. As the charge source we used radioactive plates emitting $\beta$ electrons of 5-keV mean energy. The electrons ionized a layer of liquid about 10 $\mu$m thick near the plate.

In the diode D1 we used a metallic guard ring 25 mm or 3 mm inside diameter and 3 mm height. This ring prevented the charges from escaping from the surface of the liquid to

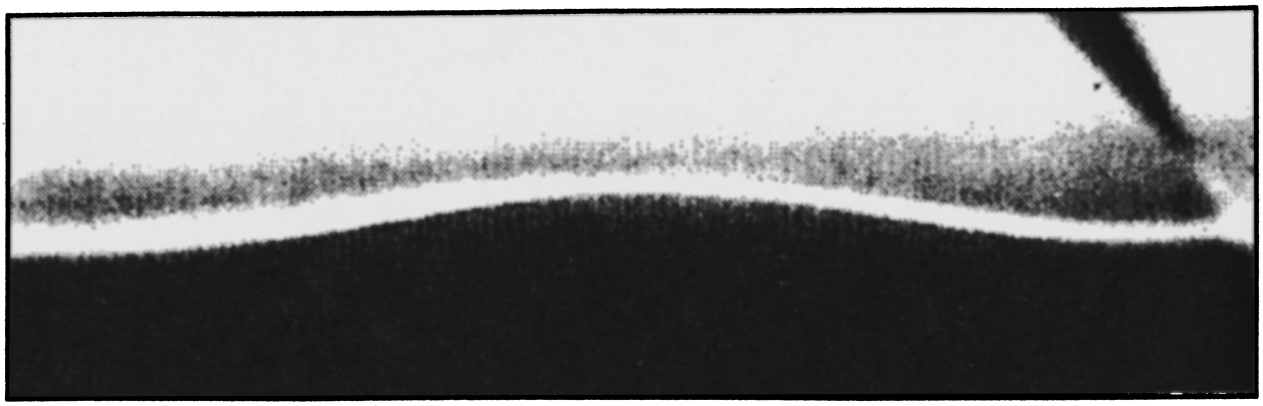

FIG. 1. Profile of the charged surface of liquid hydrogen at $U=1\,620$ V and $T=17$ K. The ''hump'' is clearly seen at the center. The linear dimension of the photograph in the horizontal position is 10 mm.

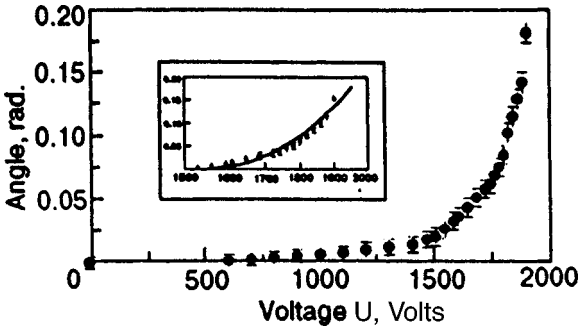


FIG. 2. Field dependence of the laser beam maximal reflection angle from the surface of the ''hump'' at $T=14.6$ K.

the walls of the container. The guard ring and the radioactive source formed a cup in which the hydrogen was condensed. A metallic collector 25 mm in diameter (control electrode) was placed above the radioactive source. The distance from the source to the collector was 6 mm.

In the diode D2 a 3-mm-diameter charge source was placed on the upper copper plate of the diode, on which the hydrogen was condensed. The source-to-lower plate distance was 3 mm. The sign of the charges on the surface of the liquid was dictated by the polarity of the applied voltage U. The properties of the positively charged surface were investigated experimentally. The shape of the charged surface was controlled visually with a TV camera, and a change in the curvature of the charged surface was determined from the deflection of the laser beam, which was reflected from the surface.

### 3. RESULTS

At small voltages between the diode plates the equipotentially charged surface of liquid wetting lower plate of the diode D1 is curved smoothly. Once a certain critical voltage $U_{c1}$ is reached, a macroscopic hump appears with a characteristic diameter of several millimeters (Fig. 1). It should be noted that the reconstructed region could occur at the random sites of the surface. In the runs the solitary hump could be shifted toward the diode center by slightly changing the tilt of the cell.

The height of the deformed surface region (hump) at the diode center could be controlled by changing the voltage between the plates within $V=1300-1700$ V. At voltages $U$ below the threshold voltage ($U_{c1}\approx 11300$ V at the given temperature) no surface reconstruction was observed. As the voltage was increased to 1750 V, the reconstructed surface lost its stability, and a discharge pulse was observed (second critical voltage $U_{c2}$). In the course of a discharge about $10^8$ charges arrive at the collector. After the discharge the surface relaxes to the original flat state and then the process is repeated. We have reported earlier on our observations of quasiperiodic oscillations of a charged surface of liquid hydrogen.[11] An analogous phenomenon—the occurrence of ionic jets (geysers) on the surface of superfluid helium in strong nonuniform fields—was observed in Ref. 12.

Figure 2 illustrates the voltage dependence of the maximal value of the reflection angle $\beta$ of the laser beam from the surface of liquid measured at the temperature of 14.6 K. The dependence of the reflection angle on the control voltage $\beta(U)$ was found to change considerably at voltages in excess of the first critical voltage (in these measurements $U_{c1}\approx 1500$ V).

Figure 3 shows another situation: the equilibrium profile of the film wetting the upper plate of the diode D2 at a voltage $U=1300$ V between the plates and temperature $T=15$ K.

It should be emphasized that the volume of the liquid film does not change with increasing voltage. When the voltage increases, the shape of the film transforms gradually from a flat film to a new drop-like film. The height of the droplet increases and the visible diameter of its base decreases. At a voltage above 2000 V a pulse discharge is been observed.

Figure 4 shows the voltage dependence of the height of the droplet. In contrast to the dependence shown in Fig. 2,

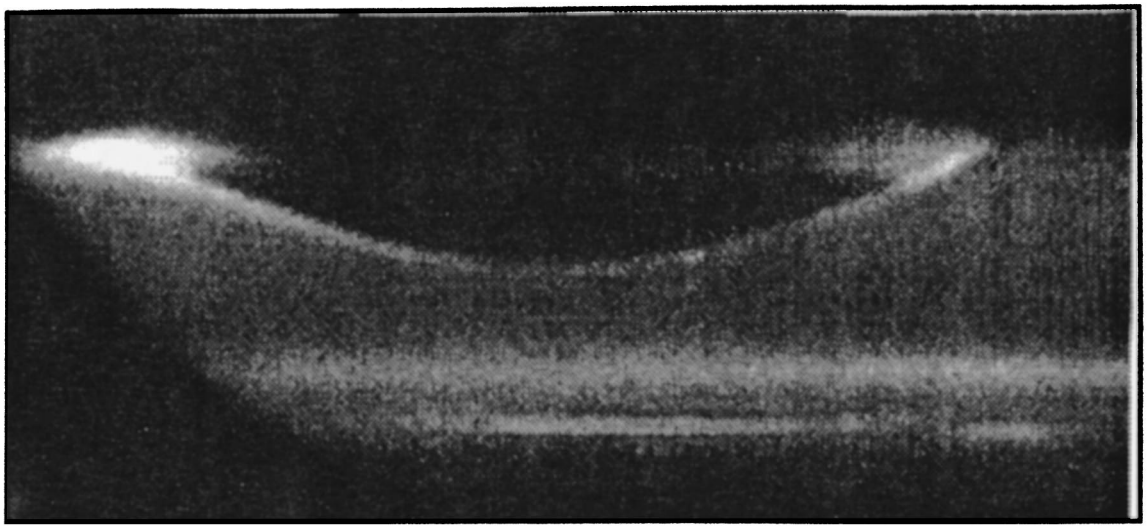

FIG. 3. Photographe of the profile of the charged surface of the film condensed on the upper plate of the diode. The voltage $U=1\,300$ V, $T=15$ K.

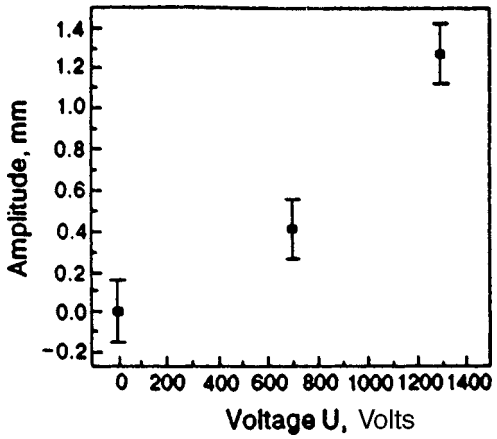


FIG. 4. Field dependence of the height of the droplet created at the upper plate of the diode, $T=15$ K.

here we observe a rapid increase of the height at small voltages.

Since in this ''inverse'' geometry the power of the charge source was not very high, we had to wait for several minutes until the charge density reached its equilibrium value and could compensate completely for the external electric field. This circumstance enabled us to record the evolution of the profile of the surface for the conditions under which the charges did not compensate the applied field.

The shape of the droplet shown in Fig. 5 differs significantly from the profile shown in Fig. 1. Here charges accumulate at the center of the droplet. In Fig. 6 we show the profile of this droplet which was obtained by scanning the photograph in Fig. 5. This situation seems to be analogous to the case of the formation of an individual dimple on the surface of liquid helium with a fixed number of electrons above the surface studied earlier.[13] In a field higher than the critical field (near 2800 V) the surface loses its stability and a discharge takes place. This process can be repeated at a constant voltage.

## 4. DISCUSSION

The experimental situation in our work is qualitatively different from the situation that has been observed in Ref. 13 and discussed in Refs. 3 and 4. In our experiments the charge density is governed by the applied voltage: the charges completely compensate for the external electric field, and their density is equal to the maximum allowable value $n=n_c=E^2/4\pi$, throughout the surface, whereas in Ref. 13 the charge density on the flat surface away from the reconstructed region (dimple) is close to zero, $n \ll n_c$. In addition, in our case the total number of charges localized near the surface is not fixed and it increases with increasing applied voltage.

The observations show that the lifetime of the reconstructed surface of hydrogen is many times longer than the characteristic time of charging and discharging of the surface. This implies that there exists a stationary charged solitary wave (hump).

The authors of Ref. 9 considered the one-dimensional case, which corresponds to the formation of a periodic system of ''rolls'' on an infinite surface of a thin helium film $d \ll \lambda$ at a field exceeding a critical field. The shape of a solitary roll ($1D$ soliton), which corresponds to an infinitely long period (for the experiment, much greater than the diameter of the experimental cell), is described by the expression

$$z(x)=A\ \cosh^{-2}(x/R), \tag{1}$$

where $A$ is the amplitude, and $R$ is the characteristic dimension of the soliton.

Nevertheless, it turned out that the shape of the hump observed in experiments with liquid hydrogen can be described satisfactory by expression (1), provided that the hump is axisymmetric and $x$ is replaced by the distance $r$ from the center of the soliton. Then $R$ is the characteristic radius of the soliton. Numerical fitting of the profile of the hump yielded the values $A=0.38$ mm and $R=2.5$ mm (the solid curve in Fig. 7).

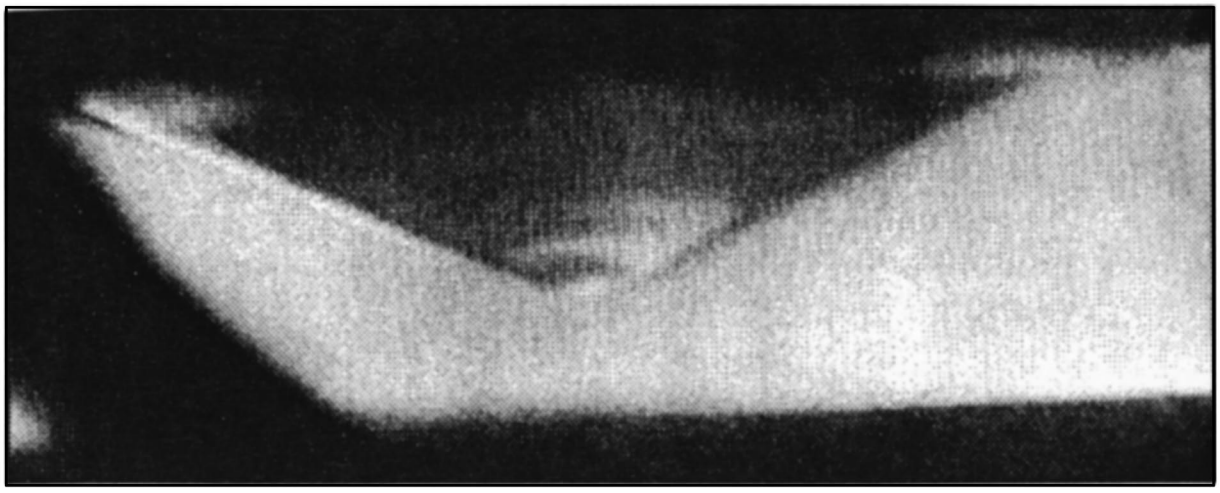

FIG. 5. Profile of the surface of the droplet wetting the upper plate. The charges have accumulated at the center of the droplet. $U=2200$ V, $T=15$ K.

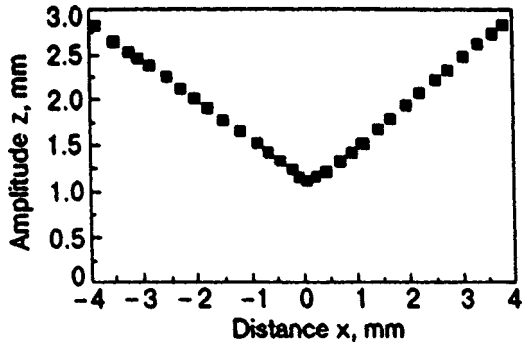


FIG. 6. Profile of the charged surface of the droplet shown in Fig. 5. Plots are the results of scanning.

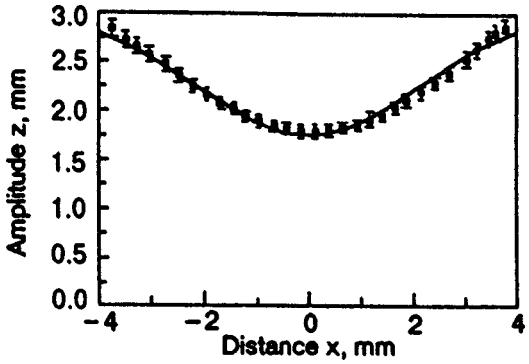


FIG. 8. Profile of the droplet obtained by scanning the photograph shown in Fig. 3. Dark squares—experiment; solid line—theory.

The evolution of the shape of the hump with increasing applied voltage can be seen from the dependence $\beta(U)$. The plot in Fig. 2 illustrates that there exist two different regimes of alteration of the shape of a free surface of the liquid—below and above the first critical voltage $U_{c1}$. The initial part ($U<U_{c1}$) corresponds to the usual drawing of the charged liquid into the field of the capacitor. In this case the reflection angle is proportional to the square of applied voltage, $\beta \propto U^2$. In fields above the first critical field, i.e., in the region $U_{c1}<U<U_{c2}$, the experimental dependence can be described by the relation

$$\beta(U) \propto (U^2/U_{c1}^2 - 1)^{3/2}/U^2, \tag{2}$$

which follows from theoretical consideration of the hump on the surface of a thin liquid layer.[9] The insert in Fig. 2 compares the experimental data in fields higher the first critical field with the theoretical dependence $\beta(U)$. This section of the curve $\beta(U)$ describes the change in slope of the lateral surface of the soliton with increasing voltage $U$. Fitting the theoretical curve to the experimental data gives the first critical field, $U_{c1}=1500$ V. The results are found to be in good agreement with the theoretical estimation from Ref. 8.

Let us now discuss the results of the experiments with a liquid layer covering the upper plate of the diode. Figure 8 illustrates the results of scanning the photograph of the profile of the charged surface of the droplet condensed on the upper plate of the diode, shown in Fig. 3. The solid curve presents the trial function $f(x)=A\ \exp(-x^2/R^2)$ with the fitting parameters $A=1.25$ mm and $R=3$ mm. The trial function describes satisfactorily the experimental data, and the effective radius $R$ coincides with the capillary length of liquid hydrogen.

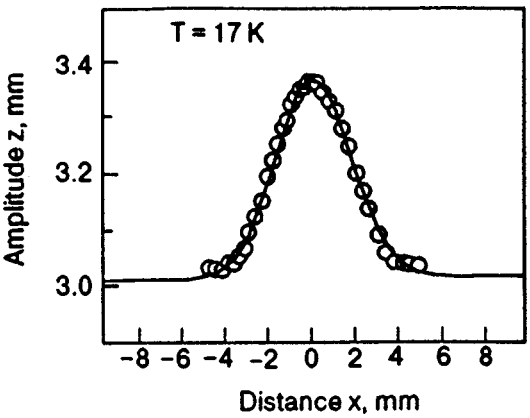


FIG. 7. Profile of the hump, obtained by scanning the photograph shown in Fig. 3 (circles). Solid line—the function (1) with the parameters $A=0.38$ mm, $R=2.5$ mm.

## 5. CONCLUSIONS

From the results of experiments on the diode D1 (Figs. 1, 2 and 7) we conclude that 1) The reconstruction of a charged surface in a static electric field in a cell of finite diameter at $d \sim \lambda$ is possible at variable number of charges and 2) Under the conditions when the charge density on the equipotential surface is governed by an external field, in fields exceeding the critical value $U_{c1}$, a solitary stationary wave (hump) appears on the surface. As the field is further increased the impulse discharge is observed; i.e., there exists the second critical field $U_{c2}$, above which the reconstructed surface of the liquid is unstable.

From the field dependence shown in Fig. 4 it follows that in the case of the film that covers the upper plate of the horizontal diode the first critical field equals to zero and direction of the free fall acceleration affects crucially the evolution of the charged surface shape in the external electric field.

This work was supported in part by a Grant from NASA-RSA, Project No. TM-17.

*E-mail: levch@issp.ac.ru

[1] L. D. Landau and E. M. Lifshitz, *Electrodynamics of Continuous Media*, Nauka, Moscow (1982).
[2] L. P. Gor'kov and D. M. Chernikova, JETP Lett. **18**, 68 (1973); DAN USSR, **228**, 829 (1976).
[3] V. I. Mel'nikov and S. V. Meshkov, Zh. Éksp. Teor. Fiz. **82**, 1910 (1982).
[4] V. B. Shikin and Yu. P. Monarkha, *2D Charge Systems in Helium*, Nauka, Moscow (1989).
[5] P. Leiderer, Phys. Rev. B **20**, 4511 (1979).
[6] M. Wanner and P. Leiderer, Phys. Rev. Lett. **42**, 315 (1979).
[7] P. Leiderer and M. Wanner, Phys. Rev. Lett. **A73**, 185 (1979).
[8] D. M. Chernikova, Fiz. Nizk. Temp. **2**, 1374 (1976).

[9] V. B. Shikin and P. Leiderer, Low Temp. Phys. **23**, 2 (1997).
[10] A. A. Levchenko, G. V. Kolmakov, L. P. Mezhov-Deglin, V. B. Shikin, E. Teske, and P. Leiderer, Zh. Éksp. Teor. Fiz. **65**, 547 (1997).
[11] A. A. Levchenko and L. P. Mezhov-Deglin, Low Temp. Phys. **22**, 46 (1996).
[12] V. P. Volodin and M. S. Khaikin, Pis'ma Zh. Éksp. Teor. Fiz. **30**(**9**), 608 (1979).
[13] P. Leiderer, W. Ebner, and V. B. Shikin, Surf. Sci. **113**, 405 (1982).
This article was published in English in the original journal. It was edited by S. J. Amoretty.

# Mapping of 2*D* contact perturbations by electrons on a helium film

E. Teske and P. Wyder

*Grenoble High Magnetic Field Laboratory, Max-Plank Institut fur Festkorperforschung Centre National de la Recherche Scientifique, B.P. 166, F-38042, Grenoble, Cedex 9, France*

P. Leiderer

*Fakultät für Physik, Universität Konstanz, D-78434 Konstanz, Germany*

V. Shikin

*Institute of Solid State Physics, 142432 Chernogolovka, Moscow District, Russia**

Fiz. Nizk. Temp. **24**, 163–165 (February 1998)

A promising way to investigate 2*D* contact phenomena is proposed. This method is based on the idea of depositing surface state electrons (SSE) on a thin layer of liquid helium covering the surface of a solid sample containing a 2*D* charge carrier system. The density of SSE adjusts to screen contact-induced perturbations of the electrostatic potential across the sample. As a result, the helium layer thickness varies due to the variation of the electrostatic pressure, thus providing a map. This map may be read off interferometrically by a technique already employed for the investigation of multi-electron dimples on helium. We have realized this mapping for a structured electrode as a test sample to demonstrate the resolution of the method.
 [S1063-777X(98)01502-3]

Contact phenomena are well known in 3*D* metal and semiconductor physics.[1,2] We have in mind, e.g., the determination of work function for different 3*D* metals, the solution of the Shottky barrier problem and applications of this solution to different aspects of transistor physics, in particular the creation of heterostructures, etc. In all these cases the perturbation of electron density near the boundary between the contacting metals or semiconductors is well localized within the so called Debye radius.

The same reasons as in 3*D* systems lead to electron density contact perturbations in 2*D* conducting structures. However, due to the peculiarities of low dimensional screening this perturbation falls off as $1/x$ and hence has no special localization length. As a result, the use of metallic source-drain terminals, which is typical of 2*D* transport measurements, leads to perturbations of the electron density practically along the entire 2*D* system. It is evident that this phenomenon is very important for different transport problems in low dimensional electron systems, for example, the quantum Hall effect, different size effects, etc.

One promising way for the investigation of 2*D* contact phenomena is based on the idea of depositing electrons on a liquid helium film condensed onto the surface of a 2*D* sample in the presence of metallic terminals. The density of this classical 2DEG which adjusts to screen the potential from the sample provides a map. This charge density map may be read by optically measuring the variation in film thickness produced by the electrostatic pressure due to the

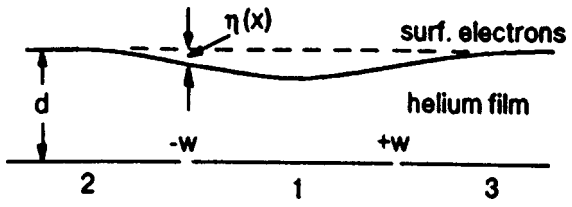


FIG. 1. Geometry and notations of the mapping problems with the electrons on helium film.

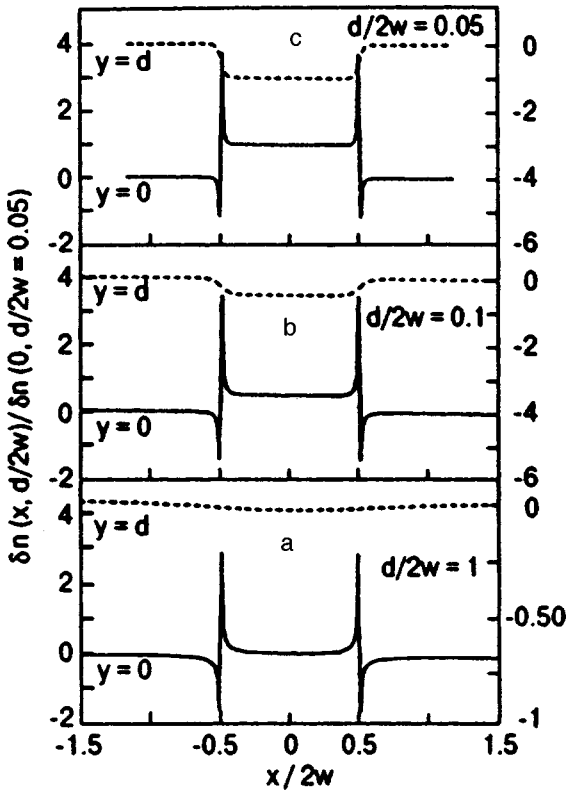


FIG. 2. Charge distribution along the gated Corbino disk with the potential perturbation between the electrodes *2-1-3* for different screening levels $d/w$. Here $2w$ is the width of the central Corbino part, $d$ is the thickness of the helium film (dielectric spacer). Solid lines correspond to Corbino sample. Dashed lines show the gate charge distribution. All density distributions are normalized to the distribution with the ratio $d/w = 0.01$.

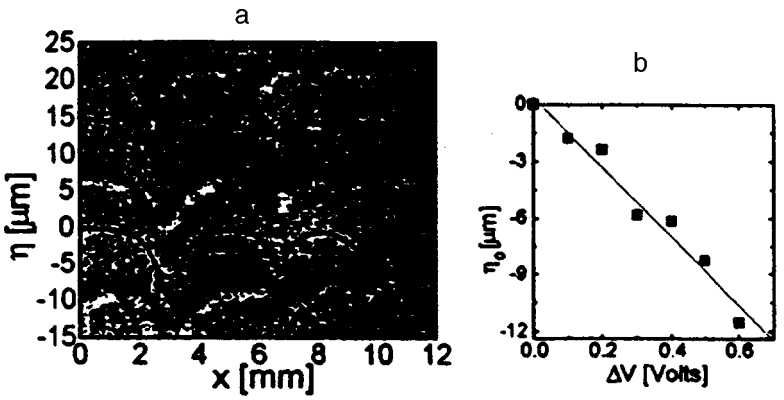


FIG. 3. Calculations compared to the experimental image. Four perturbations in these figures correspond to different $w$ (1; 0.5; 0.2; and 0.1 mm) (a). Measured helium film deformation depth against the applied perturbation voltage $\Delta V$ for $2w=1$ mm, $d=100$ $\mu$m (b).

charges, a technique already employed for the investigation of multi-electron dimples on helium.[3]

One favourable detail of the presented method is its realization under dc conditions. The existing alternative technique based on the linear electro-optic effect already used for the mapping of $2D$ potential distributions[4–6] needs an ac perturbation. Besides the electrons on a helium film could realize the mapping without total screening of the $2D$ electric potential distribution while the linear electro-optic effect is realized in the presence of an additional gate only.

In this paper we investigate the possible use of charged helium films for the mapping of model potential perturbations and demonstrate that this technique proves to be very promising for the applications outlined above.

**A.** Let us start from the solution of the electrostatic problem for a gated Corbino sample schematically shown in Fig. 1.

In the presence of electro-potential difference $\Delta V$ between the strip *1* and terminals *2* and *3* we have the following electron density distributions along the Corbino system for different screening levels (see Fig. 2a–2c). If Corbino is practically ungated (Fig. 2a), the extra electrons are distributed mainly between the electrodes *2-1-3*. The integral neutrality requirement is then fulfilled without taking the gate into account.

In the opposite limit (Fig. 2c) the gate screening comes in, and the central Corbino part *1* has an essential, practically uniform fraction of extra electrons. The corresponding compensation charge is distributed mainly along the gate. This interesting peculiarity of $2D$ contact phenomena is important for interpretation of many experimental results, e.g., the edge nature of minimal magnetocapacitance,[7] unusual $S$d$H$ oscillations in a gated Corbino disk,[8] etc. The same density distribution peculiarity is important for the potential mapping by electrons on helium film.

**B.** The point is that a non-uniform electron density distribution along the gate leads to a nonuniform deformation of the helium film, which could cover the Corbino sample (see Fig. 1) and this deformation can be detected optically using well-known methods.[3,9] Therefore the mapping of non-uniform potential perturbations along the $2D$ electron system by electrons on the helium film is reduced to two steps. First, a charged helium film with a given $2D$ system as a substrate is prepared, and second the optical technique[3,9] is applied to study the helium film deformation caused by a non-uniform electron distribution along the helium film due to the screening redistribution of these electrons in the presence of potential perturbations in $2D$ electron system. Realization of this program for the system shown in Fig. 1 is presented in Fig. 3 where Fig. 3a shows the comparison between the optical image $\eta(x)$ of the deformed helium film via $\Delta V \neq 0$ perturbation and corresponding calculations of $\eta(x)$ using the solution of Poisson and mechanic equilibrium equations. Figure 3b demonstrates a linear behavior of the helium film deformation $\eta(0)$ versus applied voltage $\Delta V$. Solid line in this figure corresponds to the calculations of $\eta(0)$ without adjustable parameters.

**C.** The above information leads to the conclusion that mapping of $2D$ contact perturbations by electrons on a liquid helium film has good prospects. This method is suitable for a general presentation of the potential map. In addition, it can be useful to extract quantitative information about the details of low dimensional contact phenomena.

Some qualitative conclusions follow from the curves plotted in Fig. 2. These results show that in the absence of an additional gate a non-uniform electron density is developed along the entire $2D$ electron system. In the presence of an additional gate, this perturbation is mainly uniform, but it still extends along the whole $2D$ system.

**D.** This activity is partly supported by INTAS 93-939 and by NASA-PSA NAS 15-10110, Project TM-17.

*E-mail: shikin@issp.ac.ru

[1] L. D. Landau and E. M. Lifshitz, *Electrodynamics of Continuous Media*, Pergamon Press, Oxford, 1960.
[2] S. M. Sze, *Physics of Semiconductor Devices*, John Wiley and Sons, New York, Chichester, Brisbane, Toronto, Singapore (1981).
[3] P. Leiderer, W. Ebner, and V. Shikin, Surf. Sci. **413**, 405 (1982).
[4] P. F. Fontein, P. Hendriks, F. A. P. Blom, I. K. Wolter, L. I. Giling, and C. W. I. Beenaker, Surf. Sci. **963**, 91 (1992).
[5] R. Knott, W. Dietsche, K. V. Klitzing, K. Plong, and K. Eberle, Semicond. Sci. Technol. **10**, 117 (1995).
[6] W. Dietsche, K. V. Klitzing, and U. Ploog, Surf. Sci. **361/362**, 289 (1996).
[7] S. Takaoka, K. Oto, H. Kurimoto, K. Murase, K. Gamo, and S. Nishi, Phys. Rev. Lett. **72**, 3080 (1994).
[8] V. T. Dolgopolov, A. A. Shashkin, G. V. Kravchenko *et al.*, Pis'ma ZhETF **63**, 55 (1996) [JETP Lett. **63**, 50 (1996)].
[9] D. Savignac and P. Leiderer, Phys. Rev. Lett. **49**, 1869 (1982).

This article was published in English in the original journal.

# Experimental and theoretical studies of levitated quantum fluids

J. Schmidt, J. W. Halley, and C. F. Giese

*School of Physics and Astronomy University of Minnesota, Minneapolis, MN 55455, USA**
Fiz. Nizk. Temp. **24**, 166–170 (February 1998)

We describe the opportunities for improved scientific understanding and technical manipulation of cryogenic fluids, particularly molecular hydrogen, by the use of carefully designed magnetic field configurations produced with assemblies of permanent magnets. We discuss the levitation of hydrogen in order to perfect technical means for handling this and other cryogenic fluids. The development of the techniques to be explored here provide extraordinary opportunities for improved methods for handling rocket fuels and cryogenic fluids in low gravity environments. © *1998 American Institute of Physics.* [S1063-777X(98)01602-8]

## INTRODUCTION

A variety of practical and scientific problems arise in the study and manipulation of cryogenic fluids in space because traditional techniques make use of the ambient gravitational field on earth. Here we address the possibility of attacking several of these scientific and practical problems by the use of permanent magnets to control the configuration and flow of the fluid. This is a possibility because several fluids of interest, notably molecular hydrogen and helium, are diamagnetic while some others, such as oxygen are paramagnetic. In either case, the principle by which one can use magnetic field gradients to exert forces on the fluid is very well known. The advantage of such an approach in a microgravity environment is that the required field gradients are quite small and permanent magnets provide an inexpensive, compact way to provide them without power supplies and other peripheral equipment requiring human attention. Forces provided in this way can serve to replace the gravitational force when gravity is serving a useful purpose (such as causing draining) in a given application, or to manipulate fluids in unusual ways not possible on earth (for example by levitation or by flow through contactless magnetic ''pipes'' or by use of suspended droplets as accelerometers).

The study of liquid molecular hydrogen began almost a century ago when Dewar won an international race to liquify the gas.[1] Attention returned briefly to the hydrogen molecule in the 1920's when Dennison,[2–4] using quantum mechanics, accounted for anomalies in its specific heat in terms of ortho and para forms using quantum mechanics. In the seventies, studies of solid molecular hydrogen clarified the spectrum of elementary excitations to be found.[5] Engineers in such diverse applications as airplane and rocket propulsion,[6–7] fusion[8] and a hydrogen economy[9] have compiled information on the physical properties of liquid hydrogen. Calculations of the behavior of $H_2$ undergoing adiabatic expansion have been reported in Ref. 10 (variational density matrix theory) and Ref. 11 (molecular dynamics). Experimentally, the group at Brown University carried out experiments on $H_2$ droplets suspended in liquid helium[12,13] which they supercooled to 10.6 K, measuring the solid nucleation rate. The experiments were used to parametrize their theory of the nucleation rate. The Brown group also reported magnetic suspension of hydrogen droplets in vacuum[14] but no supercooling experiments were reported on these droplets. Quite recently, Knuth, Schunemann and Toennies[15] reported a thermodynamic and experimental study of clusters produced through an expansion nozzle. The authors conclude that some of their clusters have masses in the range of $10^3$ to $10^4$ atoms and temperatures in the range 4.4 to 4.2 K. There have been several reports[16–19] of attempts to supercool hydrogen in the confined geometry of porous Vycor glass. Some of these reports tentatively suggest the presence of a superfluid phase while others suggest that a glass-like phase may be forming at low temperatures in the Vycor.

## DIAMAGNETIC SUSPENSION

The only report of hydrogen droplet suspension of which we are aware is the work of Paine *et al.*[14] Graphite and bismuth are also relatively easy to levitate[20,21] in an inhomogeneous magnetic field. There are also recent reports[22] by the Brown group of levitation of superfluid helium, using a superconducting electromagnet. In work at Minnesota[23] we have developed levitating magnetic field configurations obtainable with low cost permanent magnets. We use a fast locally developed computational code for the design studies. In this code, the problem of computing the fields is written

$$\nabla \cdot (1+4\pi\chi)\cdot \mathbf{H}(\mathbf{r}) = -4\pi \nabla \cdot \mathbf{M}_0 \tag{1}$$

and is solved by fast Fourier transform methods. Here $\mathbf{M}_0$ is the static magnetization of uniformly magnetized material and $\chi$ is the (highly anisotropic) susceptibility. Thus the calculation is self consistent at the linear level and takes account at this level of demagnetizing effects arising from nonuniform magnetization. The effects of such effects turn out to be small in the calculations, suggesting that the linear approximation is adequate. This is consistent with work on other designs built with the rare earth iron borides and involving very large inhomogeneities in the magnetization.[24–27] We have explored a variety of permanent magnet designs using this code and have determined that the structure shown in Fig. 1 has a satisfactory field configuration for droplet levitation and is feasible to construct. We also show the calculated potential energy per unit mass $U = pgz + (1/2)|\chi_{H_2}|^2|B|^2$ of liquid hydrogen in the resulting field configuration along the vertical axis and horizontal axes

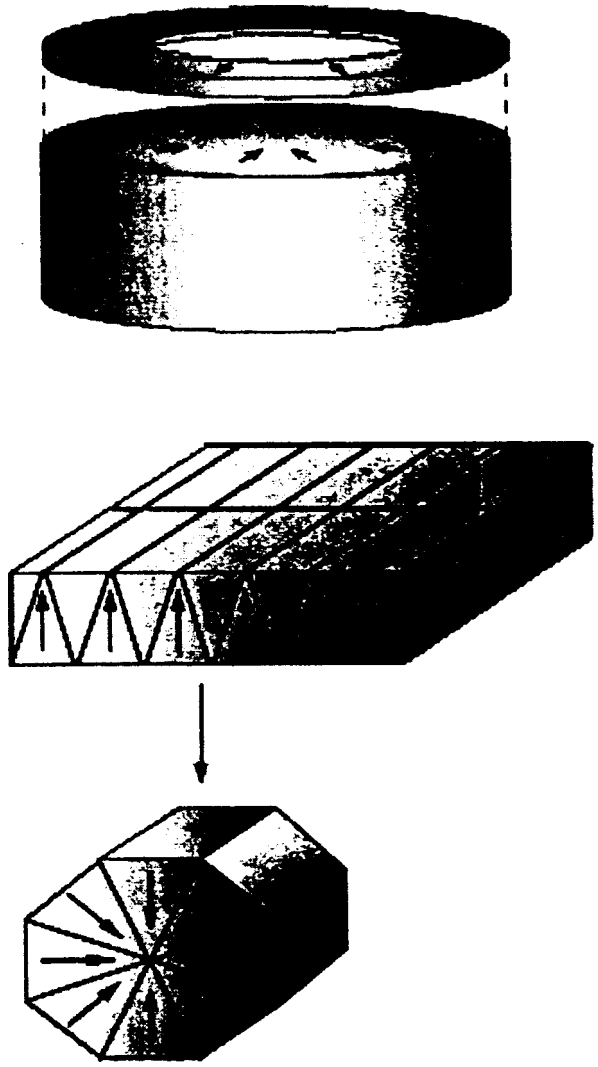

FIG. 1. Permanent magnet configuration for levitation (top) and the experimental method for approximating the ideal permanent magnet structure.

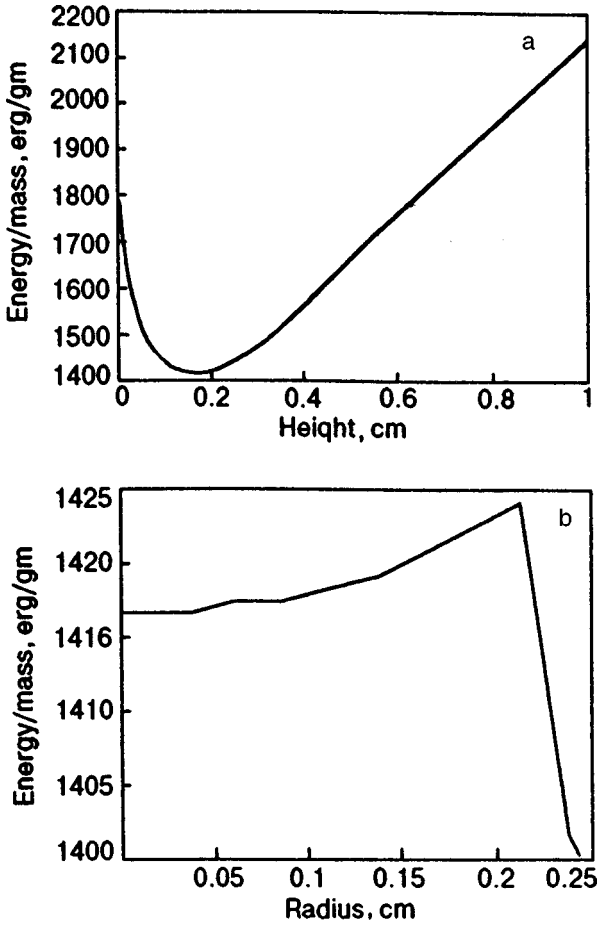


FIG. 2. Calculated energy per unit volume as a function of height (a) and radial horizontal distance from the center in the device for liquid molecular hydrogen (b).

in Fig. 2. We have built a prototype of this design, as shown in Fig. 3, using NdFeB. The apparatus which was used for assembly of this design is shown in Fig. 3b.

One may speak qualitatively of the configuration as an attempt to produce an approximation to a two dimensional magnetic monopole. This design was approximated by cutting a piece of NdFeB into pie shaped pieces as illustrated in Fig. 1, using an electric discharge machine. The device has been successfully used to suspend small particles of bismuth and, at liquid nitrogen temperatures, of ice. A photograph of a particle of bismuth levitated in the device is shown in Fig. 3a.

Not all particles of bismuth levitate successfully. However, a particle has been observed to remain levitated for periods of time greater than weeks. It can be knocked out of its stable position by a sufficiently large perturbation, after which the particle sticks to the wall formed by the cap pieces. A small push is all that is necessary to restore the particle to a state of stable levitation. If one disturbs the levitation apparatus with a gentle nudge, the particle can be perturbed from its equilibrium position and set into oscillatory motion. For small perturbations, the particle oscillated in a single line through the equilibrium position. For larger perturbations, the particle oscillated in lines that bisected different pairs of octants of the potential. A coupling between the oscillations in adjacent pairs of octants was observed and after some time, when the particle's motion was sufficiently damped, the oscillations reverted to the initial form. The position of equilibrium of the particle over the octagonal structure was slightly off-center, presumably because irregularities made the potential asymmetric. The minimum levitation height was calculated to be 1.8 mm, and the observed levitation height was between, 1.0 and 1.5 mm. When the particle was set into oscillation, the observed frequency of oscillation was approximately 5.0 Hz. In the ideal structure, there are two low amplitude mode frequencies corresponding to radial and vertical motion, of which the lower corresponds to the observed radial motion. From the ideal structure we calculate a frequency of 3.3 Hz for the radial mode. Though we have successfully levitated ice, it has not yet been possible to levitate liquid water. This may be because the magnetization is larger at liquid nitrogen temperatures. Improvements planned for this device include the production of more precisely machined and undamaged wedges and caps. Calculations show that replacing 8 wedges by 16 wedges should increase the levitation height from 75 to 90% of that for a continuous structure. Currently, video tapes of

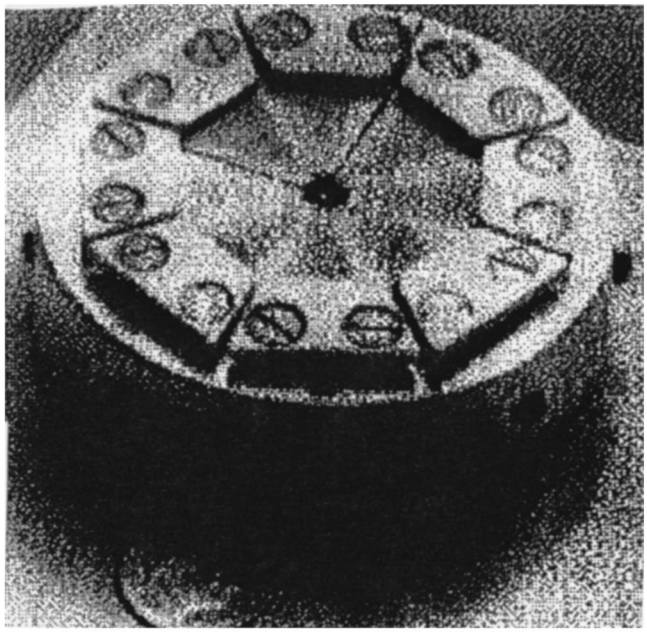

a

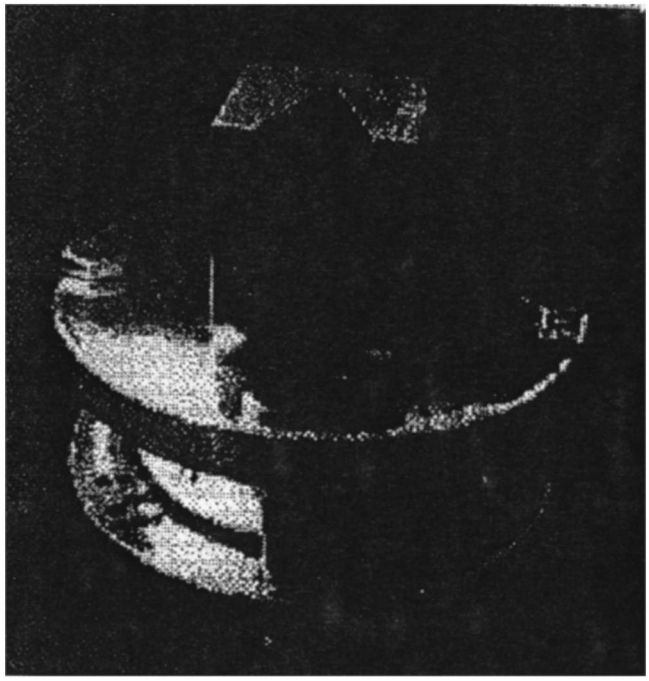

b

FIG. 3. Photographs of (a) a particle of bismuth suspended in the device and (b) apparatus used to assemble the device.

the suspended bismuth particles are being digitized for analysis in order to determine additional details concerning the nature of the particle trapping in this device.

The recent success in suspending water ice when the device was cooled to liquid nitrogen temperature shows that despite the existence of a magnetization reorientation transition[28] in NdFeB at 135 K, the device appears to levitate very successfully below the transition. This is unexpected and not fully understood, but it will simplify the practical aspects of the program considerably. In particular it may not be necessary to construct another, similar device of PrFeB (which does not have a reorientation transition[28]) in order to levitate liquid hydrogen and helium.

We calculate that we will be able to suspend a droplet of radius 3 to 4 mm. The shape will not be spherical but pancake like. We compute predicted droplet shapes from the field configurations by minimizing the energy

$$E = \int U dV + \sigma \int dA, \tag{2}$$

where $\sigma$ is the surface tension and $U$ is the energy per unit volume in the magnetic and gravitational fields (as plotted in Fig. 1). We treat the fixed volume constraint by use of a Lagrange multiplier $\lambda$ and characterize the droplet shape by the function $r(\theta,\varphi)$ and find the condition

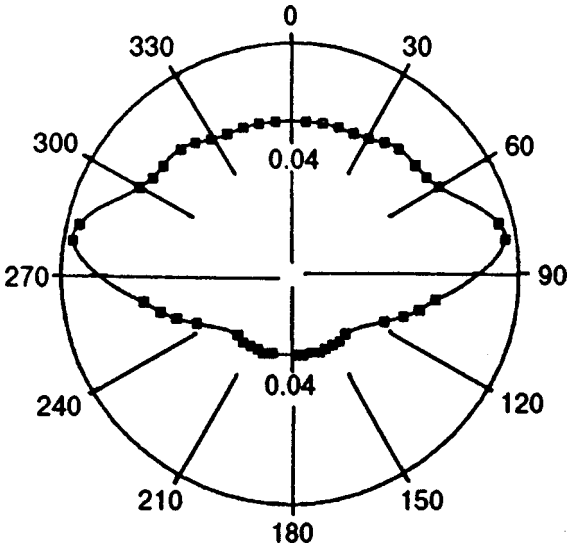


FIG. 4. Calculated cross-section of suspended hydrogen droplet (thickness is $\approx 0.04$ cm, radius (cm) vs. angle (deg)).

$$r(\theta,\varphi) = 2\sigma/(\lambda - U), \tag{3}$$

which can be solved for fixed $\lambda$ for various ''rays,'' $\theta$, $\varphi$ to give the shape when $U$ is known as a function of position. We show a calculated droplet shape in Fig. 4.

## POSSIBLE LIGHT SCATTERING STUDIES OF SUSPENDED DROPLETS

Inelastic light scattering was observed in liquid hydrogen more than 20 years ago by Fleury and McTague.[29] There is a very wide featureless spectrum which we think can be used in an ''optical thermometer,'' as described below using this phenomenon. More recently experimental work on light scattering from liquid hydrogen at pressures between 10 and 100 kbar was reported by Ulivi *et al.*[30] Light scattering from the solid phases of hydrogen has been observed by a number of authors.[31,32] The spectra show a sharp transverse phonon mode in the hcp phase and libron features in the low temperature ordered phase of solid ortho $H_2$. These features should make it quite easy to distinguish solid from liquid $H_2$ in droplets optically.

To perform the light scattering experiments, we plan to direct a laser at the droplet and detect the scattered light through optical windows in the Dewar. Several kinds of information will be gleaned from the scattered light.

### Optical measurement of temperature

The basic idea here is that, as long as the light scattering rate can be described by leading order perturbation theory in the coupling between the optical field and the system, then the ratio of the amplitude of the Stokes component $h(\omega)$ to the amplitude of the anti Stokes component $h(-\omega)$ is

$$h(\omega)/h(-\omega) = \exp(\hbar\omega\beta), \tag{4}$$

where $\beta = 1/(k_B T)$. Thus if there is a measurable scattering amplitude in the frequency region $\omega = k_B T/\hbar$ one can measure the temperature. From Ref. 29 one sees that there is a broad band of observable scattering in the region of $5-20\ \mathrm{cm}^{-1}$ of interest here. Taking into account that the grating spectrometer which we plan to use for these experiments has a spectral resolution of the order of $1\ \mathrm{cm}^{-1}$, using data in Ref. 33 to estimate uncertainties in intensity measurements, and assuming measurement times of the order of 1 s, we estimate that a temperature measurement with accuracy of a few per cent can be made with this technique. An objective of these measurements is to measure the temperature as the levitated droplet evaporates, thus subjecting the theory of ''evaporative cooling'' [34–37] to experimental test and refinement.

### Raman scattering spectrum of suspended solid and liquid samples

Though the Raman spectrum is known in both cases[29,31] it will be necessary to confirm that we can distinguish solid from liquid samples which have been levitated in the apparatus. It may be possible to make some useful studies of high frequency surface modes of the solid phases in this way, though this is not our primary objective.

### Determinations of shape and rotational state of the suspended fluids and solids

We anticipate levitated samples much larger than the wavelength of visible light and will therefore rely in the case of the liquid on measuring the droplet shape from images which can be interpreted within the approximations of geometrical optics. Our methods for calculation of droplet shape permit determination of changes in the droplet shape due to rapid rotation. By comparison of images with calculated droplet shapes we shall attempt to determine the rotational state of our levitated liquid droplets. Quantitative determination of the rotational state of suspended solid droplets is more problematical though it may be possible in the case of slow rotations to count rotational rates directly from video images.

Ultimately, we wish to explore the possibility of creating magnetic ''pipes'' to control the flow of cryogenic fluids in low gravity environments. As an example of such possibilities, we plan to produce a magnetic levitation device which will levitate a ''ring'' of cryogenic fluid (hydrogen or helium). Such a levitated ring would provide a first experimental model for a ''pipe'' in a closed circular configuration and will provide the opportunity to study the flow states in such a ''pipe.'' We are quite sure that such configurations are possible with only very modest modifications of the design described above, because preliminary calculations showed that a ring-shaped potential well for the fluid did result from some configurations of the ''caps'' on the device shown in Fig. 1. There are several interests in a ring geometry. Relatively simple flow states may be possible in them when the fluid is in the normal state. Turbulence and viscous drag should be greatly reduced, even in the normal state. In superfluid states, it might be possible to observe quantization of circulation in such rings, which could be made quite small. It is essential to make a careful study of the stability of toroidal shapes in any proposed field configuration, because

it is clear that rings with small ''aspect ratio'' of ring radius to toroidal radius will be unstable and will break into one or more droplets.

This work was supported in part by the National Aeronautics and Space administration and the University of Minnesota Supercomputer Institute.

*E-mail: woods@jwhp.spa.umn.edu

[1] J. Dewar, Nature (London) **59**, 526 (1899); *Smithsonian Report* 1900, 259 (1900).
[2] D. M. Dennison, Proc. R. Soc. London **115**, 483 (1927).
[3] K. F. Bonhoeffer and P. Harteck, Z. Phys. Chem. Abt. B **4**, 113 (1929).
[4] A. Eucken and K. Hiller, Z. Phys. Chem. Abt. B **4**, 142 (1929).
[5] I. F. Silvera, in *Proc. of LT 14*, North-Holland, Amsterdam (1975).
[6] T. L. Hardy and M. V. Whalen, *Slush Hydrogen Propellant Production, Transfer and Expulsion*, NASA Technical Memorandum 105191, AIAA-91-3550 (1991).
[7] F. J. Edeskuty, J. B. Hensall, and J. R. Bartlit, Cryogenics Ind. Gases. **4**, 36 (1969).
[8] P. C. Souers, *Cryogenic Hydrogen Data Pertinent to Magnetic Fusion Energy*, Lawrence Livermore Laboratory Report UCRL-52628 (1979).
[9] F. J. Edeskuty *et al.*, *Critical Review and Assessment of Problems in Hydrogen Energy Delivery Systems* Los Alamos Report LA-7405-PR (1978).
[10] M. L. Ristig, G. Senger, and K. E. Kurten, *Recent Progress in Many Body Theories*, Plenum, NY (1988), Vol. 1, p. 197.
[11] A. Vicentini, G. Jacucci, and V. R. Pandharipande, Phys. Rev. C **31**, 1783 (1985).
[12] G. M. Seidel, H. J. Maris, F. I. B. Williams, and J. G. Cardona, Phys. Rev. Lett. **56**, 2380 (1986).
[13] H. J. Maris, G. M. Seidel, and F. I. B. Williams, Phys. Rev. B **36**, 6799 (1987).
[14] C. G. Paine and G. M. Seidel, Rev. Sci. Instrum. **62**, 3022 (1991).
[15] E. L. Knuth, R. Schunemann, and J. P. Toennies, J. Chem. Phys. **102**, 6258 (1995).
[16] D. F. Brewer, J. Rajendra, N. Sharma, and A. L. Thomson, Physica B **165–166**, 569 (1990).
[17] D. F. Brewer, J. C. N. Rajendra, and A. L. Thomson, Physica B **194–196**, 687 (1994).
[18] R. H. Torii, H. J. Maris, and G. M. Seidel, Phys. Rev. B **41**, 7167 (1990).
[19] J. de Kinder, A. Bousen, and D. Shoemaker, Phys. Lett. A **203**, 251 (1995).
[20] B. R. F. Kendall, M. F. Vollero, and L. D. Hinkle, J. Vac. Sci. Technol. A **5**, 2458 (1987).
[21] G. T. Gillies, European J. Phys. **12**, 54 (1991).
[22] H. Maris and G. Seidel, private communication.
[23] J. Schmidt, *Master's thesis*, University of Minnesota (1996) (unpublished).
[24] H. A. Leupold *et al.*, in *High Performance Permanent Magnetic Materials*, S. G. Sankar (Ed.), Vol. 36 of MRS Symp. Proc. MRS, Pittsburg (1987), p. 279.
[25] E. Potenziani, J. P. Clarke, and H. A. Leupold, J. Appl. Phys. **61**, 3466 (1987).
[26] H. A. Leupold, E. Potenziani II, D. J. Basarab, and A. Tilak, J. Appl. Phys. **67**, 4650 (1990).
[27] H. A. Leupold, E. Potenziani II, and A. Tauber, J. Appl. Phys. **67**, 4656 (1990).
[28] C. Abache and H. Oestereicher, J. Appl. Phys. **57**, 4112 (1985).
[29] P. A. Fleury and J. P. McTague, Phys. Rev. Lett. **31**, 914 (1973).
[30] L. Ulivi, F. Barrochi, and G. Pratesi, Acoust. Phys. **309**, pt. 1, 869 (1990).
[31] F. Silvera, W. N. Hardy, and J. P. McTague, Phys. Rev. B **5**, 1578 (1972).
[32] I. Silvera, in *Correlation Functions and Quasiparticle Interactions*, J. W. Halley (Ed.), Plenum, NY (1978), p. 603.
[33] W. F. Vinen and D. L. Hurd, Adv. Phys. **27**, 534 (1978).
[34] J. Farges, M. F. DeFeraudy, B. Raoult, and G. Torchert, Surf. Sci. **106**, 95 (1981).
[35] J. Gspann, in *Physics of Electronic, and Atomic Collisions*, S. Datz (Ed.), North Holland, Amsterdam (1982), p. 79.
[36] D. M. Brink and S. Stringari, *Atoms, Molecules and Clusters* **15**, 257 (1990).
[37] C. E. Klots, Z. Phys. D **5**, 83 (1987); Z. Phys. D **20**, 105 (1991).

This article was published in English in the original journal.

# Electrical charging of helium and hydrogen droplets

Tito E. Huber and Frank Boccuzi

*Polytechnic University, Brooklyn, New York, 11201**
Fiz. Nizk. Temp. **24**, 171 (February 1998)

[S1063-777X(98)01702-2]

The cryogenic fluids helium and hydrogen are versatile prototype fluids as they have important fundamental properties. Many of these properties are influenced by the boundary conditions that prevail at the container walls. These effects can be minimized in droplets. By creating a superfluid helium sample in the near-zero gravity of the orbiting shuttle, superfluid droplet dynamics can be studied for the first time. Also, the extent of supercooling of liquid hydrogen droplets can be investigated under such favorable conditions and we can attempt to make a superfluid molecular hydrogen droplet.

Changed droplets can be levitated by using the quadrupole trap. In this paper we show that weakness of the electron bond to hydrogen and helium means that for a reasonable trapping field, the largest molecular hydrogen droplet that can be levitated on the ground is 6 micrometers in diameter. For helium, the maximum particle size is even smaller. Positive ions can strongly attach to helium and positively charged droplets appears possible on the ground. However, the ''snowballs'' produced by the ionic electrostriction are likely to pin and affect the superfluid form helium. In particular, ions can compromise the proposed rotational superfluid dynamics experiments by nucleating vortices. Ions are also likely to spoil the supercooling of hydrogen. On the other hand, the droplets can be very large, macroscopic, under microgravity conditions. In fact, in that case the droplet diameter can be as large as 1 mm for hydrogen.

Specific issues discussed in this paper are, 1) injection and positioning of droplets in a microgravity environment and, 2) electronic and ionic charging and, 3) conditions of size and temperature for charge holding.

Although we specifically target the quadrupole trap, and the magnetic trap only indirectly, we shall demonstrate that this work is relevant to all cryogenic droplet experiments in microgravity because the shuttle is a medium-to-high radiation environment and spontaneous charging of dielectric interfaces is an issue.

*E-mail: thuber@photon.poly.edu

This article was published in English in the original journal.

  

# Simulation of quantum field theory and gravity in superfluid $^3$He

G. E. Volovik*

*Helsinki University of Technology, Low Temperature Laboratory, P.O. Box 2200, FIN-02015 HUT, Finland***

Fiz. Nizk. Temp. **24**, 172–175 (February 1998)

Superfluid phases of $^3$He are quantum liquids with the interacting fermionic and bosonic fields. In many respects they can simulate the interacting quantum fields in the physical vacuum. One can observe analogs of such phenomena as axial anomaly, vacuum polarization, zero-charge effect, fermionic charge of the vacuum, baryogenesis, ergoregion, vacuum instability, etc. We discuss some topics using as an example several linear defects in $^3$He-*A*: (1) disgyration, which simulates the extremely massive cosmic string, (2) singular vortex, which is analogous to the spinning cosmic string, and (3) continuous vortex, whose motion causes the «momentogenesis» which is the analog of baryogenesis in early Universe. The production of the fermionic momentum by the vortex motion (the counterpart of the electroweak baryogenesis) has been recently measured in Manchester experiments on rotating superfluid $^3$He-*A* and $^3$He-*B*. To simulate the other phenomena, one needs a rather low temperature and high homogeneity, which probably can be attained under microgravity conditions. © *1998 American Institute of Physics.* [S1063-777X(98)01802-7]

## 1. INTRODUCTION. RELATIVISTIC FERMIONS IN $^3$He-*A*

We will give several examples of the analogy between high-energy physics and superfluid $^3$He. We consider three types of topologically stable, linear defects in $^3$He-*A*, which exhibit the properties of different types of cosmic strings. The ''gravity'' and the axial anomaly in the presence of such defects are discussed.

The quasiparticles in $^3$He-*A* are chiral and massless fermions. Close to the gap nodes, i.e., at $\mathbf{k}\approx \pm p_F\hat{\mathbf{l}}$ ($\hat{\mathbf{l}}$ is the unit vector in the direction of the gap nodes in the momentum space) the energy spectrum $E(\mathbf{k})$ of the gapless *A*-phase fermions is ''relativistic'':[1]

$$E^2(\mathbf{k}) = g^{ik}(k_i - eA_i)(k_k - eA_k). \tag{1.1}$$

Here the ''vector potential'' $\mathbf{A}$ is dynamical: $\mathbf{A}=k_F\hat{\mathbf{l}}$, $e=\pm 1$, and the metric tensor is

$$g^{ik} = c_\perp^2(\delta^{ik} - l^i l^k) + c_\parallel^2 l^i l^k, \tag{1.2}$$

where $c_\perp = \Delta/p_F$ and $c_\parallel = v_F$ (with $c_\perp \ll c_\parallel$) are ''speeds of light'' propagating transversely to $\hat{\mathbf{l}}$ and along $\hat{\mathbf{l}}$, respectively; $k_F$ is the Fermi momentum; $v_F = k_F/m_3$ is the Fermi velocity; $m_3$ is the mass of $^3$He atom, and $\Delta \ll k_F v_F$ is the gap amplitude in $^3$He-*A*.

In the presence of superflow with the superfluid velocity $\mathbf{v}_s$ the following term is added to the energy $E(\mathbf{k})$:

$$\mathbf{k}\cdot\mathbf{v}_s \equiv (\mathbf{k} - e\mathbf{A})\cdot\mathbf{v}_s + eA_0, \quad A_0 = k_F\hat{\mathbf{l}}\cdot\mathbf{v}_s. \tag{1.3}$$

The second term corresponds to the scalar potential $A_0$ of the ''electromagnetic field'' and the first term leads to the nonzero element $g^{0i} = v_s^i$ of the metric tensor. As a result, Eq. (1.1) transforms to

$$g^{\mu\nu}(k_\mu - eA_\mu)(k_\nu - eA_\nu) = 0, \tag{1.4}$$

where $k_\mu = (\mathbf{k}, E)$, $A_\mu = (\mathbf{A}, A_0)$, and the metric tensor

$$g^{00} = -1, \quad g^{0i} = v_s^i,$$

$$g^{ik} = c_\perp^2(\delta^{ik} - l^i l^k) + c_\parallel^2 l^i l^k - v_s^i v_s^k. \tag{1.5}$$

## 2. DISGYRATION AS A COSMIC STRING. CONICAL SINGULARITY

The so-called radial disgyration is one of the topologically stable linear defects in $^3$He-*A*. This is an axisymmetric distribution of the $\hat{\mathbf{l}}$ vector

$$\hat{\mathbf{l}}(r,\varphi) = \hat{\mathbf{r}}, \tag{2.1}$$

where $\hat{\mathbf{z}}$, $\hat{\mathbf{r}}$ and $\hat{\varphi}$ are unit vectors of the cylindrical coordinate system with $\hat{\mathbf{z}}$ along the axis of the defect line. The vector potential $\mathbf{A} = p_F\hat{\mathbf{r}}$ can be removed by gauge transformation since the ''magnetic'' field is zero: $\mathbf{B} = \nabla\times\mathbf{A} = 0$. Thus the radial disgyration provides only the ''gravity'' field, which acts on the $^3$He-*A* fermions, with the metric tensor

$$g^{00} = -1, \quad g^{0i} = 0,$$

$$g^{ik} = c_\perp^2(\hat{\mathbf{z}}^i\hat{\mathbf{z}}^k + \hat{\varphi}^i\hat{\varphi}^k) + c_\parallel^2\hat{\mathbf{r}}^i\hat{\mathbf{r}}^k. \tag{2.2}$$

The interval corresponding to this metric,

$$ds^2 = -dt^2 + \frac{1}{c_\perp^2}\,dz^2 + \frac{1}{c_\parallel^2}\left(dr^2 + \frac{c_\parallel^2}{c_\perp^2}\,r^2 d\varphi^2\right), \tag{2.3}$$

has a conical singularity (if $c_\perp \neq c_\parallel$), where the curvature is concentrated at the disgyration axis ($r=0$).[2,3] The space is flat everywhere outside the axis, but the length of circumference of the radius $r$ around the axis is $2\pi r(c_\parallel/(c_\perp)$. Since $c_\parallel \gg c_\perp$, this is analogous to a rather unusual cosmic string with a very big positive or negative mass $M$ per unit length:

$$4GM = 1 \pm \frac{c_\parallel}{c_\perp}, \quad 4G|M| \gg 1. \tag{2.4}$$

The correct sign should be the sign which is fixed by the fact that when $c_\parallel = c_\perp$ the geometry is flat and has to correspond to $M=0$ (I thank Matt Visser for this remark). Since the

linear mass $M=1/4G$ ($G$ is the gravitational constant) corresponds to the chain of the point masses $m$ with the distance between the neighboring masses equal to twice the Schwarzschild radius ($r_g=2Gm \quad M=m/2r_g=1/4G$), the case $|M|>1/4G$ corresponds to the chain of the overlapping black holes.

### 3. SYMMETRIC VORTEX AND SPINNING STRING

The most symmetric vortex in $^3$He-$A$ can be realized in thin films where the vector $\hat{\mathbf{l}}$ is fixed along the normal to the film and the superfluid velocity is circulating around the vortex axis:

$$\hat{\mathbf{l}}=\hat{\mathbf{z}}, \quad \mathbf{v}_s=\frac{\hbar}{2m_3 r}\,\hat{\varphi}. \tag{3.1}$$

The ''magnetic'' field and the scalar potential are absent ($\mathbf{B}=k_F\nabla\times\hat{\mathbf{l}}=0$, $A_0=0$). One has again only the gravity field, but now with the metric tensor

$$g^{00}=-1, \quad g^{0i}=\frac{\hbar}{2m_3 r}\,\hat{\varphi}^i,$$

$$g^{ik}=c_\parallel^2\hat{z}^i\hat{z}^k+c_\perp^2(\hat{x}^i\hat{x}^k+\hat{y}^i\hat{y}^k)-v_s^i v_s^k. \tag{3.2}$$

The corresponding interval is[4]

$$ds^2=-\left(1-\frac{v_s^2(r)}{c_\perp^2}\right)\left(dt+\frac{\hbar\,d\varphi}{2m_3(c_\perp^2-v_s^2(r))}\right)^2+\frac{dz^2}{c_\parallel^2}+\frac{dr^2}{c_\perp^2}+\frac{r^2d\varphi^2}{c_\perp^2-v_s^2(r)}. \tag{3.3}$$

There are two important properties of this interval:

(1) There is a region in which the velocity field $v_s(r)$ exceeds the transverse speed of light, $c_\perp$. This is the ergoregion: the vacuum in the ergoregion is unstable toward creation of particles pairs.

(2) Far from the vortex axis, where $v_s(r)$ is small and can be ignored, one has

$$ds^2=-\left(dt+\frac{d\varphi}{\omega}\right)^2+\frac{1}{c_\parallel^2}\,dz^2+\frac{1}{c_\perp^2}\,(dr^2+r^2d\varphi^2), \tag{3.4}$$

where the angular velocity

$$\omega=\frac{2m_3c_\perp^2}{\hbar}. \tag{3.5}$$

This metric corresponds to that outside the so-called spinning cosmic string,[5] which has the angular momentum in the core. In our case this is an unusual spinning string with the angular momentum $J=\hbar/(8m_3G)$ per unit length but with a zero mass.

The connection between the time and the angle in Eq. (3.4) suggests[5] that the energy $E$ and the angular momentum $J$ of fermions against the background of this spinning string are related as

$$E=J\omega. \tag{3.6}$$

The spectrum of bound states in the core of this vortex was calculated by Kopnin.[6] He found that the factor $\omega$ in Eq. (3.6) is of the same order of magnitude, although it is not equal to that in Eq. (3.5). More importantly, the calculated $\omega$ appears to be independent of the momentum $k_z$ along the vortex axis, in complete agreement with Eq. (3.5). This case is distinct from the spectrum of bound states in the core of the vortices in other systems: in $s$-wave superconductors and in $^3$He-$B$ there is an essential dependence of $\omega(k_z)$ on $k_z$.[7]

### 4. ATC VORTEX AND BARYOGENESIS

The continuous vortex, which was discussed by Chechetkin[8] and Anderson and Toulouse[9] (ATC vortex), has the following distribution of $\hat{\mathbf{l}}$ and $\mathbf{v}_s$ fields:

$$\hat{\mathbf{l}}(r,\varphi)=\hat{\mathbf{z}}\cos\,\eta(r)+\hat{\mathbf{r}}\sin\,\eta(r),$$

$$\mathbf{v}_s(r,\varphi)=-\frac{\hbar}{2m_3 r}\,[1+\cos\,\eta(r)]\hat{\varphi}, \tag{4.1}$$

where $\eta(r)$ changes from $\eta(0)=\pi$ to $\eta(\infty)=0$ in the so-called soft core of the vortex. The stationary vortex generates a ''magnetic'' field and when the vortex moves with a constant velocity $\mathbf{v}_L$, it also generates an «electric» field, since $\mathbf{A}$ depends on $\mathbf{r}-\mathbf{v}_L t$:

$$\mathbf{B}=k_F\nabla\times\hat{\mathbf{l}}, \quad \mathbf{E}=\partial_t\mathbf{A}=-k_F(\mathbf{v}_L\cdot\nabla)\hat{\mathbf{l}}. \tag{4.2}$$

The quantum vacuum with massless chiral fermions exhibits the axial anomaly: the presence of the electric and magnetic fields leads to the production of left particles from the vacuum at the rate[10,11]

$$\dot{n}=\partial_\mu j^\mu=\frac{e^2}{4\pi^2}\,\mathbf{E}\cdot\mathbf{B}. \tag{4.3}$$

In $^3$He-$A$ there are two species of fermions, left and right, with $e=\pm1$. The left quasiparticle carries the linear momentum $p_F\hat{\mathbf{l}}$, while the right-handed quasiparticle carries the opposite momentum, $-p_F\hat{\mathbf{l}}$. This asymmetry between left and right gives the net product of the fermionic linear momentum $\mathbf{P}$ in the time-dependent texture:

$$\partial_t\mathbf{P}=2\int d^3r\dot{n}p_F\hat{\mathbf{l}}=\hbar\,\frac{k_F^3}{2\pi^2}\int d^3r\hat{\mathbf{l}}(\partial_t\hat{\mathbf{l}}\cdot(\nabla\times\hat{\mathbf{l}})). \tag{4.4}$$

Integration of the anomalous momentum transfer in Eq. (4.4) over the cross section of the soft core of a moving ATC vortex gives the rate of the momentum transfer between the condensate (vacuum) and the heat bath (matter), mediated by the moving vortex:[12]

$$\partial_t\mathbf{P}=-\pi\hbar N_v C_0\hat{\mathbf{z}}\times\mathbf{v}_L. \tag{4.5}$$

Here $N_v$ is the winding number of the vortex [$N_v=-2$ in the case of Eq. (4.1)] and $C_0=k_F^3/3\pi^2$. This ''momentogenesis'' from the vacuum gives an extra nondissipative force that acts on the moving continuous vortex. This result, which was derived for the ATC vortex from the axial anomaly equation (4.3), was confirmed in the microscopic theory, which takes into account the discreteness of the quasiparticle spectrum in the soft core.[13] This was also confirmed in experiments on vortex dynamics in $^3$He-$A$,[14] where it was found that the extra force on the vortex nearly cancels the conventional Magnus force.

In the Weinberg–Salam model the similar asymmetry between left and right leads to the ''baryogenesis''—production of a baryonic charge in the presence of the SU(2) and U(1) fields. Such fields can be generated in the core of the topological defects (monopoles, domain walls, sphalerons, and electroweak cosmic strings) that evolve in the expanding Universe.[15–20] Experiments in $^3$He-$A$ and also in $^3$He-$B$,[14] where the «momentogenesis» due to the axial anomaly in the singular core has been measured in a broad temperature range, support ideas on electroweak baryogenesis in early Universe.

## 5. CONCLUSIONS. $^3$He DROPLETS IN MICROGRAVITY

We discussed here only a very small fraction of the analogies which can simulate many phenomena in particle physics and gravitation.

In superfluid $^3$He the container walls very often prevent carrying out of ''pure'' experiments. Such nonsuperfluid environment should be removed since the Universe, according to our present knowledge, has no external environment. For example, in the process of nucleation of quantized vortices (the phenomenon which is now believed to be important in the cosmological models[21]) the surface roughness of container dominates over the intrinsic nucleation. But only the latter is interesting for the cosmological community. The absence of gravity gives us a chance to produce a free droplet without the container boundaries and thus to deal with the pure intrinsic nucleation. The rotation of a free droplet of $^3$He-$A$ liquid can be made by utilizing the unique magnetic properties of superfluid $^3$He: one can apply the rotating magnetic field.

Another interesting problem, which is related to the droplets of $^3$He, is the dependence of its superfluid properties on the size of a droplet. The ex-treme case—the cluster with a small number $N$ of $^3$He atoms—corresponds to the other finite system—an atomic nucleus which also represents a cluster of fermions (protons and neutrons). These clusters have very similar properties, which are determined by their fermionic quantum statistics and interaction: shell structure, magic numbers, single and collective excitations, rotational degrees of freedom, fission and fusion, deformed and superdeformed states of clusters with large angular momentum, the superfluid (pair-correlated) properties of nuclei which evolve with increasing $N$, etc. The advantage of $^3$He clusters is that it is relatively easy to study them using the NMR technique.

I thank T. Jacobson, P. Mazur, M. Visser, and K. Rama for discussions.

*Permanent address: Landau Institute for Theoretical Physics, Moscow, Russia
**E-mail: volovik@boojum.hut.fi

[1] G. E. Volovik and T. Vachaspatl, Int. J. Mod. Phys. B **10**, 471 (1996).
[2] D. D. Sokolov and A. A. Starobinsky, Doklady AN SSSR 234, 1043 (1977).
[3] M. Banados, C. Teitelboim, and J. Zanelli, Phys. Rev. Lett. **69**, 1849 (1992).
[4] G. E. Volovik, Pis'ma ZhETF **62**, 58 (1995) [JETP Lett. **62**, 65 (1995)].
[5] P. O. Mazur, Phys. Rev. Lett. **57**, 929 (1986); Phys. Rev. D **34**, 1925 (1986); P. O. Mazur, hep-th/9611206.
[6] N. B. Kopnin, Physica B **210**, 267 (1995).
[7] C. Caroll *et al.*, Phys. Lett. **9**, 307 (1964).
[8] V. R. Chechetkin, Sov. Phys. JETP **44**, 706 (1976).
[9] P. W. Anderson and G. Toulouse, Phys. Rev. Lett. **38**, 508 (1977).
[10] S. Adler, Phys. Rev. **177**, 2496 (1969).
[11] J. S. Bell and R. Jackiw, Nuovo Cimento A **60**, 47 (1969).
[12] G. E. Volovik, Sov. Phys. JETP **75**, 990 (1992).
[13] N. B. Kopnin, Phys. Rev. B **47**, 14354 (1993).
[14] T. D. C. Bevan, A. J. Manninen, J. B. Cook *et al.*, Nature (London) **386**, 689 (1997).
[15] A. D. Dolgov, Phys. Rep. **222**, 310 (1992).
[16] A. Vilenkin and E. P. S. Shellard, *Cosmic Strings and Other Topological Defects*, Cambridge University Press (1994).
[17] M. B. Hindmarsh and T. W. B. Kibble, Phys. Rep. **58**, 477 (1995).
[18] N. Turok, in *Formation and Interactions of the Topological Defects*, A. C. Davis and R. Brandenberger (Eds.), Plenum Press, New York and London (1995).
[19] T. Vachaspati and G. B. Field, Phys. Rev. Lett. **73**, 373 (1994); **74**, Errata (1995).
[20] J. Garriga and T. Vachaspati, Nucl. Phys. B **438**, 161 (1995).
[21] V. M. H. Ruutu, V. B. Eltsov, A. J. Gill, T. W. B. Kibble, M. Krusius, Yu. G. Makhlin, B. Placais, G. E. Volovik, and W. Xu, Nature (London) **382**, 334 (1996).

This article was published in English in the original journal. It was edited by S. J. Amoretty.

# Bose–Einstein condensation and heat capacity of a nonideal gas

V. S. Yarunin

*N. Bogoliubov Laboratory of Theoretical Physics, Joint Institute for Nuclear Research, 141980 Dubna, Russia*

Fiz. Nizk. Temp. **24**, 176–179 (February 1998)

The theory of a nonideal gas developed by N. N. Bogoliubov is applied for a semiclassical description of nonlinear dynamics of Bose condensate density. Analytical calculations lead to temperature dependence of heat capacity $C_v$ typical of superfluid $^4$He at temperatures below and above the superconducting transition temperature $T_c$ except for the interval $1.6\ \mathrm{K}<T<2.2\ \mathrm{K}$. © *1998 American Institute of Physics.* [S1063-777X(98)01902-1]

Bogoliubov's model of nonideal gas is frequently applied to low-temperature ($T\sim 0$ K) states of Bose condensate. Among other things, this is due to the fact that the excitation spectrum of the model in the limit of low condensate densities $\rho\sim 0$ ($T\sim T_c$) differs significantly from the experimental spectrum. However, an analysis of semiclassical dynamics of $\rho$ in the Bogoliubov model shows that its thermodynamic properties are determined by the type of solution of nonlinear equations of motion rather than by details of the excitation spectrum. Ultimately, we can find an approximation leading to a description of heat capacity $C_v$ in accordance with experiments for superfluid $^4$He at temperatures below and above the superconducting transition temperature $T_c$ except for the interval 1.6–2.2 K.

Let us consider the Bogoliubov model for a nonideal Bose gas[1]:

$$H=h+\sum_{k\neq 0}\left[\Omega_k b_k^+ b_k+\frac{g_k}{2V}(b_k^+ b_{-k}^+ a^2+b_k b_{-k} a^{*2}+2b_k^+ b_k|a|^2)+\frac{g_0}{V}b_k^+ b_k|a|^2\right],$$

$$h=g_0\frac{|a|^4}{2V},\quad \Omega_k=\frac{k^3}{\mu},\quad \mu=2m. \tag{1}$$

Here the numerical variables $a$ and $a^*$ describe the amplitude of condensate particles with a momentum $k=0$, and $b^+$ and $b$ are the operators of creation and annihilation of particles above the condensate. The Hamiltonian $H$ has the ''semiclassical'' integral of motion[2]

$$\frac{dn}{dt}=\frac{d}{dt}\left(|a|^2+\sum_{k\neq 0}b_k^+ b_k\right)=\{H,|a|^2\}+i\left[H,\sum_{k\neq 0}b_k^+ b_k\right]=0.$$

As a result, the partition function $Q$ of the system (1) can be written in the form of an integral over trajectories with a constraint:

$$Q=\mathrm{Tr}(e^{-\beta H}\delta_{N,n})=\int d^2a\prod_{k\neq 0}\int Db_k^* Db_k\int_{-\pi}^{\pi}dy\ \exp[iy(n-N)+S(0,\beta)].$$

Considering that the Bose condensate in the partition function is a ''slow'' subsystem and integrating with respect to ''rapid'' trajectories $b_k^*$, $b_k$ above the condensate, we obtain the semiclassical effective action $S_{\mathrm{ef}}$ of the condensate[3]:

$$Q=\int d\rho d\nu\ \exp[S_{\mathrm{ef}}(\rho,\nu)],$$

$$S_{\mathrm{ef}}=-\beta V\left(\frac{g_0\rho^2}{2}-\nu\rho+\nu R\right)+cV\int k^2\left[\frac{(\omega_k-\nu)\beta}{2}-2\ln\mathrm{sh}\left(\frac{\beta E_k}{4}\right)\right]dk,$$

$$E_k=[(\Omega_k+\rho g_0-\nu)^2+2\rho g_k(\Omega_k+\rho g_0-\nu)]^{1/2},$$

$$\nu=i\frac{y}{\beta},\quad \rho=\frac{|a|^2}{V},\quad R=\frac{N}{V},\quad c^{-1}=2\pi^2 h^3.$$

The variational equations $\delta S_{\mathrm{ef}}(\rho,\nu)=0$ have the form

$$R=\rho+r,\quad \frac{\nu}{g_0}-2r=\rho\left[1-\frac{G(\rho)}{g_0}\right]. \tag{2}$$

The explicit expressions for the density $r(\rho,\nu)$ of particles above the condensate and for the effective interaction $G(\rho,\nu)$ between the condensate particles and particles above the condensate are given in Refs. 3 and 4, and $g_0$ is the interaction between the condensate particles.

Substituting the solutions of Eqs. (2) into the effective action $S_{\mathrm{ef}}$, we obtain the following expressions for the partition function $Q$ and free energy $F$:

$$Q\simeq(\sqrt{\beta g_0})^{-1}e^{S_{\mathrm{ef}}|_0},\quad F=-\frac{1}{V\beta}S_{\mathrm{ef}}\Big|_0.$$

We introduce the model of interaction between atoms of the Bose gas:

$$g_k=\begin{cases} g_0(1-k^2/k_0^2)\geqslant 0 & (0\leqslant k\leqslant k_0),\\ g_0[(k-2k_0)^2/k_0^2-1]\leqslant 0 & (k_0\leqslant k\leqslant 2k_0).\end{cases}$$

We can prove[3,5] that the two spectral branches corresponding to the values of coupling parameter $\nu_1=\rho g_0$ and $\nu_2=3\rho g_0$ satisfy the condition $E_k\to 0$, $k\to 0$ in the absence of a gap in the energy of excitation. The first branch corresponds to excitations in the Bogoliubov theory, while the second is similar to that described in Ref. 6.

Let us analyze the equations $\delta S_{\mathrm{ef}}(\rho,\nu)=0$ in order to find the values of $\rho$ and $\beta$ compatible with $\nu_{1,2}$. It should be noted above all that the low-temperature approximation as

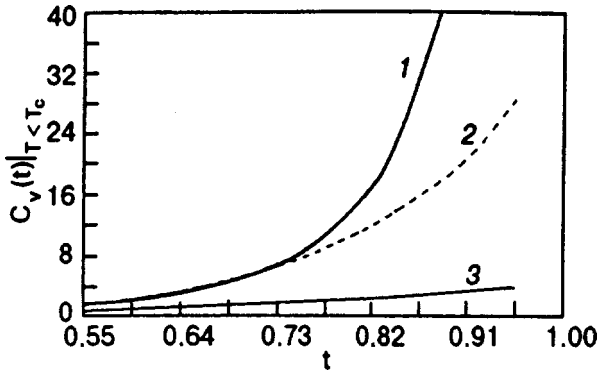


FIG. 1. Heat capacity of a Bose gas as a function of $t$ at $T<T_c$: theoretical (curve *1*) and experimental results obtained in Ref. 7 (curve *2*).

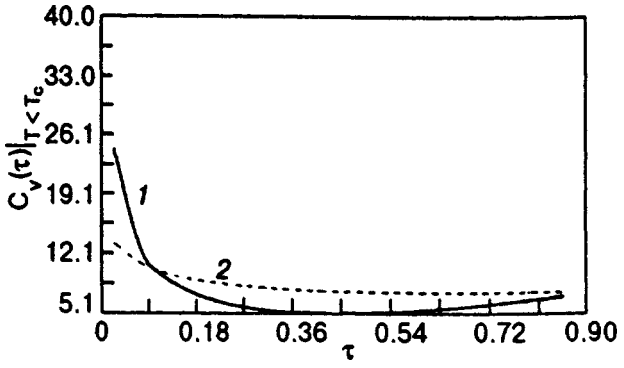


FIG. 2. Heat capacity of a Bose gas as a function of $\tau$ at $T>T_c$: theoretical (curve *1*) and experimental results obtained in Ref. 7 (curve *2*).

applied for the description of Bose condensation can be expressed by the inequality $\beta E_k>4$. The condition $r\geqslant 0$ confines the temperature to the value of $T_c$ in the case of $\nu_1$, but is immaterial in the case of $\nu_2$ so that Eqs. (2) assume the form

$$R=\rho_1+r_1, \quad 2g_0r_1=\rho_1G(\rho_1)(\nu=\nu_1),$$

$$T<T_c\equiv\frac{Rg_0}{4k_B}\simeq 3 \text{ K}, \tag{3}$$

$$R=\rho_2+r_2, \quad 2g_0r_2=\rho_2[2g_0+G(\rho_2)](\nu=\nu_2), \quad T<\infty. \tag{4}$$

The zeroth approximation for $G$ in Eqs. (3) and (4) in the form of ''nontrivial'' and ''trivial'' values of density of an ideal Bose gas, i.e.,

$$G(\rho_{1,2})\to G_0(\rho_{1,2}^0), \quad \rho_1^0=R[1-(T/T_c)^{3/2}], \quad \rho_2^0\equiv 0$$

leads to ''nontrivial'' and ''trivial'' solutions of these equations:

$$\rho_1=\frac{R}{1+x_1}, \quad r_1=\frac{Rx_1}{1+x_1},$$

$$x_1=\frac{G_0(\rho_1^0)}{2g_0}=\frac{r_1}{\rho_1}, \quad T<T_c,$$

$$\rho_2=\frac{r_2}{1+x_2}<r_2=\frac{R(1+x_2)}{2+x_2},$$

$$x_2=\frac{G_0(\rho_2^0)}{2g_0}, \quad \frac{r_2}{\rho_2}=x_2+1.$$

We can prove[5] that the free energies corresponding to these solutions are connected through the inequality $F_1<F_2$, and hence the solutions are valid for temperatures lower and higher than the superconducting transition temperature, so that the heat capacity is defined by the formulas

$$C_v=-VT\frac{\partial^2 F}{\partial T^2}, \quad F=\begin{cases}F_1, & T<T_c,\\ F_2, & T>T_c.\end{cases}$$

In the case of a ''nontrivial'' solution, we can consider two temperature regions.

(1) At low temperatures ($T\ll T_c, \rho\simeq R$), the contribution $E_{k1}\simeq kk_c/\mu$ of phonon excitations to $C_v$ gives

$$C_v\simeq\frac{k_BV(k_BT)^3}{\varepsilon_c^{3/2}}J_1,$$

$$\varepsilon_c=\frac{k_c^2}{\mu}=g_0\rho_1^0=g_0R[1-(T/T_c)^{3/2}]\simeq g_0R,$$

$$J_1=\kappa J_10, \quad \kappa=\mu^{3/2}\frac{c}{2}, \quad J_1^0\simeq\int_4^{\beta_cE_{k_01}}y^3dy.$$

(2) At temperatures close to $T_c(T<T_c, \rho\ll R)$, the temperature dependence $\varepsilon_c=g_0\rho_1^0$ leads to the formulas

$$C_v(t)=\frac{VTJ_2}{\xi_c^{3/2}}\frac{\partial^2(k_BT)^4}{\partial T^2}=3k_BV(k_BT_c)^{3/2}J_2\zeta(t),$$

$$t=\frac{T}{T_c}, \quad \zeta(t)=\frac{4t^3}{(1-t^{3/2})^{3/2}}, \quad J_2=2\kappa J_2^0,$$

$$J_2^0=\int_{y_0}^{\infty}y^2e^{-y/2}dy,$$

the parameter $y_0>4$ separating temperature regions above and below the superconducting transition temperature.

For ''trivial'' solution ($T>T_c, \rho\ll R$), we use the power expansion of the function $F_2(x)$ for $x=\gamma\sqrt{k_BT}\ll 1$:

$$C_v(\tau)=8k_BV(k_BT_c)^3R^{-1}J_3^0\xi(\tau),$$

$$\xi(\tau)=\frac{1}{4}\tau^{-1/2}-\frac{3}{4}\tau^{1/2}+\tau,$$

$$F_2(x)\simeq\frac{g_0R^2}{8}[4+a_1(k_BT)^{1/2}-a_2(k_BT)+a_3(k_BT)^{3/2}+a_4(k_BT)^2],$$

$$a_1=\gamma, \quad a_2=2\gamma^2, \quad a_3=2\gamma^3, \quad a_4=-0.5\gamma^4,$$

$$\gamma=g_0\dot{\kappa}J_3^0, \quad J_3^0=\int_4^{y_0}\frac{dy}{\sqrt{y}}.$$

The parameter $y_0$ can be found from the condition of coincidence of the scale of values $C_v(t)$ for $T<T_c$ and $C_v(\tau)$ for $T>T_c$ in the units $\text{J(mole}\cdot\text{K)}^{-1}$. For this purpose, the following estimates of integrals are used:

$$J_3^0 = 2(\sqrt{y_0} - 2), \quad J_2^0 \sim 2y_0^2 \exp(-y_0/2).$$

For example, the experimentally observed relation between the scales of $C_v(t)$ and $C_v(\tau)$ holds for superfluid $^4$He when the following transformation is used:

$$\frac{J_3^0}{J_2^0} = \frac{\sqrt{y_0} - 2}{y_0^2 \exp(-y_0/2)} \to \frac{1}{20}, \quad \xi(\tau) \to 20\xi(\tau).$$

This leads to the value of the parameter $y_0 = 4.4$ and to the equation for the function $\tau(T)$:

$$\frac{\tau}{\tau_0} = \frac{T - T_c}{T_0 - T_c}, \tag{5}$$

where $\tau_0 \to 0$ for $T_0 \to T_c$.

The initial value of temperature $T_0$ (for $\tau_0 = 0.03$) in Eq. (5) is assumed to be equal to 2.2 K for the superconducting transition temperature $T_c = 2.18$ K, while the final temperature value is $T = 2.9$ K ($\tau = 0.86$). The results of calculations are presented in Figs. 1 and 2 for $C_v|_{T<T_c}$ and $C_v|_{T>T_c}$, respectively. The values of heat capacity in J(mole·K)$^{-1}$ are laid along the ordinate axes. Solid curves corresponds to calculations based on the above formulas. Dashed and dotted curves in Fig. 1 correspond to experimental results obtained by Lounasmaa[7] and calculated by the formula $C_v \sim T^3$ for the phonon heat capacity. The dashed curve in Fig. 2 corresponds to experimental results obtained by Lounasmaa.[7] It can be seen from the figures that a reasonable coincidence of theoretical and experimental[7] results is observed for temperatures 0 K$<T<$1.6 K and 2.2 K$<T<$2.9 K.


[1] N. N. Bogoliubov, Izv. Akad. Nauk SSSR, Ser. Fiz. **11**, 77 (1947).
[2] V. S. Yarunin, Teor. Mat. Fiz. **96**, 37 (1993).
[3] V. S. Yarunin and L. A. Siurakshina, Physica A **215**, 261 (1995).
[4] V. S. Yarunin Physica A **232**, 436 (1996).
[5] V. S. Yarunin Teor. Mat. Fiz. **109**, 295 (1996).
[6] V. I. Yukalov, Mod. Phys. Lett. **5**, 725 (1991).
[7] O. V. Lounasmaa, Cryogenics **1**, 212 (1961).


Translated by R. S. Wadhwa

# Electronic properties of $C_{60}$ crystals: why we need crystals grown in a microgravity?

V. V. Kveder, R. K. Nikolaev, E. A. Steinman, and Yu. A. Ossipyan

*Institute of Solid State Physics, Russian Academy of Sciences, 142432, Chernogolovka, Moscow distr., Russia*[*]

Fiz. Nizk. Temp. **24**, 180 (February 1998)

[S1063-777X(98)02002-7]

The crystalline fullerene $C_{60}$ is a novel semiconductor that is very interesting for basic science and for possible applications. It corresponds to intermediate case between ''classical'' semiconductors (like Si or GaAs) and ''classical'' molecular crystals. Therefore, some interesting effects related to insulator–metal transitions and electron correlation can possibly be discovered in $C_{60}$ crystals. In spite of numerous investigations, the electronic properties of $C_{60}$ crystals are still far from being clearly understood. It is even not clear to what extent it is possible to consider the solid $C_{60}$ a one-electron band-like semiconductor. The main reason for that is the very high defect concentration in the crystals available now.

In the present report we discuss some experimental data concerning the electronic properties of $C_{60}$ crystals and the existing problems in their interpretation. We also discuss the reasons why the crystals grown in normal gravitation have many defects and why there is a good chance of producing much more perfect crystals in a microgravity conditions.

[*]E-mail: kveder@issp.ac.ru

This article was published in English in the original journal.

  

# Ultra-high vacuum investigations of atomic layers at low temperatures

V. A. Grazhulis

*Institute of Solid State Physics, Academy of Sciences of Russia, Chernogolovka, Moscow distr. 142432, Russia**

Fiz. Nizk. Temp. **24**, 181 (February 1998)

[S1063-777X(98)02102-1]

Low-temperature (10–300 K) investigations of Ag atomic overlayers on Ge (111), Si (111), and InSb (110) surfaces by means of different surface science techniques are briefly reviewed. It is shown that Ag monolayers can show very different behavior on different substrates. In the case of InSb (110) a new type of Ag can be formed.

Recent achievements in the development of ultra-high vacuum techniques are also briefly discussed.

*E-mail: grazhul@issp.ac.ru

This article was published in English in the original journal.

  

# Autowaves of component concentration under directed crystallization

A. P. Gus'kov

*Institute of Solid State Physics Academy of Sciences of Russia, Moscow District, Chernogolovka, 142432, Russia**

Fiz. Nizk. Temp. **24**, 182–185 (February 1998)

The occurrence of autowaves at the interface as a result of a first-order phase transition had been examined. The linear analysis of a system of the equations for a liquid which contains two components shows that a phase transition at the interface can give rise to autowaves. A spectrum of these autowaves depends on parameters of the system. For a special case of the system parameters an analysis is made of the dependence of the spectrum of autowaves from a temperature gradient the interface. We show that as a result of a interface instability in the bulk solid phase there are various periodic structures of distribution of the component concentration. Surfaces of equal concentration for the spectra of the autowaves are built. A qualitative and quantitative comparison of the numerical calculations with experimental data is made. © *1998 American Institute of Physics.* [S1063-777X(98)02202-6]

## INTRODUCTION

We have shown,[1–3] that a first-order phase transition can give rise to various types of autowaves of a component concentration at the interface. We obtained a dependence of the change in the spectrum of the autowaves on the temperature gradient at the interface.

The autowaves of the component concentration form a nonuniform distribution of the component in the solid phase as a result of the crystallization. Modes of the autowaves define a structure of the component distribution. Spatial period of the autowaves defines characteristic size of this structure. In this study we analyze of the distribution of the component concentration in the bulk solid phase and consider the types of autowaves, which were obtained in Ref. 3.

## FORMULATION OF THE PROBLEM

Let $T(y,z,\tau)$ be the temperature normalized to the phase transition temperature $T_{e0}$ and to the initial component concentration $C_0$; $C(y,z,\tau)$ is the component concentration normalized to the initial concentration; $y$, $z$, $\tau$ are the dimensionless coordinates and the time: $y=\alpha y_r$, $z=\alpha z_r$, $\tau=\alpha^2\chi_0\tau_r$; $D$ is the dimensionless factor of diffusion in a melt, $D=D_r/\chi_0$; $\chi=\chi_r/\chi_0$ is the factor of thermal diffusivity; $\varepsilon$ is the heat of phase transition normalized to the specific heat capacity and the temperature of phase transition; $y_r$, $z_r$, $\tau_r$, $D_r$, $\chi_r$ and $\varepsilon_r$ are dimensional quantities, $\chi_0=10^{-5}$ m$^2$/s, and $\alpha=10^2$ m$^{-1}$. Let the conditions of melt cooling be such that the flat front of crystallization in a stationary regime is moving at a constant velocity $V_s$.

We take into account the heat conduction in the solid and liquid phases and diffusion of the component in the liquid phase. To reduce the calculations in the equations, we do not write the coordinate $x$. The values relating to the solid phase are designated by a prime. In the coordinates $y$, $z$, $\tau$, which are rigidly connected with the moving front, the original system of equations has the form

$$\frac{\partial T'}{\partial\tau}=\chi'\Delta T'+V\frac{\partial T'}{\partial z};\quad z_0\leqslant z\leqslant 0;$$

$$\frac{\partial T}{\partial\tau}=\chi\Delta T+V\frac{\partial T}{\partial z};\quad 0\leqslant z<\infty;$$

$$\frac{\partial C}{\partial\tau}=D\Delta C+V\frac{\partial C}{\partial z};\quad 0\leqslant z<\infty;$$

$$\chi'\left.\frac{\partial T'}{\partial z}\right|_{z=-0}-\chi\left.\frac{\partial T}{\partial z}\right|_{z=+0}=\varepsilon V;$$

$$\chi\left.\frac{\partial T}{\partial z}\right|_{z=-0}=I;\quad T(0)=T'(0);\quad T(\infty)=T_{00};$$

$$D\left.\frac{\partial C}{\partial z}\right|_{z=0}=V(1-k)C(0);\quad C(\infty)=1;$$

$$V=V(T(y,0,\tau),\quad C(y,0,\tau)).$$

Here

$$k=\frac{C_\infty}{C_s(0)},$$

where $C_s(0)$ is the component concentration at the interface in the stationary regime.

To study the stability of the stationary solutions against small perturbations of the temperature and concentration, we seek the solutions as

$$T'=T'_s(z)+T'_m(z)\exp(\omega\tau+Ky);$$

$$T=T_s(z)+T_m(z)\exp(\omega\tau+Ky);$$

$$C=C_s(z)+C_m(z)\exp(\omega\tau+Ky);\quad \omega=\omega_1+i\omega_2;$$

$$K=K_1+iK_2,\quad T'_m(z)\ll T'_s(z);\quad T_m(z)\ll T_s(z);$$

$$C_m(z)\ll C_s(z),$$

where $T'_s(z)$, $T_s(z)$, and $C_s(z)$ are the solutions of the stationary problem. We linearize the boundary value problem to small $T'_m(z)$, $T_m(z)$, $C_m(z)$ quantities and find the solutions of the stationary problem and for small perturbations of the problem. The homogeneous boundary value problem for small perturbations gives the dispersion relation.

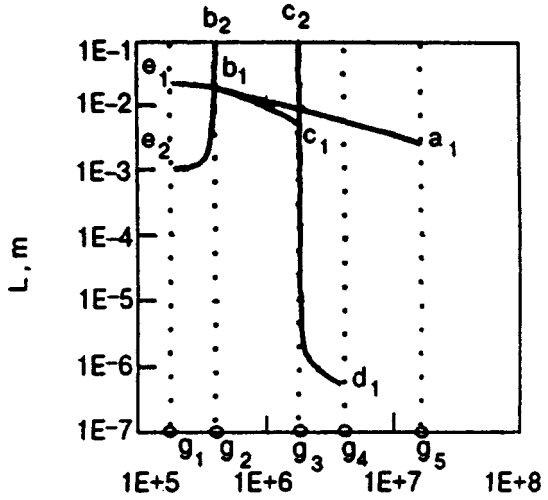


FIG. 1. Dependence of the spatial distortions $L_d$ and spatial period of temporary pulsations $L_p$ on the temperature gradient grad $T_s(0)$.

This dispersion relation contains all the parameters that are contained in the boundary value problem. These parameters depend on the composition of the material and on the external conditions of crystallization. They are reduced to six dimensionless parameters:

$$\mu_1=\frac{\chi}{D};\quad \mu_2=\frac{\chi}{\chi'};\quad P_1=\frac{\gamma}{V_s};\quad P_2=\frac{2\varepsilon\theta}{V_s};$$

$$\Phi_0=\frac{I_0}{\varepsilon V_s}=\frac{\chi}{\varepsilon V_s}\ \text{grad}\ T_s(0).$$

The solution of this task resulted in work in Ref. 3. To find the spectrum of the autowaves we used the maximum-growth-rate hypothesis.

## DISTRIBUTION OF THE COMPONENT CONCENTRATION IN THE SOLID PHASE

Let us consider the results from the physical point of view. According to the examined theory, the formation of the structure of the component distribution begins in the liquid in front of the interface. The liquid phase has a homogeneous distribution of the component at a sufficiently large distance from the interface. The component concentration becomes inhomogeneous near the interface as a result of nonlinear processes at the interface. It depends on both time and spatial coordinates. The inhomogeneity of the component concentration increases with decreasing distance to the interface. As a result, the component concentration is a flat periodic structure at the interface. Upon moving the interface, this structure is fixed into the solid phase. Thus, the volumetric periodic structure of the distribution components are formed in the solid phase.

Let $k=2$, $\mu_1=500$, $\mu_2=1.5$, $P_1=-206$, and $P_2=-4600$. In this case the dispersion relation can be presented as the dependence in Fig. 1. Here grad $T_s(0)$ is the temperature gradient at the interface; $L$ is a spatial period of the temporary oscillations and of the spatial distortions of the distribution of the component concentration in the solid phase, which are obtained from the expressions

$$L_p=\frac{8\pi D}{\alpha V_s\Omega},\quad L_d=\frac{4\pi D}{\alpha V_s\sqrt{Y}};\quad \Omega=\frac{4D\omega_i}{V_s^2};$$

$$Y=\frac{4D^2K_2^2}{V_s^2}.$$

Here $L_p$ is the spatial period of the temporary oscillations, and $L_d$ is the period of the spatial distortions. In the range $0<\text{grad}\ T_s(0)<g_1$ and $g_5<\text{grad}\ T_s(0)<\infty$ the system is steady. In the ranges $g_1<\text{grad}\ T_s(0)<g_2$ and $g_3<\text{grad}\ T_s(0)<g_4$ the system is unstable and the autowaves at the interface have one mode of the temporary oscillations and one mode of the spatial distortions. At $g_2<\text{grad}\ T_s(0)<g_3$ the autowaves have two spatial modes. At $g_4<\text{grad}\ T_s(0)<g_5$ the autowaves have one spatial mode.

Let us consider the distribution of the component concentration in the solid phase for each of these modes of the autowaves. In a common case for a regime with one mode of the temporary oscillations and two modes of the spatial distortions, it is possible to write the dependence of the component concentration on $x$, $y$, and $\tau$ at the interface as

$$c(x,y,\tau)=c_s+[A_1\ \cos(K_{21}x)\cos(K_{21}y)+A_2\ \cos(K_{22}x)\cos(K_{22}y)]\sin(\omega_2\tau). \quad (1)$$

Let us define the coordinate $z$ in the laboratory system of coordinates as

$$z=V_s\tau-\frac{1}{\omega_2}[A_1\ \cos(K_{21}x)\cos(K_{21}y)+A_2\ \cos(K_{22}x)\cos(K_{22}y)]\cos(\omega_2\tau), \quad (2)$$

where $A_1$ and $A_2$ are the constant factors, and $K_{21}$, and $K_{22}$ are the wave numbers of the first and second modes.

Let us consider a surface for a constant value of the component concentration in the solid phase at the ranges $g_1<\text{grad}\ T_s(0)<g_2$ and $g_3<\text{grad}\ T_s(0)<g_4$. To find the surface $c(x,y,\tau)=\text{const}=Q$ from Eqs. (1) and (2), we find $\tau$ in Eq. (1) and substitute it in Eq. (2). As a result, we obtain the dependence $z(x,y,\tau)$, which is at the required surface $c(x,y,\tau)=\text{const}=Q$ in coordinates $(x,y,z)$. To obtain the surface $c=\text{const}$ for autowaves with one temporary mode and one spatial mode, let us assume $A_2=0$. For example at $Q=0.9$, $c_s=1$, $V_s=1$, $A_1=0.2$, $A_2=0$, $\omega_2=1$, $K_{21}=1$. The surfaces of the component concentration for these values of the parameters are shown in Fig. 2. They correspond to a grainy component distribution. The grains can be elongate or flattened, depending on the ratio between the initial parameters. For example, if $K_2\ll\omega_2$, in the experiment, there will be a striated component distribution in the solid phase. This case corresponds to the range $g_3<\text{grad}\ T_s(0)<g_4$.

In the ranges $g_4<\text{grad}\ T_s(0)<g_5$ and $g_2<\text{grad}\ T_s(0)<g_3$ Eq. (1) has the form

$$c(x,y)=c_s+A_1\ \cos(K_{21}x)\cos(K_{21}y)+A_2\ \cos(K_{22}x)\cos(K_{22}y), \quad (3)$$

i.e., in this case for any value of $z$ the distribution of the component concentration is the solution of Eq. (3).

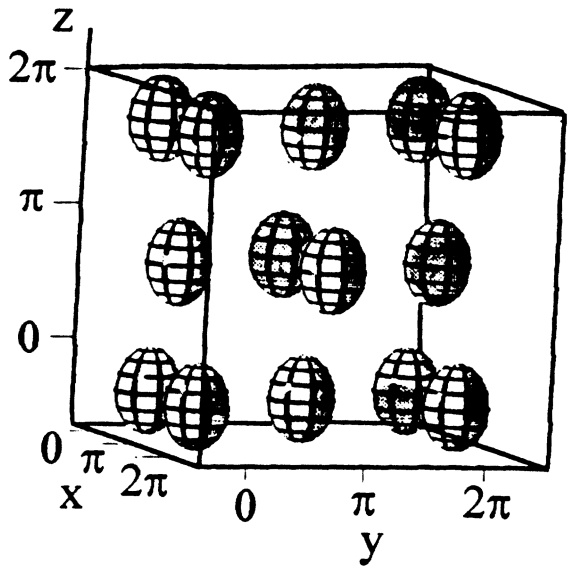


FIG. 2. Structure of distribution of the component concentration as grainy.

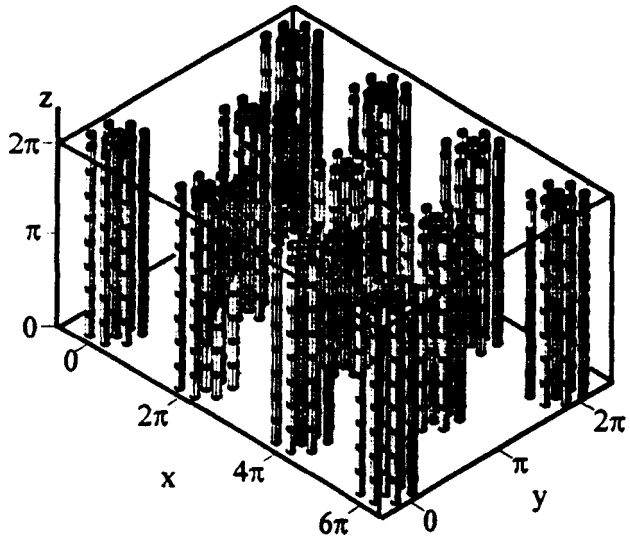


FIG. 4. Structure distribution of the component concentration as columns settle down by the groups.

Let us assume that in the range $g_4 < \text{grad}\, T_s(0) < g_5$ the parameters have the values $Q=0.8$, $c_s=1$, $V_s=1$, $A_1=0.3$, $A_2=0$; and $K_{21}=1$. The surfaces $c=\text{const}$ for this case are shown in Fig. 3. They represent columns which are parallel to the $z$ axis.

In the range $g_2 < \text{grad}\, T_s(0) < g_3$ we use the values $Q=0.7$, $c_S=1$, $V_s=1$, $A_1=0.1$, $A_2=0.3$, $K_{21}=1$, and $K_{22}=6$. The surfaces $c=\text{const}$ for this case are shown in Fig. 4. They also represent the columns parallel to the $z$ axis. In contrast to the previous case, however, these columns are arranged by the groups located periodically at a certain distance between these groups.

## COMPARISON WITH EXPERIMENT

We did not apply this model to calculations of the phase transitions of systems with a low temperature. We want to demonstrate that in the problems where the phase transitions together with the diffusion are examined, there can be complex periodic structures. We used the maximum-growth-rate hypothesis to investigate this problem. It is not a strict mathematical method of investigating the stability problems. However, in this case it gives not only qualitatively correct results, but also quantitative agreement of the numerical calculations with experiments. We used this theory to investigate crystallization of materials at usual temperatures and obtained complete qualitative agreement with the experimental data. All the structures found above coincide with the structures of the impurity distribution of real crystal materials. The grains similar to a sphere are a grainy structure, which is formed under the crystallization of large ingots and microcrystal materials. In the same materials the elongated grains may be formed. Such a structure is called as columnar crystals. The formation of the striated impurity distribution is

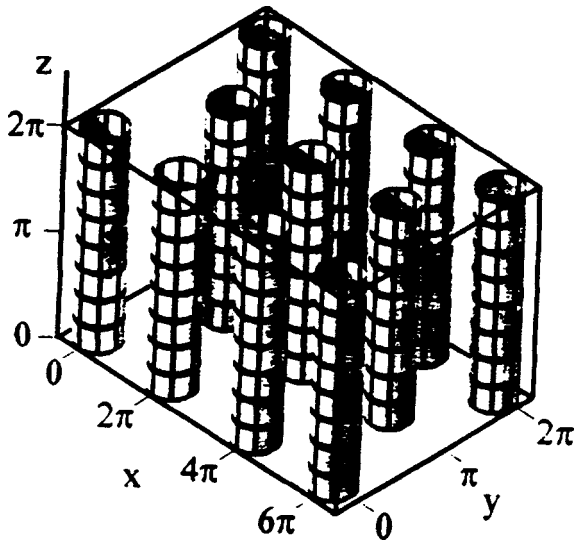


FIG. 3. Column structure distribution of the component concentration.

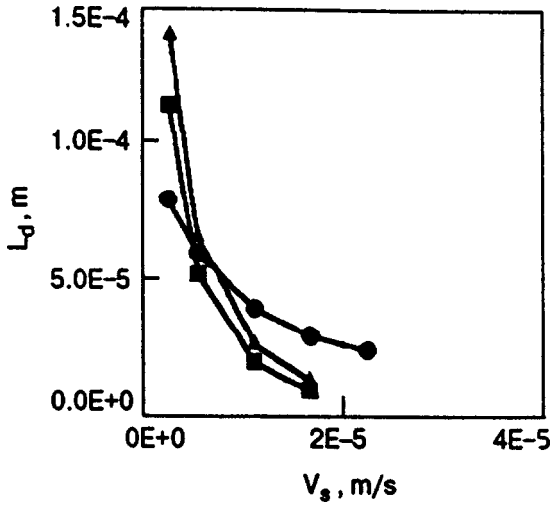


FIG. 5. Dependence of the distance between the columns of eutectic composites on the velocity of a moving interface. (●)—experimental data; (▲)—numerical calculations at $c_\infty < c_{\text{eut}}$; (■)—numerical calculations at $c_\infty c_{\text{eut}}$.

known as crystal growth. The impurity distribution as columns (Figs. 3 and 4) is formed as a result of crystallization of eutectic composites.

Recently we have applied this theory to a real experiment. The experiments performed in our laboratory of M. Starostin gave the dependence of distance between columns of eutectic composites on the velocity of a moving interface.[4] We have calculated this dependence using the model given here. The results of calculations are in good agreement with the experimental dependences. Figure 5 shows experimental and theoretical dependences.[5]

This work was supported by the Russian Fund for Fundamental Research, Grant No. 97-02-16845.

*E-mail: gusskov@issp.ac.ru

[1] A. P. Gus'kov, in *Instabilities in Multiphase Flows*, G. Gouesbet and Berlemont (Eds.), Pergamon, New York (1993), p. 25.
[2] A. P. Gus'kov, in *Hydromechanics and Heat and Mass Transfer in Microgravity*, Gordon and Breach Science Publishers, Amsterdam (1992).
[3] A. P. Gus'kov, Doklady of the Russian Academy of Sciences (in Russia) **349**, 561 (1996).
[4] V. A. Borodin, M. Yu. Starostin, and T. N. Yalovets, J. Cryst. Growth **104**, 143 (1990).
[5] A. Gus'kov and M. Starostin, J. Mater. Sci. (to be published).

This article was published in English in the original journal. It was edited by S. J. Amoretty.

# Large microlensing: history and perspectives

A. V. Byalko

*L. D. Landau Institute for Theoretical Physics, 117940, Kosygin St., 2 Moscow, Russia**
Fiz. Nizk. Temp. **24**, 186 (February 1998)

[S1063-777X(98)02302-0]

The recent observational confirmation[1,2] of microlensing (i.e., gravitational focusing of light from a distant star by a small invisible body) becomes a scientific event of rather unusual appearance: this phenomena was theoretically predicted by Einstein 60 years ago,[3] its observational probabilities were analyzed by me[4] and later by Paczynski.[5] Being finally observed the phenomena reveals difficulties in its becoming a valuable observational instrument.[6] Actually the instrumental capacity of microlensing and the information about lens bodies prove to be limited: observations of a single event cannot say definitely what are the mass and transverse velocity of the lensing body, and how far away it is located—only the product of the mass and distance becomes an actual outcome of each microlensing observation. I will report the results of a statistical approach to brightness changes of distant objects resulting in multiple microlensing. The theoretical time-correlation function will be compared with that for quasars observations.[7] Finally another observational procedure will be discussed briefly: the brightness curve of a pulsar in the radio waverange can reveal a diffraction pattern which could give information on both mass and distance to the lensing object.

*E-mail: byalko@landau.ac.ru

[1] C. Alcock *et al.*, Nature (London) **365**, 621 (1993).
[2] E. Aubourg *et al.*, Nature (London) **365**, 623 (1993).
[3] A. Einstein, Science **84**, 506 (1936).
[4] A. V. Byalko, Astron. Zh. **46**, 998 (1969) (in Russian), the English translation is published in *30 Years of the Landay Institute. Selected papers*, I.M. Khalatnikov and V. P. Mineev (Eds.), World Scientific (1996).
[5] B. Paczynski, Astrophys. J. **304**, 1 (1984).
[6] A. V. Byalko, *Microlensing: Statistical Approach, Astronomical and Astrophysical Trans.* **10**, 177 (1995); *Priroda* **24** (1994) (in Russian).
[7] M. R. S. Hawkins, Nature (London) **366**, 242 (1993).

This article was published in English in the original journal.

  

# The NASA/JPL program in microgravity fundamental physics

U. E. Israelsson

*Jet Propulsion Laboratory, California Institute of Technology, Mailstop 79-5, 4800 Oak Grove Drive, Pasadena, CA 91109, USA*[*]

M. C. Lee

*National Aeronautics and Space Administration, Microgravity Research Division, Code UG, Washington, DC 20546-0001, USA*[**]

Fiz. Nizk. Temp. **24**, 187–190 (February 1998)

The National Aeronautics and Space Administration (NASA) has been supporting research in microgravity low temperature physics for about 20 years. In the last 10 years, the program has seen significant growth in the number of funded investigations and in the breadth of the research activities being pursued. Currently, flight experiments are being performed exclusively on the Space Shuttle. For the future, a cryogenic Space Station facility is being developed by the Jet Propulsion Laboratory and industrial partners to support the microgravity needs of the international scientific community. The facility will be attached to the Japanese Experiments Module's Exposed Facility and will operate with a 6 month helium cryogen lifetime. Flights of the facility are planned at 2 year intervals starting in 2003 with each flight accommodating multiple scientific experiments. Capabilities, conceptual designs and development plans for the facility are discussed along with a summary of potential near term flight candidate experiments.  [S1063-777X(98)02402-5]

## INTRODUCTION

There are three different organizations within NASA that support scientific research. Code Y supports research in Earth science, Code S support research in planetary exploration and astronomy, and Code U supports research in life and microgravity science and applications. The Microgravity Research Division is part of Code U and sponsors research in the areas of biotechnology, combustion science, fluid physics, fundamental physics, and material science. The fundamental physics program is managed for NASA by the Jet Propulsion Laboratory (JPL) and aims at studying far-reaching physics questions that are obscured by gravity on the Earth. To accomplish the program goals, NASA funds a large number of ground investigators from which to select the best future flight experiments. Funds are also being expended on development of advanced technology to support the needs of future flight experiments.

In the early eighties the fundamental physics program consisted of a small community of investigators supported by NASA's Physics And Chemistry Experiments Program (PACE). This community expanded in the late eighties and early nineties to involve many major universities. Currently, NASA is funding 30 investigators (6 for potential flight) in the fundamental physics area. 26 of the investigations are in the low temperature and condensed matter physics area, 4 investigations are in the laser cooling and atomic physics area, and 2 investigations are in the relativity and gravitational physics area. Historically, the program has focused on research in the condensed matter physics area, primarily on critical point studies, although significant growth has occurred recently in the other research areas.

## SHUTTLE PROGRAM HISTORY

In 1985 the Superfluid Helium Experiment,[1] developed by the Jet Propulsion Laboratory, demonstrated the containment and control of liquid helium aboard the space shuttle and the feasibility of supporting a science instrument insert within a liquid helium dewar. Containment, using the fountain pressure, was accomplished by pumping with space vacuum on the helium through a porous plug. The porous plug and vent plumbing must be precisely adapted to the expected operating conditions for containment to occur.

In 1992 the Lambda-Point Experiment (LPE),[2] developed by Stanford University, JPL and Ball Aerospace, added nanokelvin high resolution thermometry to this capability which allowed a precise test of the Nobel Prize winning Renormalization Group (RG) theory of critical phenomena[3] to be performed. The LPE demonstrated that the superfluid transition in $^4$He is sharp to within about one nanokelvin, or about two orders of magnitude closer to the critical point than is accessible in a ground experiment. The heat capacity exponent measured by LPE ($\alpha = -0.0128 \pm 0.0004$) agrees with RG predictions,[4] but is about fifteen times more accurate than the best theoretical calculations. By making use of ground-based measurements of the correlation length exponent, $\upsilon$,[5] LPE was able to demonstrate to a high precision the validity of the hyperscaling relation $d\upsilon = 2 - \alpha$,[6] where $d = 3$ represents the dimensionality of the system. This scaling relation is one of the cornerstones of the theory giving confidence that the theory of critical phenomena is in effect an exact description of continuous phase transitions. Further, by making use of thermal transient data in the normal phase LPE was able to extend ground observations of thermal conductivity closer in to the transition. The data are consistent with ground data[7] further from the transition and with calculations based on dynamic renormalization group theory

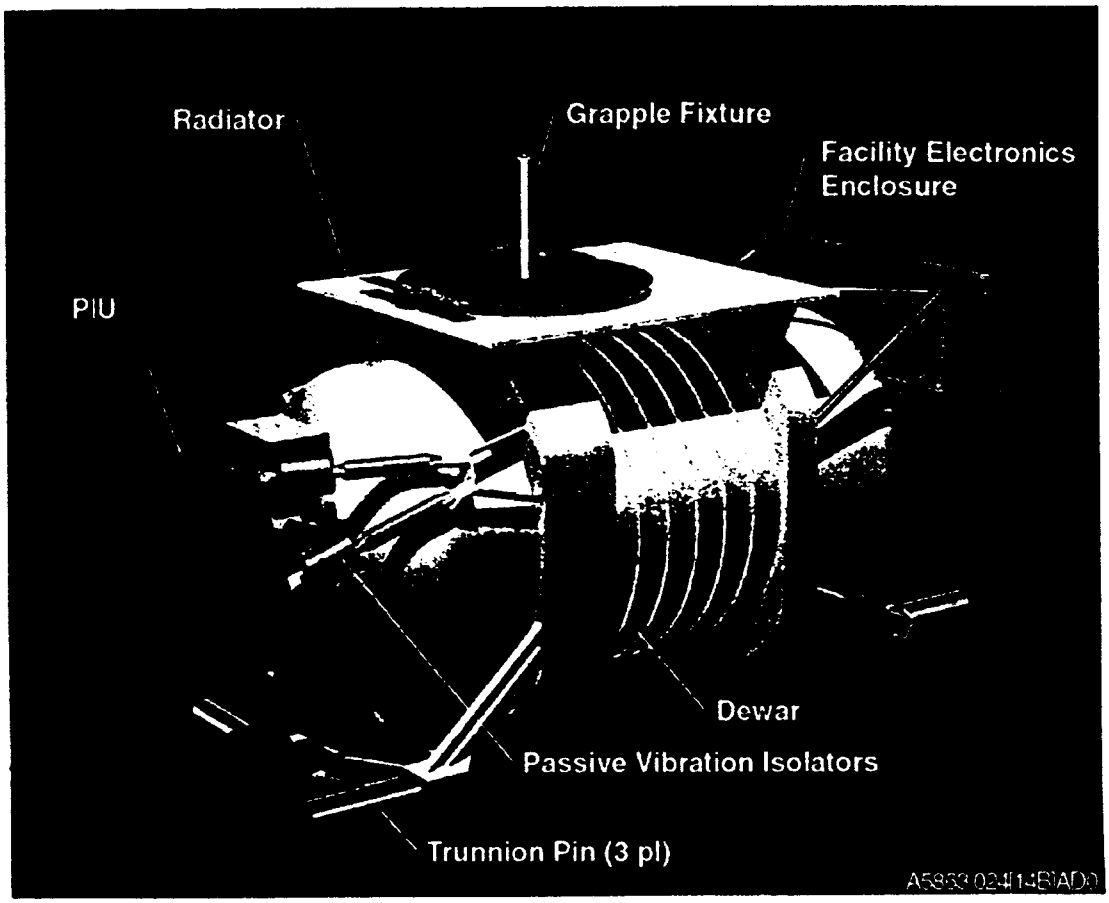


FIG. 1. An artist's rendering of the planned Space Station facility for performing fundamental physics experiments. The Payload Interface Unit (PIU) serves as the mechanical interface to the Space Station. The PIU is attached to the facility through passive vibration isolators. The trunnion pins are used to secure the facility in the Shuttle cargo-bay. Transfer from the Space Shuttle to the Space Station is accomplished with the grapple fixture and robotic arms.

techniques.[8] Perhaps equally significant, LPE demonstrated that advanced technology, high resolution experiments can be made to survive the shock associated with launch and can operate flawlessly in the hostile space environment. Subsequent flight projects, including the plans for experimentation aboard the space station relies heavily on the pioneering work developed for the LPE flight.

In 1997, the Confined Helium Experiment (CHeX) will use the unique properties of liquid helium to perform a high resolution test of the theory of finite size effects.[9] CHeX will investigate the shape of the heat capacity curve very near the lambda transition of a sample confined in one of the dimensions to about 50 microns thickness. Confinement is accomplished by stacking nearly 400 4 cm diameter, 50 micron thick Silicon wafers on top of each other with a 50 micron gap space between.

The last of the Shuttle based experiments, Critical Dynamics in Microgravity (DYNAMX) is tentatively scheduled to fly in 2001. DYNAMX will study the rich, largely unexplored, properties of superfluid helium driven away from equilibrium by introduction of a heat current.[10] Thermal conductivity data in the non-linear region will be collected as well as heat capacity data just below the superfluid transition. Heat currents below about 100 $nW/cm^2$ will be used predominantly.

While necessary and productive, shuttle based experiments are short term, lasting no longer than ten days; expensive; and require up to 7 years for development. It is clear that future experiments will require longer duration experiment times than possible on the shuttle. Therefore, the National Research Council's Space Studies Board and other advisory groups have recommended that NASA develop a cryogenic capability on the Space Station[11] for use by the fundamental physics community.

## SPACE STATION FACILITY DESCRIPTION

The facility will be implemented by a science, industry and JPL partnership of joint participation through all phases of definition, development and test. JPL will be responsible for development of the instruments and management of the overall activity. The industry partner, Ball Aerospace and Technology Corporation (BATC) was selected through a competitive technical selection process. BATC will be responsible for development of the facility flight hardware and the ground data system for controlling the experiments.

A conceptual design for the facility that meets all the imposed requirements has already been developed. An artist's rendering of the facility is shown in Fig. 1. The design provides 6 months of cryogenic lifetime operating as an attached payload to the Japanese Experiment Module's Exposed Facility. The facility carries about two hundred and

sixty liters of helium and accommodates two instrument inserts, one from either end of the cylindrical facility. Each instrument must fit within a volume defined by a cylinder with a diameter of 20 cm and a length of 50 cm. Other assumed constraints for each instrument is a mass limitation of 50 kg, a wire and plumbing count similar to LPE, and a power dissipation at helium temperatures of 10 mW. In addition to the necessary readouts for the helium dewar, the flight electronics will also accommodate all cards necessary to operate the two instruments. The instrument portion of the electronics provides germanium thermometry readouts and heater control circuits, 8 SQUID controllers, 4 precision heater drivers, and also ten extra slots for electronics cards beyond the capability of the LPE instrument. Passive vibration isolation of the facility is to be provided directly from the Space Station structure. The resonant frequency of the isolator is about 3 Hz, providing a factor of about 10 attenuation at a frequency of 10 Hz. To provide experimenters with a direct correlation of important environmental influences to their science data, the facility provides the output from a 3-axis accelerometer and a charged particle monitor. The 3-axis accelerometer is sampled at 250 Hz and will provide accurate $g$-jitter information up to 100 Hz at levels down to a few $\mu$g. The charged particle monitor will have a sampling rate of up to 100 Hz and a sensitivity of about 2 MeV for protons and heavier particles.

After the two instruments have been constructed and tested, they will be integrated with the Space Station facility at JPL. Following integration and cool down to helium temperatures, the facility and instruments will go through system testing and environmental sensitivity testing at JPL. The integrated system will then be shipped cold to Kennedy Space Center for integration with the Shuttle orbiter. The dewar is last serviced on the launch pad prior to payload bay door closure launch activities. Transfer from the Orbiter to the Space Station is accomplished by crew internal vehicle activity using Orbiter and Space Station remote manipulator systems.

Turn-on and check-out will be performed at the Payload Operations Control Center (POCC) for the Space Station and routine operations will be conducted from individual remote POCCs located at investigator facilities using telemetry and command services from the Space Station POCC. The facility will operate continuously for 6 months or until the cryogen is expended and then wait passively for the next opportunity to transport back to Earth.

During the 6 months operation of one flight, a second pair of instruments will be developed, integrated and tested with another flight dewar in preparation for the next flight. Upon return to Earth, the facility will proceed through a brief checkout and the instruments and dewar from the first flight will be removed and replaced with the flight ready instruments and dewar for the next flight. This exchange of instruments and dewars will allow re-flight as often as every 20–24 months.

## SCIENCE SELECTIONS

Science participants will be determined through the NASA Research Announcement (NRA) peer review process. Two potential flight experiments for the Space Station facility have recently been selected.[14] The Microgravity Scaling Theory Experiment (MISTE)[15] will perform very precise measurements of thermodynamic properties near the liquid/vapor critical point of 3He. In particular, MISTE will measure the heat capacity exponent ($\alpha$), the isothermal compressibility exponent ($\gamma$), and the exponent characterizing the relation between pressure and density along the critical isotherm ($\delta$). These exponents will be used for a self-consistent test of scaling law predictions.

The Superfluid Universality Experiment (SUE)[16] will measure the superfluid density exponent along the lambda line of helium in microgravity. These measurements along with measurements of the heat capacity exponent along the lambda line in the 0.01 g facility at JPL[17] will be used to check the universality prediction of the theory of critical phenomena.

Two additional flight definition investigations are targeted to be selected from a NRA solicitation currently under review. Subsequent NRAs will be issued at two year intervals for future experiment selections.

## CONCLUSIONS

The microgravity fundamental physics program of NASA's Microgravity Research Division have experienced significant growth in the early 1990's. To meet the need for extended experimentation time in microgravity over the coming decades, NASA and JPL have teamed with Industry to develop a Microgravity Physics Facility for use on the International Space Station. The facility attaches outside the Space Station to the Japanese Experiment Module's Exposed Facility and provides a 6 month lifetime for operation of two instruments per flight. The international scientific community is invited to collaborate with U.S. researchers in developing science experiments for this facility via the NASA Research Announcement process. The first flight of the facility is targeted for the year 2003.

This work was carried out by the Jet Propulsion Laboratory, California Institute of Technology under a contract with NASA. We acknowledge stimulating discussions with Rich Reinker and Reuben Ruiz.

*E-mail: ulf@squid.jpl.nasa.gov
**E-mail: mark.lee@hq.nasa.gov

[1] P. V. Mason *et al.*, *Proc. Intern. Cryogenic Engineering Conf.* West Berlin, April 22–25, 1986, Butterworth Guilford, Surrey (1986).
[2] J. A. Lipa, D. R. Swanson, J. A. Nissen, T. C. P. Chui, and U. E. Israelsson, Phys. Rev. Lett. **76**, 944 (1996).
[3] K. G. Wilson, Phys. Rev. B **4**, 3174 (1971).
[4] J. C. Le Guillou and J. Zinn-Justin, Phys. Rev. B **21**, 3976 (1980); D. Z. Albert, Phys. Rev. B **25**, 4810 (1982).
[5] L. S. Goldner, N. Mulders, and G. Ahlers, J. Low Temp. Phys. **93**, 131 (1992); D. R. Swanson, T. C. P. Chui, and J. A. Lipa, Phys. Rev. B **46**, 9043 (1992).
[6] B. D. Josephson, Proc. Phys. Soc. **92**, 269 (1967).
[7] W. Y. Tam and G. Ahlers, Phys. Rev. B **32**, 5932 (1985).
[8] V. Dohm, Phys. Rev. B **44**, 2697 (1991); Z. Phys. B **61**, 193 (1985).
[9] D. R. Swanson, J. A. Nissen, X. Qin, P. R. Williamson, J. A. Lipa, T. C. P. Chui, U. E. Israelsson, and F. M. Gasparini, J. Spacecr. Rockets **33**, 154 (1996).

[10] Principal investigator, R. V. Duncan, University of New Mexico.
[11] *Microgravity Research Opportunities for the 1990s*, unpubl. report by the National Research Council's Space Studies Board.
[12] J. A. Lipa, D. R. Swanson, and T. C. P. Chui, Cryogenics **34**, 341 (1994).
[13] X. Qin, J. A. Nissen, D. Swanson, P. R. Williamson, D. A. Stricker, J. A. Lipa, T. C. P. Chui, and U. E. Israelsson, Czech. J. Phys. **46**, 2857 (1996).
[14] NRA-94-OLMSA-05, November 29, 1994.
[15] Principal investigator, M. Barmatz, JPL.
[16] Principal investigator, J. Lipa, Stanford University.
[17] M. Larson, F. Liu, and U. E. Israelsson, Czech. J. Phys. **46**, 179 (1996).

This article was published in English in the original journal.

# The boundary resistance between superfluid $^4$He near $T_\lambda$ and a solid surface

Haiying Fu, Hanan Baddar, Kerry Kuehn, and Guenter Ahlers

*Department of Physics and Center for Nonlinear Science, University of California, Santa Barbara, California 93106, USA**

Fiz. Nizk. Temp. **24**, 101–103 (February 1998)

We report high-resolution measurements of the singular contribution $R_b$ to the thermal boundary resistance between a solid surface and superfluid helium near the superfluid-transition temperature $T_\lambda$. The results confirm the observation by Murphy and Meyer that a gap between the cell end and the sidewall leads to an apparent finite-current contribution to $R_b$. In the absence of such a gap, overall agreement of $R_b$ with theoretical predictions is very good. Remaining small differences require further investigations. Without a sidewall gap and within our resolution we found no finite-current effects over the range $3.9\ \mu\mathrm{W/cm^2} < Q < 221\ \mu\mathrm{W/cm^2}$. © *1998 American Institute of Physics.* [S1063-777X(98)00102-9]

67.40.Pm

In bulk superfluid $^4$He heat transport occurs through counterflow of the normalfluid ($j_n$) and superfluid ($j_s$) currents and does not produce a temperature gradient.[1] However, a heat current $Q$ orthogonal to a solid wall will produce a boundary layer in the fluid adjacent to the wall with a temperature difference $\Delta T_b$ across it.[1] Physically there are two reasons for this. The superfluid must be converted to normal fluid near the wall in order to maintain the counterflow in the interior. In addition, the order parameter, and thus $j_s$ and $j_n$, are suppressed near the wall. The boundary layer has a thickness which is proportional to the correlation length $\xi$. Within it, some of the heat must be carried by diffusive processes. Consequently, a thermal gradient is developed near the wall. However, the thermal resistance $R_b = \Delta T_b / Q$ is unobservably small deep in the superfluid phase where the boundary-layer thickness is of atomic dimensions. Only very close to the superfluid transition temperature $T_\lambda$, where $t \equiv 1 - T/T_\lambda$ becomes small and $\xi = = \xi_0 t^{-\nu}$ diverges, does $R_b$ become measurable in high-precision experiments. Thus this phenomenon was discovered experimentally only about a decade ago by Duncan *et al.*[2,3] Roughly speaking one can assume that the temperature gradient in the boundary layer decays exponentially from $-Q/\lambda$ at the wall (where there is no counterflow at all) to zero deep in the superfluid (where all the heat is carried by counterflow) with a characteristic length equal to $\xi$. Here $\lambda \simeq \lambda_0 t^{-x_\lambda}$ with $x_\lambda \simeq 0.42$ is the diffusive thermal conductivity of the fluid.[4] This leads to the crude estimate $R_b = \xi/\lambda - t^{-x_b}$ where $x_b = \nu - x_\lambda \simeq 0.25$. A renormalization-group-theoretical calculation of $R_b$ carried out by Frank and Dohm[5,6] agrees with this qualitative expectation and is expected to give the behavior of $R_b(t)$ quantitatively. We report new measurements of $R_b$ which agree well with the predicted overall size of $R_b$ in the range $3 \times 10^{-7} \leqslant t \leqslant 10^{-3}$. However, at the smallest values of $t$ the data fall somewhat below the theory and additional work is in progress to explore the precise dependence upon $t$ of $R_b$.

The apparatus was a modified version of one described previously.[3,7] A schematic diagram of the sample cell is shown in Fig. 1. It had cylindrical copper top and bottom ends and a stainless-steel sidewall. The top plate was silver soldered into the sidewall, thus leaving no gap between the copper anvil and the stainless steel. The bottom endplate has an anvil which fits snugly into the sidewall, and was sealed with an indium gasket to the bottom flange of the sidewall. The gap between the anvil and the sidewall was approximately 0.01 mm. The top surface of the cell was finely machined copper. The bottom surface was atomically smooth gold[8] epoxied onto a polished copper surface. The cell was filled from the bottom. It had an inside diameter of 1.27 cm and an interior height of 0.50 cm. The sample was high-purity $^4$He containing less than 1 ppb $^3$He. Both the top and bottom of the cell had copper platforms on which high-resolution copper-ammonium-bromide (CAB) susceptibility thermometers[9] with a resolution of 3 nK were mounted. Two sideplanes similar in construction to the mid-plane of[2,3] were attached to the cell wall. Each sideplane carried a CAB thermometer, thus permitting a determination of the helium temperature adjacent to it.

The top temperature was held constant and the desired current $Q$ was passed through the cell. The resulting $\Delta T$ between the cell top or bottom and the nearest sideplane gave the total thermal resistance $R$. The result includes the boundary-layer resistance $R_b$ of interest as well as the Kapitza resistance $R_K$ due to the temperature jump at the wall and the resistance $R_{\mathrm{Cu}}$ of the copper between the cell surface and the relevant thermometer. At large currents there also was a contribution $R_{\mathrm{He}}$ due to mutual friction in the

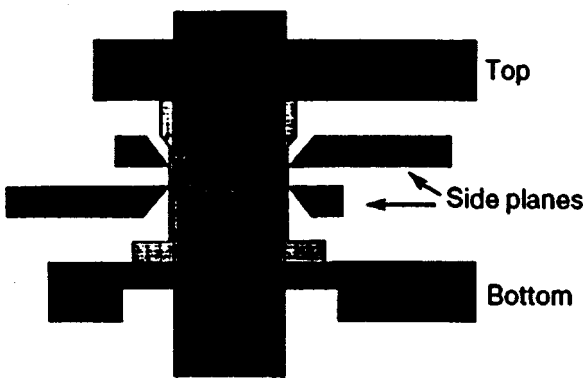


FIG. 1. Schematic diagram of the cell.

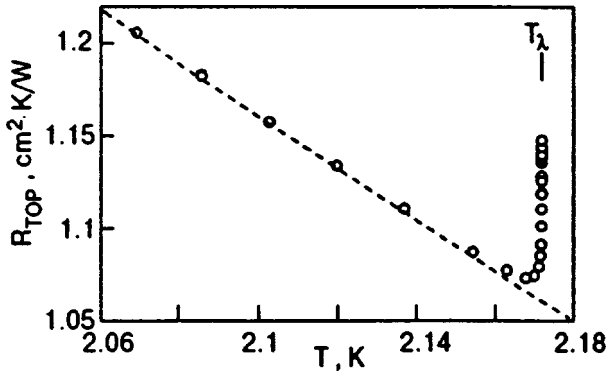


FIG. 2. The total resistance $R$ of the top cell surface as a function of temperature on linear scales.

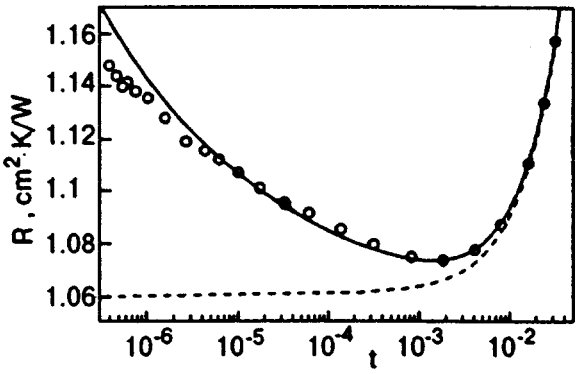


FIG. 4. The total resistance $R$ of the top cell surface on an expanded linear scale as a function of $t$ on a logarithmic scale.

helium layer between the sideplane and the cell end. The contribution from $R_{\rm He}$ was measured separately using the two sideplanes and subtracted when necessary. It was less than our resolution for $Q<7\ \mu$W/cm$^2$.

Figure 2 gives results for the cell top on linear scales over a wide range of $T$. It shows the regular contribution from $R_K$ and $R_{\rm Cu}$, as well as the singular contribution very near $T_\lambda$ from $R_b$. Some of the same data are plotted in Fig. 3 (open symbols) on a linear scale as a function of $t$ on a logarithmic scale. Also shown there are the results for the bottom end (solid symbols). The data for the bottom surface show a strong anomalous current-dependent contribution. This phenomenon was observed previously in a number of investigations.[10] Recently it was suggested by Murphy and Meyer[11] that such an effect can arise from a small gap between the copper anvil and the cell wall (see Fig. 1). From the data in Fig. 3 one sees that the top surface of our cell, which does not have such a gap, does not have an anomalous current-dependent contribution. Thus our data confirm the observation of Murphy and Meyer,[11] and provide conclusive evidence that the previously observed current dependence is unrelated to the theoretically calculated[5,6,12] boundary resistance.

In order to extract $R_b$ from the measurements of $R$ for the top surface, we fit the data well below $T_\lambda$ to a polynomial in $T_\lambda - T$. This fit is the background contribution from $R_K$ and $R_{\rm Cu}$, and is shown as the dashed lines in Figs. 2 and 3. The contribution $R_b$ to $R$ which is of interest to us is the small difference between the open circles and the dashed lines in the figures. In order to see the contribution from $R_b$ more clearly, we show the data for the cell top on an expanded linear vertical scale as a function of $t$ on a logarithmic scale in Fig. 4. The fit to the background is still shown as a dashed line. The *solid* line is the sum of the background and of the theoretical prediction[5,6] for $R_b$. We see that the overall agreement between the data and the theory is very good. This is in contrast to recent measurements by Murphy aud Meyer[11] which yield an $R_b$ about a factor of two larger than the theory. At small $t$, our results fall slightly below the predicted curve. This small difference requires further investigation.

We searched with high resolution for any remaining current dependence of $R_b$ at the top surface of our cell, and found none. The results are shown in Fig. 5 as a function of the average reduced temperature $t_b$ (relative to $T_\lambda[Q=0]$) of the boundary layer. In principle, a small current dependence would be expected theoretically, but only very close to $T_\lambda$.[12,13] Apparently our measurements were not sufficiently close to reveal this effect within our resolution.

This work was supported by NASA Grant NAG-3-1847.

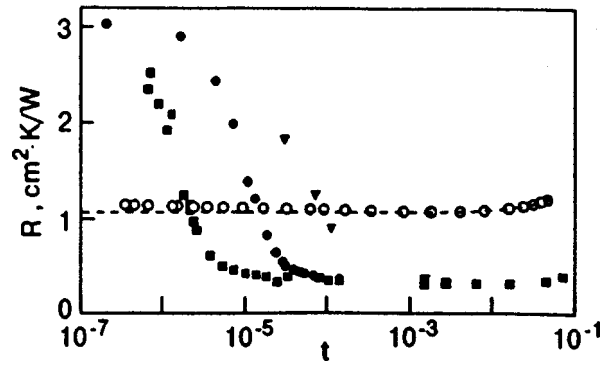


FIG. 3. The total resistance $R$ of the top (open circles) and bottom (solid symbols) cell surface. The solid squares, circles, and triangles are for $Q=1$, 10, and 100 $\mu$W/cm$^2$, respectively. The open circles are for the same three currents; for clarity we show them all by the same symbol.

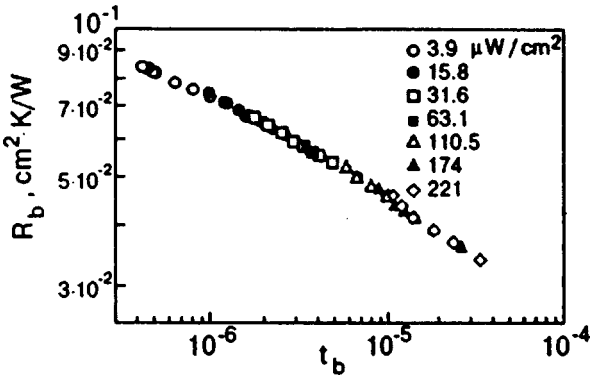


FIG. 5. The contribution $R_b$ from the fluid boundary layer to the resistance $R$ as a function of the mean reduced temperature $t_b$ of the boundary layer on logarithmic scales for different heat currents.

*E-mail: guenter@tweedledee.ucsb.edu

[1] L. D. Landau, J. Phys. (Moscow) **5**, 71 (1941) [English translation: *Collected Papers of L. D. Landau*, D. ter Haar (Ed.) Gordon and Breach, New York (1965), p. 301].
[2] R. V. Duncan, G. Ahlers, and V. Steinberg, Bull. Am. Phys. Soc. **31**, 281 (1986); Phys. Rev. Lett. **58**, 377 (1987).
[3] R. V. Duncan and G. Ahlers, Phys. Rev. B **43**, 7707 (1991).
[4] G. Ahlers, Phys. Rev. Lett. **21**, 1159 (1968).
[5] D. Frank and V. Dohm, Phys. Rev. Lett. **62**, 1864 (1989).
[6] D. Frank and V. Dohm, Z. Phys. B **84**, 443 (1991).
[7] A. Singsaas and G. Ahlers, Phys. Rev. B **29**, 4951 (1984).
[8] N. G. Woodard and G. P. Lafyatis, J. Vac. Sci. Technol. A **14**, 332 (1996).
[9] H. Baddar, H. Fu, M. Larson, N. Mulders, and G. Ahlers, Czech. J. Phys. **46**, 2859 (1996).
[10] For a summary of early work, see Ref. 3. For a more recent summary, see Ref. 11.
[11] D. Murphy and H. Meyer, J. Low Temp. Phys. **105**, 185 (1996).
[12] R. Haussmann, *Ph.D. Thesis, Technische Hochschule Aachen*, Aachen, Germany (1991) (unpublished).
[13] V. Dohm and R. Haussmann, Physica B **197**, 215 (1994); and references therein.
[14] G. Ahlers, Phys. Rev. **171**, 275 (1968); J. Low Temp. Phys. **84**, 173 (1991).

This article was published in English in the original journal.

# Lambda point thermodynamics of confined liquid helium: negative surface specific heat

R. A. Ferrell

*Center for Theoretical Physics of the Department of Physics, University of Maryland, College Park, Maryland 20742, USA**

J. K. Bhattacharjee

*Indian Association for the Cultivation of Science, Jadavpur, Calcutta 700 032, India*

Fiz. Nizk. Temp. **24**, 104–108 (February 1998)

We present some theoretical considerations that are relevant to the forthcoming measurements in microgravity of the specific heat of confined liquid helium (the flight experiment ''CHEX''). Primary attention is devoted to the suppression near the boundaries, the ''negative surface specific heat.'' Above the lambda point, we compute this to lowest order in the $\varepsilon$-expansion: below the lambda point our discussion is more restricted.  [S1063-777X(98)00202-3]

The forthcoming measurements in microgravity of the specific heat of liquid $^4$He confined between parallel plates (the flight experiment ''CHEX'') present an important challenge to the general theory of the critical properties of a fluid near the critical point of a second order transition. In the case of liquid He, which is described by a complex order parameter, we have noted[1] that the cross-over at the lambda point from three-dimensional to two-dimensional behavior is beyond the scope of current theory. It is feasible, however, to develope a theoretical prediction of the temperature dependence in the crossover region by means of an interpolation[1] based on the ''negative surface specific heat'' outside the crossover region. In this paper we present a computation of this effect above the lambda point to lowest order in the $\varepsilon$-expansion. Because of space limitation, we provide only a quite incomplete discussion of the much more complicated theory below the lambda point.

It is generally accepted that the thermodynamics of liquid $^4$He are determined by the Ginzburg–Landau free energy functional

$$F=\frac{1}{2}\,|\nabla\Psi|^2+\frac{a}{2}\,|\Psi|^2+\frac{b}{4}\,|\Psi|^4, \tag{1}$$

provided that the effects of the fluctuations of the complex order parameter, $\Psi$, are properly included. In this short note our attention will be directed mainly to the critical specific heat in the normal state, that is, at temperatures $T$ greater than the lambda temperature $T_\lambda$. After a short review of the contributions of the order parameter fluctuations to the bulk specific heat, we will study how these contributions are reduced by the suppression of the fluctuations that results from the boundary condition at the walls of the confining vessel. This fractional reduction, relative to the bulk value, can be regarded as a ''negative surface specific heat,'' and can be expected to be of the form $A\xi S/V$, proportional to the product of the order parameter correlation length times the surface to volume ratio. The primary goal of the first part of this paper is to compute the numerical value of the proportionality coefficient $A$. Our method and approach differ somewhat from those of Schmolke *et al.*[2] and Huhn and Dohm.[3]

In the normal state, each component of the order parameter fluctuates about its mean value zero. To simplify the notation, we let $\Psi$ be a real field that denotes one of these components, and decompose it into the sum of plane waves:

$$\Psi=\frac{1}{\Omega}\sum_{\mathbf{p}}\,\Psi_{\mathbf{p}}\,\exp i\mathbf{p}\times\mathbf{x}, \tag{2}$$

where $\Omega$ is the volume of the hypercube in $D$-dimensional space. Restricting the free energy functional to this component alone, and neglecting the quartic term, we have for the volume integration

$$\int\,Fd^Dx=\frac{1}{2}\sum_{\mathbf{p}}\,(p^2+a)|\Psi_{\mathbf{p}}|^2. \tag{3}$$

Applying the equipartition theorem and using units in which the temperature times Boltzmann's constant is one, we obtain for the equilibrium thermal average

$$\langle|\Psi_{\mathbf{p}}|^2\rangle=\frac{1}{p^2+a}. \tag{4}$$

The bulk thermodynamic free energy is the negative of the logarithm of the partition function

$$Z=\sum_{\{\Psi\}}\,\exp\left(-\int\,Fd^Dx\right), \tag{5}$$

summed over all configurations of the fluctuating field $\Psi$. The entropy density is therefore

$$\frac{\partial\,\ln\,Z}{\partial T}=-\frac{a'}{2}\,\langle\Psi^2\rangle, \tag{6}$$

where the prime denotes the temperature derivative. In the following discussion, we will ignore the coefficient $a'/2$ and regard $-\langle\Psi^2\rangle$ as representing the entropy. Substitution from Eq. (2) and replacement of the summation by an integration yield

$$\langle\Psi^2\rangle=\frac{1}{\Omega}\sum_{\mathbf{p}}\,\langle|\Psi_{\mathbf{p}}|^2\rangle=\frac{1}{(2\pi)^D}\int\,\frac{d^Dp}{p^2+\kappa^2}. \tag{7}$$

Here we have introduced the inverese correlation length

$$\xi^{-1}=\kappa=\sqrt{a}. \tag{8}$$

In anticipation of our later treatment of the surface effect, it is useful to separate one of the Cartesian components of **p**, say $q$, from the remaining $D-1$ components, **k**. Substituting

$$p^2=q^2+k^2. \tag{9}$$

into Eq. (7) and carrying out the integration over $q$ yields

$$\frac{1}{2\pi}\int_{-\infty}^{\infty}\frac{dq}{q^2+k^2+\kappa^2}=\frac{1}{2}\,(k^2+\kappa^2)^{-1/2}. \tag{10}$$

Thus,

$$\langle\Psi^2\rangle=\frac{1}{2(2\pi)^{D-1}}\int\frac{d^{D-1}k}{(k^2+\kappa^2)^{1/2}}. \tag{11}$$

Because differentiation with respect to $\kappa^2$ is, except for the factor $a'$, the same as differentiation with respect to $T$, the bulk specific heat is proportional to

$$-\frac{\partial\langle\Psi^2\rangle}{\partial\kappa^2}=\frac{1}{4(2\pi)^{D-1}}\int_0^{q_D}\frac{d^{D-1}k}{(k^2+\kappa^2)^{3/2}}. \tag{12}$$

The Wilson–Fisher $\varepsilon$-expansion theory calculates the specific heat as a Taylor's series in powers of $\varepsilon=4-D$. With enough terms in the truncated power series, a good account can be rendered of the thermodynamics in the actual three-dimensional system, i.e., $\varepsilon=1$. It is found, however, that smaller values of $\varepsilon$ can simulate the lambda-point properties of $^4$He, provided that $n$, the number of components of the order parameter, is taken as a continuous variable and permitted to increase above its natural value of 2 as $\varepsilon$ decreases below 1. Following this procedure and introducing the Debye cutoff $q_D$, we obtain a satisfactory representation of the bulk specific heat from the $\varepsilon\to 0$ $(D\to 4)$ limit of Eq. (12). (The neglect of the quartic term in Eq. (1) is justified in this limit because the coefficient, $b$, is proportional to $\varepsilon$.) Thus,

$$\begin{aligned}-\frac{\partial\langle\Psi^2\rangle}{\partial\kappa^2}&=\frac{1}{4(2\pi)^3}\int_0^{q_D}\frac{d^3k}{(k^2+\kappa^2)^{3/2}}\\&=\frac{1}{4(2\pi)^3}\,4\pi\int_0^{q_D}\frac{k^2dk}{(k^2+\kappa^2)^{3/2}}\\&=\frac{1}{8\pi^2}\left(\ln\frac{q_D}{\kappa}+\text{const}\right)=\frac{1}{16\pi^2}\left(\ln\frac{q_D^2}{\kappa^2}+\text{const}\right),\end{aligned} \tag{13}$$

This compares well with the experimentally measured specific heat. Because of the very small empirical value of the critical exponent, the logarithm into provides a good representation of the temperature dependence.

The above brief review of the bulk specific heat will now serve as a basis for our investigation of the effect of imposing the Dirichlet boundary condition at parallel planes separated by $L$ and normal to the direction of the momentum coordinate $q$. Thus, the fluctuation modes are no longer ''running waves'' but rather ''standing'' sine waves with quantized momenta

$$q_n=n\,\frac{\pi}{L}, \tag{14}$$

and spacing $\Delta q_n=\pi/L$. Instead of the integration over $q$ we now have the sum

$$\begin{aligned}\frac{1}{L}\sum_{n=1}^{\infty}\frac{1}{q_n^2+k^2+\kappa^2}&=\frac{1}{2L}\left(\sum_{n=1}^{\infty}\frac{1}{q_n^2+k^2+\kappa^2}\right.\\&\qquad\left.+\sum_{-\infty}^{n=-1}\frac{1}{q_n^2+k^2+\kappa^2}\right)\\&=\frac{1}{2L}\sum_{-\infty}^{\infty}\frac{1}{q_n^2+k^2+\kappa^2}-\frac{1}{2L}\,\frac{1}{k^2+\kappa^2}.\end{aligned} \tag{15}$$

To evaluate the first term in Eq. (15) it is convenient to introduce

$$Q=\frac{L}{\pi}\,(k^2+\kappa^2)^{/12}. \tag{16}$$

In terms of this variable the required sum is the following meromorphic function, which has a second order pole at $Q=0$ and first order poles at $i$ times the non-zero integers:

$$\begin{aligned}\frac{1}{2L}\sum_{n=-\infty}^{\infty}\frac{1}{q_n^2+(\pi^2/L^2)Q^2}&=\frac{L}{2\pi^2}\sum_{n=-\infty}^{\infty}\frac{1}{n^2+Q^2}\\&=\frac{L}{2\pi Q}\coth(\pi Q)\\&=\frac{\coth(\pi Q)}{2(k^2+\kappa^2)^{1/2}}.\end{aligned} \tag{17}$$

We need this expression for large values of $Q$, for which

$$\coth(\pi Q)\approx 1-2\exp(-2\pi Q). \tag{18}$$

The last term expresses the perturbing effect of the overlap of the two penetration regions that extend from the opposite sides into the interior of the fluid. With

$$\pi Q\geqslant Lk=\frac{L}{\xi}\gg 1, \tag{19}$$

we see that Eq. (17) is nothing other than Eq. (10), except for a very small error of the order of, or less than, $\exp(-2L/\xi)$. This error is evidently such as might be expected from the general ''rule of thumb'' [4] that any disturbance to the squared order parameter should heal at distances $l\gg\xi/2$ and die out as $\exp(-2l/\xi)$. According to Eq. (18): keeping $\xi$ below the upper bound

$$\xi_{u.b.}=\frac{1}{2}\,L \tag{20}$$

should hold the error to less that 4%.

With the neglect of the exponentially small error in Eq. (18), the final term in Eq. (15) represents the only remaining effect of the Dirichlet boundary conditions. The surface contribution to the entropy is, therefore,

$$-\langle\Psi^2\rangle_{\rm Dir}=\frac{1}{2L}\,\frac{1}{(2\pi)^{D-1}}\int\frac{d^{D-1}k}{k^2+\kappa^2}. \tag{21}$$

Setting $D-1$ again equal 3, we find for the surface specific heat

$$\begin{aligned}-\frac{\partial\langle\Psi^2\rangle_{\rm Dir}}{\partial\kappa^2}&=-\frac{1}{2L}\,\frac{1}{(2\pi)^3}\int\frac{d^3k}{(k^2+\kappa^2)^2}\\&=-\frac{1}{4\pi^2L}\int_0^\infty\frac{k^2dk}{(k^2+\kappa^2)^2}=-\frac{1}{4\pi^2L}\,\frac{\pi}{4\kappa}\\&=-\frac{1}{16\pi^2}\,\frac{\pi\xi}{L}.\end{aligned} \tag{22}$$

Gathering together Eqs. (13) and (21), we have for the effect of the Dirichlet boundary condition at the walls

$$\begin{aligned}-\frac{\partial[\langle\Psi^2\rangle+\langle\Psi^2\rangle_{\rm Dir}]}{\partial\kappa^2}&=\frac{1}{16\pi^2}\left[\ln\left(\frac{q_D^2}{\kappa^2}\right)+{\rm const}-\pi\,\frac{\xi}{L}\right]\\&=\frac{1}{16\pi^2}\left[\ln\left(\frac{q_D^2}{\kappa^2}\right)+{\rm const}-\frac{\pi}{2}\,\frac{S\xi}{V}\right].\end{aligned} \tag{23}$$

The final form of this equation is a generalization to an arbitrary shape of the fluid sample, and is valid provided that $\xi$ is small in comparison with the characteristic dimensions of the vessel. The coefficient of $S\xi/V$ that is predicted by the above simple theory is evidently

$$A_{\rm th}=\frac{\pi}{2}=1.57. \tag{24}$$

This theoretical result can he compared with some recent measurements by Mehta and Casparini[5] for confinement between plane walls of separation equal to $L=2110$ Å and $L=5040$ Å. We limit our attention to the thinner of these fluid layers, for which the surface effect is bigger and thus easier to read off from the display of the data in their Fig. 2. To limit the overlap error to less than 4%, Eq. (20) requires $\xi<\xi_{u.b.}=1055$ Å. With the correlation length given by

$$\xi(t)=\xi_0t^{-\nu}, \tag{25}$$

where $\xi_0=1.4$ Å and $\nu=0.672$, this implies $t>0.5\times10^{-4}$. In fact, from the lower curve of Mehta and Casparini (Fig. 2) we find that the size of the drop below the bulk specific heat fits very well the temperature dependence $t^{-\nu}$, with a deviation of 4% first showing up at $t=0{,}5\times10^{-4}$ and increasing rapidly at lower temperatures.

It remains only to deduce the coefficient $A$ from their data, for which one choice of temperature in the surface scaling range will suffice. At $t=10^{-4}$ the negative surface specific heat is evidently $\Delta C=-3.85$ J/mole·K. The bulk specific heat is fitted by

$$C_{\rm bulk}=B\left(\ln\frac{q_D^2}{\kappa^2}+{\rm const}\right) \tag{26}$$

with $B=4.01$ J/mole·K. Including the surface effect gives the total as

$$C_{\rm tot}=C_{\rm bulk}+\Delta C=B\left(\ln\frac{q_D^2}{\kappa^2}+{\rm const}+\frac{\Delta C}{B}\right), \tag{27}$$

of the same form as Eq. (23), which permits the identification

$$A_{\rm exp}\,\frac{\xi}{L/2}=-\frac{\Delta C}{B}=0.960. \tag{28}$$

According to Eq. (25), $\xi=682$ Å at $t=10^{-4}$, so

$$A_{\rm exp}=1.49, \tag{29}$$

5% below the theoretically predicted value in Eq. (24). This agreement is remarkably close, in view of the approximate nature of the calculation. A more complete theoretical treatment would produce $A_{\rm th}$ as a Taylor's series in powers of $\varepsilon$, of which Eq. (24) would be the truncated version, stopping at the first term.

An alternative experimental study of the negative surface specific heat, for $^4$He confined in 8-micron diameter cylindric pores, has been reported by Coleman and Lipa.[6] The lower half of Fig. 1 in[6] exhibits a log-log plot of their $T>T_\lambda$ data, which is fitted well by the $t^{-\nu}$ temperature dependence. But lacking a comparison with the bulk specific heat, as well as relevant information on the dimensional units, we are not able to deduce from their data an independent value for $A_{\rm exp}$.

For the sake of brevity we now limit our review of the computation of the negative surface specific heat for $T<T_\lambda$ to its most salient features, leaving the details and remaining features to be presented elsewhere. For $a<0$ the symmetry with respect to the order parameter is broken and it takes on the mean field value $\Psi_{MF}$ fixed by

$$\Psi_{MF}^2=-\frac{a}{b}. \tag{30}$$

With $\Psi=\Psi_{MF}+\varphi$, the terms in $F$ quadratic in the fluctuation $\varphi$ are

$$\frac{a}{2}\,\varphi^2+\frac{3b}{2}\,\Psi_{MF}^2\varphi^2=-a\varphi^2\equiv\frac{\kappa_-^2}{2}\,\varphi^2, \tag{31}$$

where the inverse correlation length is given by

$$\xi_-^{-2}=\kappa_-^2=2|a|. \tag{32}$$

Imposing the Dirichlet boundary condition at the plane $z=0$ gives the mean field order parameter the Ginzburg–Pitaevsky space dependence

$$\Psi_0(z)=\Psi_{MF}\tanh(z/2\xi). \tag{33}$$

The resulting surface loss in entropy is

$$\begin{aligned}\int_0^z dz[\Psi_0^2(z)-\Psi_{MF}^2]&=\Psi_{MF}^2\int_0^\infty dz\,\,{\rm sech}^2\,\frac{z}{2\xi_-}\\&=2\xi_-\Psi_{MF}^2=\frac{\xi_-}{b}\,2|a|=\frac{\kappa_-}{b},\end{aligned} \tag{34}$$

the temperature differentiation of which yields a surface correction to the temperature independent mean field bulk specific heat coming from the differentiation of $\Psi_{MF}^2$ itself. For

a more subtle effect of the $z$-dependence of $\Psi_0(z)$ we return to Eq. (31) to find that the coefficient of the quadratic term,

$$[a+3b\Psi_0^2(z)]\,\frac{\varphi^2}{2}=\frac{\kappa_-^2}{2}\left(1-\frac{3}{2}\,\mathrm{sech}^2\,\frac{z}{2\xi}\right)\varphi^2, \qquad (35)$$

dips down to negative values close to the boundary. This results in a localized fluctuating mode and discrete energy eigenvalue below the continuum, the consequences of which will be examined elsewhere.

This work has been supported by a Grant for Basic Research NAG 3-1867, from the National Aeronautics and Space Administration.

*E-mail: rferrell@muppetn.umd.edu

[1] R. A. Ferrell and J. K. Bhattacharjee, in *Proc. of the Joint Xth European and VIth Russian Symposium on Physical Sciences in Microgravity*, St. Petersburg, Russia, June 15–21, 1997, to be published.
[2] R. Schmolke, A. Wacker, V. Dohm, and D. Frank, Physica B **165–166**, 575 (1990).
[3] W. Huhn and V. Dohm, Phys. Rev. Lett. **61**, 1368 (1988).
[4] R. A. Ferrell, J. Phys. (Paris) **32**, 85 (1971).
[5] S. Mehta and F. M. Gasparini, in *Proc. of the 21st Intern. Conf. on Low Temperature Physics*, Prague, August 8–14, 1996, S. Danis, V. Gregor, and K. Zareta (Eds.), Part Sl. Czech. J. Phys. vol. **46**, Suppl. Sl, (1996), p. 173.
[6] M. Coleman and S. A. Lipa, in *Proc. of the 21st Intern. Conf. on Low Temperature Physics*, Prague, August 8–14, 1996, S. Danis, V. Gregor, and K. Zareta (Eds.), Part Sl. Czech. J. Phys. vol. **46**, Suppl. Sl (1996), p. 183.

This article was published in English in the original journal.

# Theory for normal state critical Kapitza resistance of $^4$He

R. A. Ferrell

*Center for Theoretical Physics of the Department of Physics and Astronomy, University of Maryland, College Park, Maryland 20742, USA**

J. K. Bhattacharjee

*Indian Association for the Cultivation of Science, Jadavpur, Calcutta 700 032, India*

S. I. Mukhin

*Moscow State Institute for Steel and Alloys, Theoretical Physics Dept., Leninskii prospect 4, 117936 Moscow, Russia***

Fiz. Nizk. Temp. **24**, 109–111 (February 1998)

We study a steady state, bearing a heat current, $Q_0$. In the normal state of liquid $^4$He with constraining geometry, near the lambda point, at temperatures $T$ greater than the lambda temperature, $T_\lambda$. Critical order parameter fluctuations near the boundary are incorporated in the expression for the non-local thermal resistivity. The Kapitza resistance is manifested by the additional temperature rise at the boundary, as compared with the bulk-extrapolated value. Sensitivity of the calculations to the application of the Dirichlet boundary condition is discussed. © *1998 American Institute of Physics.* [S1063-777X(98)00302-8]

In the region of the lambda point of $^4$He the critical Kapitza resistance is a strong function of temperature. This behavior is predicted by theory and has been measured experimentally. It is puzzling that the recent experimental data[1] and the theoretical results[2] for the additional boundary contribution to the thermal conductivity of $^4$He just above the λ-point show a significant discrepancy. Understanding the physical source of this discrepancy is important for the general theory of critical fluctuations at a second-order phase transition. In this paper we calculate the Kapitza resistance in a different way from that of Frank and Dohm[2] by modeling a boundary with the heat source imbedded in the liquid helium in the plane $z=0$. Such a source produces the outward flow

$$Q(z)=Q_0 \ \text{sign} \ z=\begin{cases} Q_0, & z>0, \\ -Q_0, & z<0. \end{cases} \tag{1}$$

The resulting temperature distribution would give the gradient

$$\frac{dT_\infty}{dz}\equiv T'_\infty(z)=-\rho(0,\kappa)Q(z), \tag{2}$$

in the absence of any boundary effect, with $\rho(0,\kappa)=\lambda^{-1}(0,\kappa)$ the thermal resistivity, i.e., the reciprocal of the thermal conductivity. Then, the Kapitza resistance is manifested by the difference:

$$\Theta(z)=T(z)-T_\infty(z). \tag{3}$$

The choice of zero in temperature is irrelevant and does not affect this difference. The wave number dependent non-local resistivity, $\rho(k,\kappa)$, determines the spatial derivative, $\Theta'(z)$, by the operator equation

$$\Theta'(z)=T'(z)-T'_\infty(z)=-[\tilde{\rho}-\rho(0,\kappa)]Q(z). \tag{4}$$

In the Fourier representation this becomes

$$ik\tilde{\Theta}(k)=-[\rho(k,\kappa)-\rho(0,\kappa)]\tilde{Q}(k). \tag{5}$$

Here we use the following notations:

$$\tilde{Q}(k)\equiv\int_{-\infty}^{\infty}dz\ \exp(-ikz)Q(z)=-\frac{2i}{k}\,Q_0,$$

$$\tilde{\Theta}(k)\equiv\int_{-\infty}^{\infty}dz\ \exp(-ikz)\Theta(z). \tag{6}$$

Combining Eqs. (5) and (6) we readily get

$$\tilde{\Theta}(k)=\frac{2}{k^2}\,[\rho(k,\kappa)-\rho(0,\kappa)]Q_0. \tag{7}$$

The Kapitza resistance is consequently

$$R_K=\frac{\Theta(0)}{Q_0}=\frac{2}{\pi}\int_0^\infty\frac{dk}{k^2}\,[\rho(k,\kappa)-\rho(0,\kappa)]. \tag{8}$$

Making use of the bulk thermal conductivity,

$$\lambda=\rho(0,\kappa)^{-1}\sim\kappa^{-x/\nu}, \tag{9}$$

we can approximate the non-local resistivity by

$$\rho(k,\kappa)=\lambda^{-1}[1+(k/a\kappa)^2]^{x/2\nu}, \tag{10}$$

with $a=O(1)$. The thermal conductivity critical exponent in the crossover region is $x$ and the critical exponent of the correlation length is $\nu$, $\xi=\kappa^{-1}$.

Thus,

$$R_K=\frac{a\xi}{\lambda}\,I, \tag{11}$$

where the definite integral is

$$I=\frac{2}{\pi}\int_0^\infty\frac{du}{u^2}\,[(1+u^2)^{x/2\nu}-1]. \tag{12}$$

This integral converges at both upper and lower limits due to $x/\nu<1$. Integration by parts yields

$$I=\frac{2}{\pi}\frac{x}{\nu}\int_0^\infty \frac{du}{(1+u^2)^{1-x/2\nu}}. \tag{13}$$

Noting that $1-x/2\nu>1/2$, and passing to the new variable ($u=\tan\chi$, $du=\sec^2\chi$), the integral reduces to the Euler beta-function, $\beta(m,n)$:

$$I=\frac{2}{\pi}\beta\left(\frac{1}{2},\frac{1}{2}-\eta\right);\quad \eta\equiv\frac{x}{2\nu}. \tag{14}$$

It is convenient to rewrite Eq. (11) in the form

$$R_K=\frac{l_{\rm eff}}{\lambda} \tag{15}$$

with the amplitude of the effective thickness of the critical boundary layer

$$l_{\rm eff}=A\xi \tag{16}$$

given by

$$A=aI. \tag{17}$$

From the slope of the log-log plot of Ahler's data[3] we obtain

$$x=0.46. \tag{18}$$

This crossover effective exponent is well accounted for by ''quasi-scaling'' theory,[5] in which the asymptotic dynamic scaling exponent of 0.40 is increased by the factor of $1+z_Q$, where $z_Q$ was found to equal 0.18. This brought the theoretically expected quasi-scaling exponent up to

$$x_Q=0.40\times 1.18=0.47, \tag{19}$$

in good accord with the experimental value of $x$. Substituting this value of $x$ into Eq. (14), with $\nu=0.672$, we obtain $\eta=0.343$, which yields $\beta(1/2,1/2-\eta)=7.66$ and $I=1.673$. From the ''rule of thumb'' [6] and the two-term $\varepsilon$ expansion[7] we have $a=2$, so that $A=2.35$.

In order to compare this result with the theory of Frank and Dohm[2] we have deduced their value for this coefficient by reading off the numerical values for $R_K$ from their Fig. 3 in Ref. 2. It suffices to consider the case $t=10^{-6}$, for which they evidently predicted the value $R_K=0.0268\ \mathrm{K\cdot cm^2/W}$. Multiplying by Ahlers' [3,4] thermal conductivity at the saturated vapor pressure and at this same temperature, namely, $\lambda=6.24\cdot 10^{-3}$ W/K·cm we find $l_{\rm eff}^{FD}=1.67\times 10^{-4}$ cm. Dividing by the correlation length

$$\xi=\xi_0 t^{-\nu}=1.40\times 10^{-8}\times 10^{6\nu}\ \text{cm}=1.49\times 10^{-4}\ \text{cm},$$

we obtain for the Frank–Dohm theory the coefficient $A_{FD}=1.12$.

In comparing data[1] with the Frank–Dohm theory,[2] Lipa and Li noted a significant discrepancy in magnitude. The size of the boundary effect that they observed was evidently approximately five times greater than that predicted by Frank and Dohm. Our treatment, presented above, predicts a stronger effect than that of Frank and Dohm by the factor of 2.1 (from A and $l_{\rm eff}^{FD}$). This factor can be expected to get bigger when we improve our idealized ''embedding'' theory by introducing the Dirichlet boundary condition at the heat source. The increase, however, is unlikely to be large enough to account fully for the observed magnitude of the effect.

The work has been supported by NASA Grant NAG3-1867.

*E-mail: rferrell@muppetn.umd.edu
**E-mail: sergeimoskow@glasnet.ru

[1] J. A. Lipa, Adv. Space Res. **13**, 61 (1993); J. A. Lipa and Q. Li, Czech. J. Phys. **46**, Suppl. S1 (1996).
[2] D. Frank and V. Dohm, Z. Phys. B **84**, 443 (1991).
[3] G. Ahlers, in *Proc. of the XII'th Int. Conf. on Low Temperature Physics*, Kyoto, 1970, E. Kanda (Ed.), Keigaku, Tokyo (1971), p. 21.
[4] G. Ahlers, in *Physics of Liquid and Solid Helium*, K. H. Benneman and J. B. Ketterson (Eds.), Wesley, New York (1976), vol. 1, Fig. 36.
[5] R. A. Ferrell and J. K. Bhattacharjee, Phys. Rev. B **28**, 121 (1983).
[6] R. A. Ferrell, J. Phys. (France) **32**, 85 (1971).
[7] R. A. Ferrell and J. K. Bhattacharjee, J. Low Temp. Phys. **36**, 166 (1979).

This article was published in English in the original journal.

# Dynamical behavior of He I–He II interface layer caused by forced heat flow

M. Murakami, K. Kamiya, and T. Sato

*Institute of Engineering Mechanics, University of Tsukuba, Tsukuba, Ibaraki 305 Japan*[*]
Fiz. Nizk. Temp. **24**, 112–115 (February 1998)

The appearance and dynamical behavior of a He I–He II phase interface is investigated experimentally. The experimental mode in which nearly saturated He I initially at a little bit higher temperature than the lambda temperature is cooled by sudden evaporative cooling is primarily employed in the present experiment among several possibilities. In this mode where an interface appears and propagates downward, some dynamical aspects of an interface layer can be preferably investigated. The phenomenon is investigated by the application of the schlieren visualization method, and by measuring the temperature variation by superconductive temperature sensors and the pressure variation as well as the evaporating vapor flow rate which can be converted into the cooling rate. © *1998 American Institute of Physics.* [S1063-777X(98)00402-2]

## INTRODUCTION

The λ transition of liquid helium was investigated by several researchers both theoretically[1,2] and experimentally,[3] in which a phase transition was supposed to be caused by heating. In the present study, the appearance and dynamical behavior of He I–He II interface generated by imposing forced heat flow as a means to create spatial inhomogeneity is experimentally investigated. A phase interface can emerge in such several modes as; i) cooling of nearly saturated He I initially at a little bit higher temperature than the lambda temperature by sudden evaporative cooling from a free surface, ii) cooling of subcooled He I by Joule–Thomson (J–T) heat exchanger during the process of phase conversion to create subcooled He II where a phase interface proceeds from below, and iii) heating of subcooled He II by a heater. The appearance of an interface was able to be visually observed in every mode. The experimental result conducted in the first mode is primarily described in the present report. Such dynamical aspects of the phenomena as the propagation speed of an interface and the dynamical stability are investigated by the application of Schlieren visualization method and by using a superconductive temperature sensor. It is visually observed that an interface appears and then propagates downward from a free surface in a cryostat if the cooling heat flux is larger than parasitic heat leak into the cryostat. The propagation speed is measured by a double probe superconductive sensor and the data is correlated with the cooling heat flux and the distance from the free surface. It is, however, suggested from the present ground experiment that the dynamical behavior, in particular the dynamical stability, as well as the appearance is affected by the such gravity effects as the natural convection and thermal stratification.

## EXPERIMENTAL APPARATUS AND PROCEDURE

A He I–He II phase interface was generated by a number of methods by imposing forced heat flow in this study, as mentioned in the introduction, such as; i) sudden evaporating cooling of He I, ii) cooling of subcooled He I by a J–T heat exchanger, and iii) heating of subcooled He II from a horizontal planar heater. In the first mode, of which experimental results are primarily discussed in this paper, nearly saturated He I at a little bit higher temperature than the lambda temperature is cooled by sudden evaporative cooling by evacuating vapor from a free surface with a vacuum pump. The overall view of the experimental setup for the first mode experiment is schematically given in Fig. 1. An electric valve controls quick opening of the evacuation line connected to a vacuum pump to start vapor evacuation for sudden cooling. The temperature of He I in the free surface region drops abruptly to pass the lambda point along the saturated vapor line, and then a phase interface appears and propagates downward from the free surface provided that the cooling heat flux is larger than parasitic heat leak into the cryostat. A schematic illustration of the propagation of an interface is given in Fig. 2. A well defined phase boundary layer can be observed by using the high sensitivity schlieren visualization method. The dark and white contrast in a schlieren image is in proportion to the spatial derivative of the refractive index, or approximately of the temperature. For the measurement of the propagation speed of an interface, we utilize a superconductive sensor made of gold-tin thin film vacuum deposited on the side wall of a fine quartz rod with a diameter of 40 $\mu$m. The schematic drawing of a sensor is shown in Fig. 3. The electric resistance of a sensing element drastically changes as a function of the temperature around a supernormal transition region. The sensor has a very high sensitivity and a high time resolution as small as several $\mu$s, and the active range with a very high temperature sensitivity can be adjusted so as to cover the lambda point region by carefully controlling the thickness ratio between gold and tin films. And the minute trimming of the sensitive range can be performed by changing the bias electric current through a sensing element. The speed of interface propagation is calculated from the time interval of two onset signals of the resistance variations of two aligned sensing elements, that is time-of-flight method. For this purpose, we utilized a double probe sensor of which two sensing elements are separated by about 5 mm in the direction of interface propagation. The cooling heat flux across a free surface is calculated in terms of the evaporating vapor flow rate measured with a gas flow meter and the latent heat of evaporation. Optical visualiza-

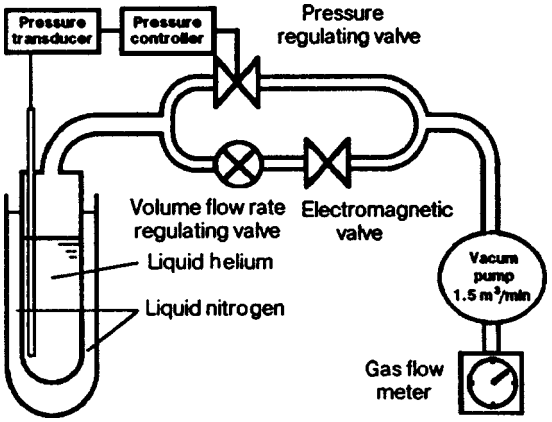


FIG. 1. Overall view of the experimental setup for the first experimental mode, evaporative cooling of He I.

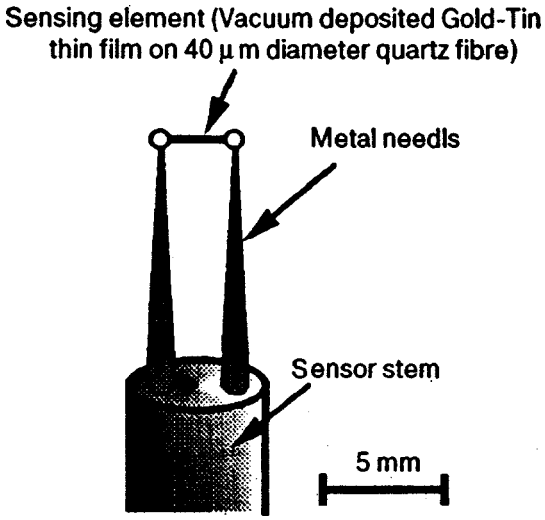


FIG. 3. Schematic drawing of a superconductive temperature sensor (single probe type).

tion to make the local density, or the temperature variation around an interface visible is applied to investigate the dynamical stability of it during propagation.

Each experimental run begins with the production of a thermal equilibrium state at a prescribed temperature, usually only slightly higher temperature than the lambda temperature, with the vapor pressure control valve system. Just before the start of evaporative cooling, the vapor control valve is closed for the following measurement of the vapor flow rate. Then the measurements of the flow meter, the vapor pressure sensor and the superconductive sensor are started in response to the start of evaporative cooling. Visual observation is also carried out through a pair of optical windows of the cryostat.

## RESULTS AND DISCUSSION

The data acquisition starts in response to the signal of quick valve opening. A typical example of the data is shown in Fig. 4, where the variation of the vapor pressure and the data from the superconductive sensor located at 10 cm below a free surface are plotted against the time. It is seen from the figure that the vapor pressure once drops upon the start of the evacuation and then further decreases very slowly during an experimental run for about 20 s. This result indicates that the temperature of a free surface once drops down to the lambda point to result in generating a phase interface and then continuously decreases a little below the lambda point through the period of evacuation. It should be noted that data from the superconductive sensor does not exactly indicate the temperature variation in particular in the region across an interface. The data should be rather considered to be subject to both effects of the heat transfer coefficient between the sensing element and surrounding medium (He I or He II) and of the temperature. The reason for this is that the sensor generates small amount of heat due to Joule heating, and thus the temperature of the element itself must be higher than that of surrounding medium when a sensor is immersed in He I because of poor heat transfer coefficient between the sensing element and He I. The element temperature rapidly drops down to the surrounding temperature in He II because of so called super thermal conduction in He II. Thus, the variation of the superconductive sensor output shown in Fig. 4 is much exaggerated as compared with that of the temperature in particular in the transition region. It is, however, fair to consider that the variation of the data except in the transition region is that of the temperature. It is seen that the temperature little drops before the arrival of an interface and it further drops quite slowly behind the interface in He II phase. The latter seems to indicate that He II behind an interface layer is in the

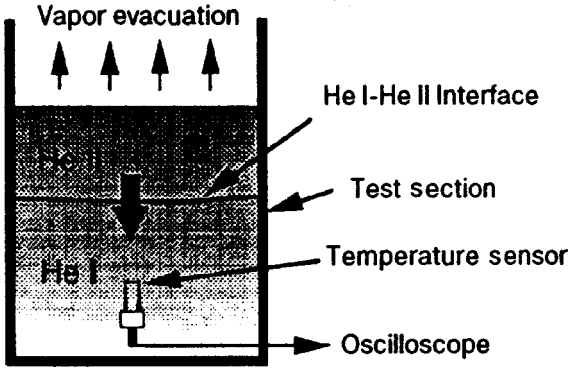


FIG. 2. Schematic illustration of a propagating interface downward and a superconductive temperature sensor.

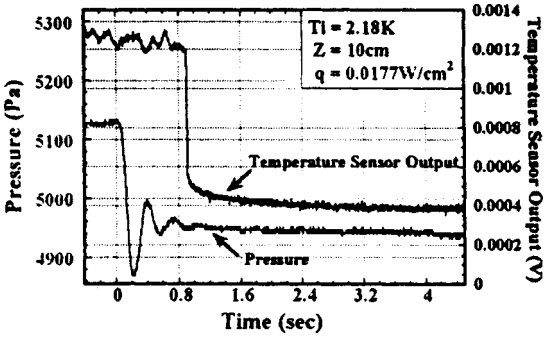


FIG. 4. Typical example of the experimental data; the time variations of the vapor pressure and the output from the superconductive sensor located at 10 cm below a free surface. $T_i = 2.18$ K, $q = 0.0177$ W/cm$^2$.

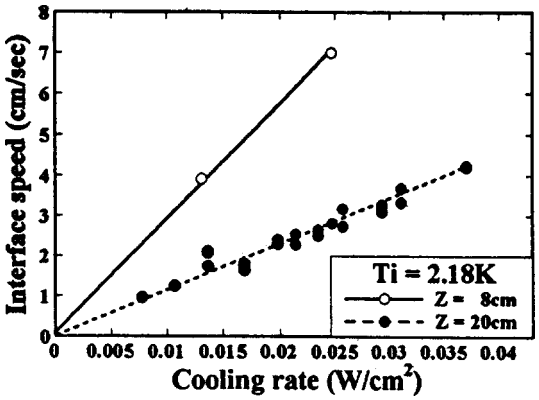


FIG. 5. Variation of the interface propagation speed with the net cooling rate. $T_i = 2.18$ K.

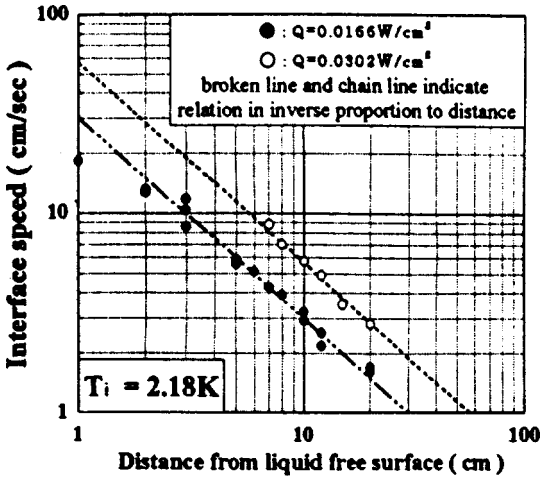


FIG. 6. Interface speed as a function of distance from a free surface. $T_i = 2.18$ K, $q = 0.0166$ W/cm$^2$ and 0.0302 W/cm$^2$

superfluid breakdown state where small temperature gradient develops due to the effect of tangled mass of quantized vortices. Thus, we reached some conclusion as follows: Heat transfer toward an interface is highly confined within a narrow region just in front of an interface in He I. There exists a very small temperature gradient in He II phase behind an interface and the temperature of a free surface also drops quite slowly during an experimental run.

The variation of the interface propagation speed with the cooling rate is shown in Fig. 5. Here, the cooling rate is corrected to compensate the parasitic heat leak into the He II bath in the following manner as the cooling rate converted from the vapor flow rate minus the parasitic heat leak. This means that there exists a minimum cooling rate, equal to the parasitic heat leak, below which no interface appears. The propagation speed is measured by a double probe sensor located at 20 or 8 cm from a free surface, respectively. It is confirmed that a He I–He II interface propagates downward with a speed of several centimeters per second in direct proportion to the cooling heat flux and the speed varies with the distance from a free surface. In Fig. 6 the interface speed is plotted as a function of distance from a free surface for two cases of the cooling rates. It is seen that the interface speed decreases approximately in inverse proportion to the distance from a free surface except in the very initial phase of propagation near a free surface. It is experimentally suggested that the propagation speed is finite at the beginning of propagation from a free surface and then it approaches to the inversely proportional law.

It is found from Schlieren visualization pictures that a phase boundary layer propagates quite stably provided that the cooling rate is larger than a critical value. In the case of small cooling rate an interface layer once appeared is found to terminate propagation halfway in the Dewar and then gradually to disappear remaining stationary. The thickness of an interface layer seems to increase as the propagation with the lapse of time.

A phase boundary is also observed through high sensitivity Schlieren visualization in the case of cooling of subcooled (pressurized) He I by a J–T cooler in the subcool cryostat, where subcooled He II develops from the bottom of the test section. It is found that after the J–T cooling is stopped a phase boundary turns into an unsteady irregular pattern and then gradually disappears as a result of temperature rise due to parasitic heat input.

This study is carried out as a part of ''Space Utilization Frontiers Joint Research Projects'' promoted by NASDA Japan, and Japan Space Utilization Promotion Center.

*E-mail: murakami@superhe2.kz.tsukuba.ac.jp

[1] G. Ahlers and F. Liu, J. Low Temp. Phys. **105**, 255 (1996).
[2] A. Onukl, J. Low Temp. Phys. **404**, 133 (1996).
[3] G. Ahlers, Rev. Mod. Phys. **52**, 489 (1980).

This article was published in English in the original journal.

# Propagation of short nonlinear second-sound pulses through He-II in one- and three-dimensional geometry

V. B. Efimov, G. V. Kolmakov, A. S. Kuliev, and L. P. Mezhov-Deglin

*Institute of Solid State Physics RAS, 142432, Chernogolovka, Moscow distr., Russia*[*]
Fiz. Nizk. Temp. **24**, 116–121 (February 1998)

The results of an experimental study of the evolution of the shape of nonlinear second-sound pulses in superfluid He-II are reported. The pulses propagate in the bulk ($3D$ geometry) and along a cryoacoustic waveguide filled with liquid helium (quasi-$1D$ geometry) at temperatures corresponding to the negative, positive, or zero nonlinearity coefficient. A strong dependence of the shape of the propagating pulse on the dimensionality of the wave was observed. The finite size of the heater (generator of a sound) affects the profile of a short $3D$ pulse even at distances many times greater than the heater size, which restricts the minimal width of the excited pulse. The experimental data are compared with the results of numerical simulations.
 [S1063-777X(98)00502-7]

## INTRODUCTION

The waves of the entropy (second sound) are macroscopic quantum effects which may be observed in a superfluid liquid and perfect crystals.[1,2] The properties of the second sound in a superfluid $^4$He (He-II) were studied extensively, both experimentally and theoretically. More recently, the attention has been focused on the study of nonlinear acoustic properties of superfluid He-II.[3–7]

We report here on experimental and theoretical investigations of the peculiarities of nonlinear evolution of a solitary second-sound pulse in He-II under different geometrical conditions of excitation and propagation of the pulse.

As can be seen from further comparison of the shape of the recorded pulse with the results of computer simulations, one must take into account not only the strong nonlinearity of He-II, but also finite dimensions of the heater (generator of the second sound) and receiver (bolometer).

Evolution with time of the propagating second-sound pulse is defined by dispersive and nonlinear properties of the superfluid and geometrical conditions of the propagation. From the analytical point of view, the partial differential equation that describes the evolution of the shape of a wave traveling through an unrestricted medium can be reconstructed unambiguously from two important properties: the dispersion law of the wave $\omega(k)$ and the vertex function of nonlinear self-interaction $\Gamma(k,k_1,k_2)$, which is the amplitude characterizing the strength of three-wave interaction.[8]

For the second sound in superfluid $^4$He at temperatures $T>0.9$ K (roton second sound) but not very close to $T_\lambda$ (so that $\omega<c_2/\xi$, when $\xi$ is correlation length) and at frequencies lower than the inverse time which characterizes phonon-roton interaction, $\omega<c_2/c_1\tau_{r-\mathrm{ph}}$, the spectrum $\omega(k)$ is a linear function of the wave vector $k$, $\omega(k)=c_2k$ (here $c_1$ and $c_2$ are velocities of the first- and second-sound waves of infinitely small amplitude).[2] The vertex $\Gamma$ can be evaluated from the Landau equations of two-fluid hydrodynamics using the method similar to Ref. 9 which gives $\Gamma(k,k_1,k_2)=\mathrm{const}\,\alpha(kk_1k_2)^{1/2}$, where $\alpha$ is the nonlinearity coefficient of the second sound,

$$\alpha=c_2\frac{\partial}{\partial T}\ln\left(c_2^3\frac{\partial\sigma}{\partial T}\right).$$

Here $\sigma$ is the entropy per unit of mass. The sign of the nonlinearity coefficient $\alpha$ depends on temperature of the helium bath:[2] $\alpha>0$ at $T<T_\alpha=1.88$ K as in ordinary matter, and $\alpha<0$ at $T_\alpha<T<T_\lambda$.

At temperatures of the bath close to $T_\alpha$ the three-wave interaction is small [because $\Gamma(k,k_1,k_2)\to0$] and one must account for the next nonlinear term in the expansion of the evolution equation over the amplitudes of the sound. This term is proportional to the vertex of four-waves interaction $\Gamma^{(4)}(k,k_1,k_2,k_3)$ of the second sound.

In real experiments the amplitude of the excited second-sound waves, $\delta T_{\max}$, is restricted from above by the conditions of film boiling of the superfluid near the generator (heater): from our measurements of the heat pulses with duration $\tau_e\approx10$ $\mu$s the critical value of the heat flux density is $Q_0\approx25$ W/cm$^2$, which corresponds to $\delta T_{\max}<10$ mK in the temperature range of the measurements. At such amplitudes of the second sound the four-wave interaction is sufficiently weak and the condition $|\Gamma^{(4)}|\,\delta T_{\max}^2\ll c_2/L$ holds. Accordingly, at $T=T_\alpha$ no changes in the shape of a traveling pulse have been observed at distances from the heater to the bolometer up to $L\approx10$ cm. One can therefore observe a ''ballistic'' travel of the pulse from the generator to the detector without any evolution of its shape at bath temperatures $T\approx T_\alpha$, in contrast to the case $T\neq T_\alpha$, when the nonlinear transformation of the pulse is significant and the shock second-sound wave is formed at small distances from the heater.

At temperatures very close to $T_\lambda$ the nonlinearity coefficient tends to infinity according to the power law $\alpha\sim\varepsilon^{-1}$, where $\varepsilon=(T_\lambda-T)/T_\lambda$ is the reduced temperature.[7] Near the lambda point the nonlinear properties of the second sound therefore play the crucial role even for a wave with a small amplitude.[6]

Since the second sound has linear dispersion law and a square root-like dependence of the vertex $\Gamma$ on the wave vectors, the evolution of the shape of one-dimensional

second-sound pulse $\delta T(x,t)$ is governed by the Burgers equation.[7]

$$\frac{\partial \delta T}{\partial t} + \alpha \delta T \frac{\partial \delta T}{\partial x} = \mu \frac{\partial^2 \delta T}{\partial x^2}. \quad (1)$$

The last term describes the dissipation of the wave and is introduced to preserve the turnover of the wave front. Here $\mu$ is the damping coefficient.

If $T \neq T_\alpha$ ($\alpha \neq 0$), the nonlinear evolution leads to the creation of a shock at the profile of the traveling pulse. The width of the shock front $d_f$ is defined by the nonlinear term and the dissipative term, $d_f = \mu/\alpha\Delta T$. The velocity of shock propagation is $v_f = c_2 + \alpha\Delta T/2$ (Refs. 1 and 2). At large distances $L$ from the heater, the profile of a 1D shock wave, acquires the final form presented by a triangle. The dependence of the length of the triangle (duration of the pulse $\tau$) and its height (the temperature jump at the shock front $\Delta T$) can be described by a universal power law,

$$\tau = \text{const}(\alpha L)^{1/2}, \quad \Delta T = \text{const}(\alpha L)^{-1/2}, \quad (2)$$

where the constants depend on the former shape of the second-sound wave. It is important to note that the evolution of the developed shock wave (i.e., the dependence of the parameters of the triangle on distance) is governed only by the value of the nonlinearity coefficient and does not depend on the value of the dissipation $\mu$. The entropy production rate $dS/dt$ at the shock front due to dissipation processes remains finite as dissipation coefficient $\mu$ tends to zero, because the small value of $\mu$ is compensated for by a big gradient, $\delta T' \sim \Delta T/d_f$. Because of this circumstance, the coefficient $\mu$ does not enter in the expressions (2).

## 2. RESULTS OF THE INVESTIGATIONS

The changes in shape of a solitary second-sound pulse have been studied as a function of duration of the electric pulse $\tau_e$ applied to a heater, as a function of emitted heat power $Q$ and the distance $L$ between the source and the superconducting bolometer at three temperatures which correspond to positive (at $T = 1.5$ K), negative ($T = 2.02$ K) and zero ($T = 1.88$ K) values of the nonlinearity coefficient $\alpha$. The experiments were performed under three different geometrical conditions: a) one dimensional (1D) geometry, when the second-sound pulse travels along the cryoacoustic waveguide—a long capillary with inner diameter $d = 3$ mm filled with superfluid helium; b) ''an open'' (3D) geometry, when a spherical pulse propagates through a bulk of the liquid, and c) combined geometry, when a formerly excited 3D spherical pulse enters into a capillary placed at some distance from the source and after that propagates along the waveguide as a quasi-1D wave.

a) Experiments on the propagation of 1D second-sound pulse have been divided by two parts. At the beginning, we studied the evolution of the pulse shape with increasing distance $L$ at a constant power $Q$ and duration of a rectangular electrical pulse $\tau_e = 10$ $\mu$s. The distance $L$ was increased by a step from 0.7 cm to 8.5 cm.

The typical dependence of the shape on the distance $L$ measured at the bath temperature $T = 2.02$ K ($\alpha < 0$) is shown in Fig. 1. It can be seen that for the pulse with initial amplitude $\delta T \sim 3$ mK the shock is formed at the back side of the pulse at a distance $L < 0.7$ cm. The dependence of the amplitude of the wave on the distance $L$ is described well by expressions (2). At $\alpha > 0$ the shock appears at the front of the pulse (which is a general situation in classic nonlinear acoustics).

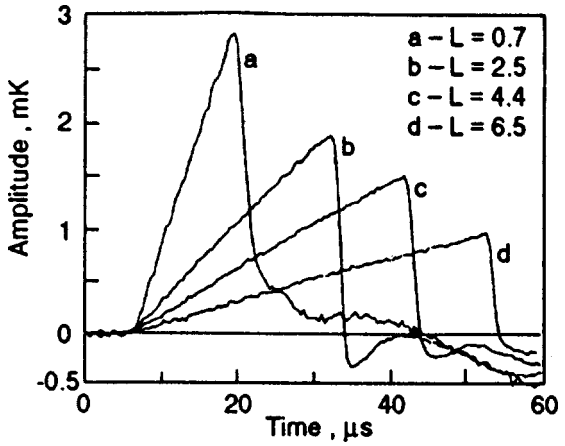


FIG. 1. Evolution with the distance $L$ of the one-dimensional second-sound pulse propagating in a long capillary. The bath temperature is $T = 2.02$ K ($\alpha < 0$). The emitted heat power is $Q = 20$ W/cm$^2$, $\tau_e = 10$ $\mu$s. The distance $L$ if measured in cm.

Figure 2 shows the evolution of the second-sound pulse profile at $T = 1.5$ K with increasing heat power from $Q = 2.4$ W/cm$^2$ to $Q = 20.2$ W/cm$^2$ at a constant distance $L = 2.5$ cm and heat pulse duration $\tau_e = 10$ $\mu$s. We see that the slope of the profiles $a = \Delta T/\tau$ does not depend on $Q$: in accordance with the general relations (2), the value $a = c_2/\alpha L$.

We see from Figs. 1 and 2 that the pulses traveling in a capillary are followed by oscillating tails with the amplitudes of the order less than the amplitude of the pulse. The appearance of these tails could be attributed to the nonideality of the experimental cell: the heater consists of a rectangular thin metal film $1.2 \times 2$ mm; its dimensions are therefore less than the inner diameter of a capillary. The tails appear because of

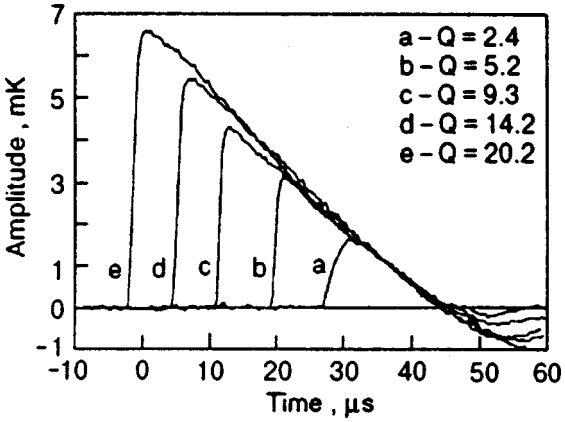


FIG. 2. Change in the shape of the one-dimensional pulse with increasing emitted heat power $Q$ from 2.4 W/cm$^2$ to 20.2 W/cm$^2$ at a fixed distance from the heater $L = 2.5$ cm and $\tau_e = 10$ $\mu$s. The bath temperature is $T = 1.50$ K ($\alpha > 0$).

the multiple reflection of the heater-irradiated nonplanar wave from the walls of the capillary. The subsequent computer simulation revealed the influence of the geometrical nonideality of the cell in the region near the heater on the shape of the recorded pulse.

b) Open (3D) geometry.

An evolution of shape of the spherical pulse propagating in the bulk of liquid helium with increasing power and electric pulse duration has been studied at three different temperatures $T=1.50$ K ($L=4.7$ cm), 1.88 K and 2.02 K (in two latter cases $L=5.8$ cm). The pulse was generated by the same heater immersed in superfluid helium.

It is known[5] that the second-sound wave generated in He-II by a point source heated by a rectangular electric pulse consists of a heating pulse (compression wave in the roton gas) followed by a cooling wave (rarefaction wave in the gas). In the linear approximation the amplitude of the traveling spherical pulse decreases as $\delta T_{\max}\sim 1/R$ with increasing distance $R$. Allowance for nonlinearity leads to slow (logarithmic) corrections to this dependence.[1] In the case of a shock wave we have $\Delta T\sim(1+\text{const}(\ln R))^m/R$, where the exponent $m$ depends on the asymptotic shape of the wave (and, hence, on the sign of the nonlinearity coefficient), and the constant in the latter relation is defined by initial conditions.

The shape of the bipolar pulse that was generated in He-II at $T=1.88$ K by the heat pulse of the same duration $\tau_e=10$ $\mu$s and the evolution of the shape with changing nonlinearity coefficient are illustrated in Fig. 3. The distance $L$ is fixed $L=5.8$ cm, and the heat density changes slightly from $Q=23$ W/cm$^2$ at $T=2.02$ K (upper graph), to $Q=21$ W/cm$^2$ at $T=1.88$ K (middle graph), and to $Q=16$ W/cm$^2$ at $T=1.50$ K (bottom graph). We see that the final shape of the bipolar nonlinear pulse depends significantly on the sign of the nonlinearity coefficient. If $\alpha>0$, two shocks appear at the profile of the pulse (at the front of the compression wave and at the back side of the rarefaction wave). If $\alpha<0$, the shock appears at the middle of the pulse. The asymptotic dependence of the jump $\Delta T$ at the shock front at large distances is defined by the final shape of the bipolar pulse: the exponent of the logarithmic factor $m=-1/2$ in the case of the profile with two shocks at the edges of the pulse and $m=-1$ in the case of the profile with a discontinuity in the middle.

In the experiments with spherical 3D pulses we have observed an unexpected dependence of the shape of the recorded pulse on the duration $\tau_e$ of an electric pulse (in contrast to the one-dimensional case). If $\tau_e$ is less than a characteristic time $\tau_0\approx 20$ $\mu$s, the detected bipolar pulse is presented by coupled heating and cooling pulses. But if $\tau_e$ exceeds $\tau_0$ one could observe a shell between the heating and cooling waves (a region with a zero deviation of the temperature from the temperature of the bath). The duration of electric pulse $\tau_0$ at which the shell appears depends only slightly on the temperature of the bath.

In order to explain the appearance of the shell we considered a simple theoretical model which describes the generation of linear second-sound pulse ($\alpha=0$) by a spherical heater with a radius $b$. We assumed that a rectangular electric pulse is applied to the heater. The problem involved can be mapped to a well-known problem of the wave equation for a scalar field $\varphi$ by introducing the hydrodynamic potential using the relation $\nabla\varphi=\mathbf{p}/S$. Here $\mathbf{p}$ is a momentum per unit of mass of relative motion of the normal and superfluid components of He-II, and $S$ is the entropy of a unit volume. The boundary conditions for the potential $\varphi$ express the continuity of the heat flux at the surface of the heater.

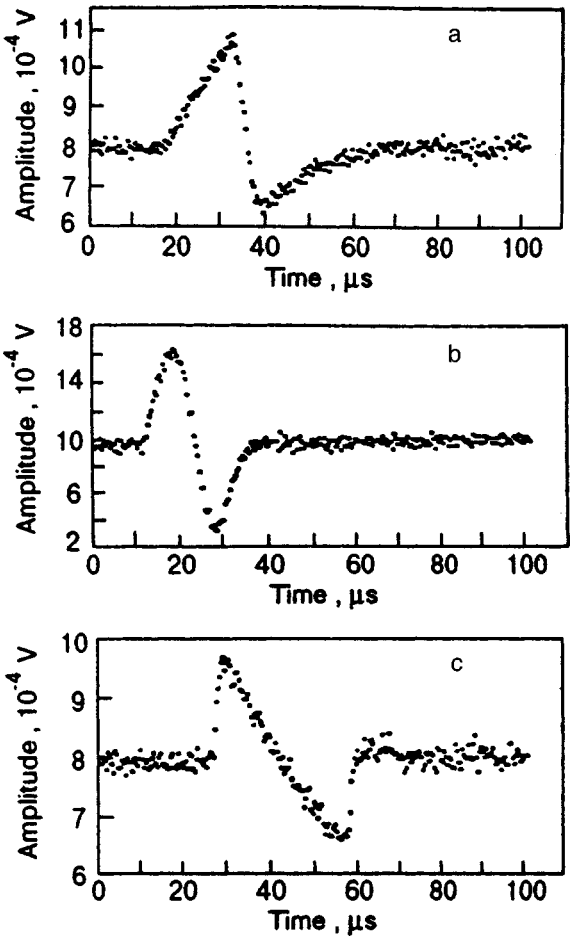


FIG. 3. Detected profile of the 3$D$ second-sound pulse at various temperatures. The distance $L=5.8$ cm, $\tau_e=10$ $\mu$s. a) $T=2.02$ K ($\alpha<0$) $Q=23$ W/cm$^2$; b) $T=1.88$ K ($\alpha=0$), $Q=21$ W/cm$^2$; c) $T=1.50$ K ($\alpha>0$), $Q=16$ W/cm$^2$.

The analyses of the solution show that, in contrast with the one-dimensional case, the shape of generated 3D second-sound pulse is defined by an integral relation and, in general, is proportional to a time derivative $dQ/dt$ with the exponentially decaying post-action with characteristic time $\tau_0\sim b/c_2$. For a rectangular heat pulse the observed profile of the second-sound wave that propagates through a liquid is given by two uncoupled thermal peaks if $\tau_e>\tau_0$. If $\tau_e<\tau_0$, the peaks overlap and the nonlinearity results in an additional broadening of the propagating pulse.

In order to evaluate the broadening $\tau_0$ we made a computer simulation of the generation of linear second-sound pulse, taking into account the real geometry of the heater (flat rectangular film). This gave the value of $\tau_0\approx 20$ $\mu$s, consistent with the measurements results.

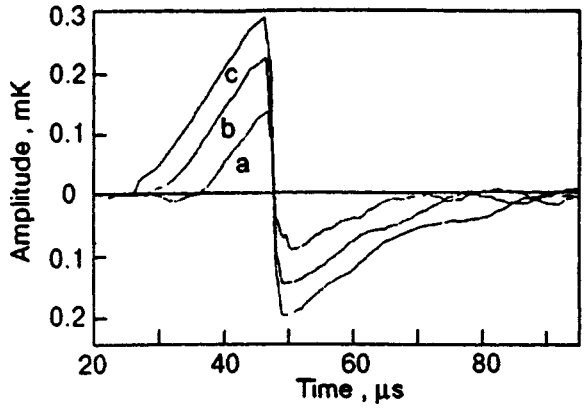


FIG. 4. The shape of the second-sound pulses detected at the far end of the capillary in the experiment with combined geometries. The bath temperature $T=2.02$ K, the heat pulse duration $\tau_e=10\ \mu$s. $Q=24$ W/cm$^2$ (a), $Q=9.2$ W/cm$^2$ (b), $Q=20$ W/cm$^2$ (c).

The results of such treatment can be used immediately only at $T=T_\alpha$ because the action of nonlinearity is ignored. As follows from previous considerations, the change in the duration of the pulse at $\alpha\neq 0$ is logarithmically small at finite distances, so the measured time $\tau_0$ must depend slowly on the temperature. This conclusion has been confirmed by our observations.

c) The combined geometry.

In these experiments the heater was placed at a distance of 1 cm outside the capillary. The heater generated a nearly spherical bipolar wave that can enter through the open edge of the capillary and propagate along it as a 1D wave. The profile of the pulse was measured at the far end of the capillary. This technique makes it possible to create quasi-one-dimensional bipolar second-sound pulse. As in pure spherical case, such a pulse propagates ''ballistically'' at $T=T_\alpha$ and two shocks appear at the edges of the pulse at $T<T_\alpha$ or the shock is formed in the middle of the pulse at $T>T_\alpha$.

Evolution of the shape of the pulse that propagates through a capillary with increasing heat power ($Q=2.4$, 9.2 and 20.2 W/cm$^2$) is shown in Fig. 4. The duration of the electric pulse is $\tau_e=10\ \mu$s (short pulse) and the length of the capillary is $\sim 5$ cm. The temperature of the liquid helium bath is $T=2.02$ K ($\alpha<0$).

Computer simulations of the nonlinear evolution of a 1D pulse with distance was performed in the framework of the Burgers equation. Two cases have been studied: a) a rectangular pulse was excited by a plane infinite heater and b) the initial condition for the wave is given by a sine-like function (a simulation of the combined geometry).

The results of calculations for this case are shown in Fig. 5. In case a) the bath temperature is assumed to be $T=1.6$ K and the initial amplitude of the pulse is 5 mK. We see a formation of the shock at the front of the pulse at a distance from the open edge of the capillary $L\sim 3$ cm.

In case b) the bath temperature is $T=2.1$ K. The shock appears at the center of the wave (in accordance with our previous considerations). The jump of the temperature $\Delta T$ decreases in inverse proportion to the distance $\Delta T\sim 1/L$. (Note that the direction of the $x$ axes on the two last plots is inverse with respect to previous plots; Figs. 1–4 correspond

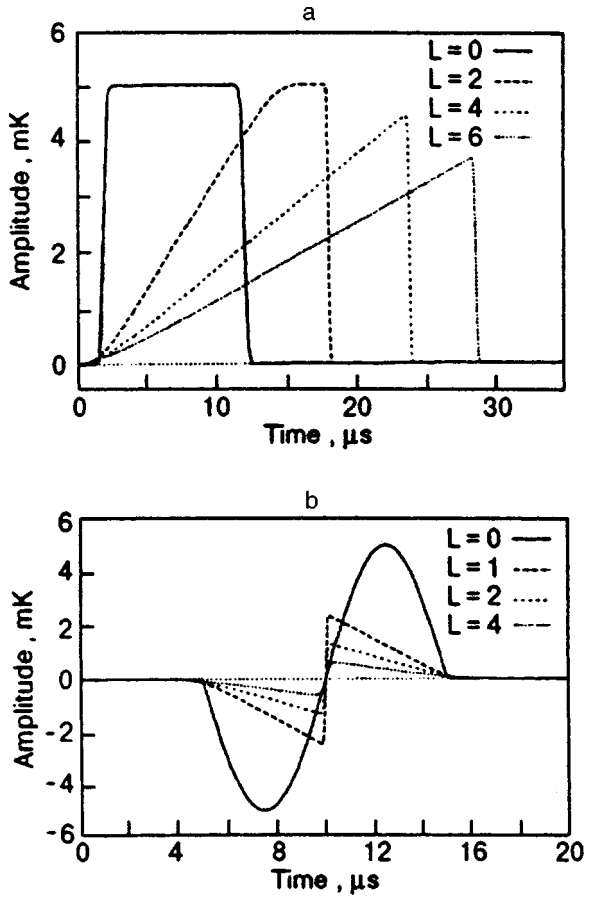


FIG. 5. Results of computer simulation of the evolution with distance of the $1D$ second-sound pulse. The distance $L$ is measured in cm. The rectangular pulse, the bath temperature is $T=1.6$ K ($\alpha>0$) (a). The sine-like initial pulse, the bath temperature is $T=2.1$ K ($\alpha<0$) (b).

to the signal recorded from the bolometer.) We see that the evolution of the second-sound pulses obtained in numerical simulations coincide qualitatively with the results of observations.

### 3. CONCLUDING REMARKS

Thus, the results of experimental and theoretical studies have shown that the shape of excited second-sound waves and their evolution due to nonlinear properties of superfluid helium depend strongly on the dimensionality of the wave and geometrical conditions of the generation and propagation of the wave, as well as on the temperature of the liquid-helium bath. For $3D$ pulses the influence of the finite dimensions of the source of the wave can not be ignored even at large distances.

Despite the relative simplicity of the equation that governs the evolution of the second-sound pulse (the Burgers equation), it exhibits a very interesting behavior. The character of the evolution and the final shape of the pulse can vary significantly under various conditions of the experiment.

It is interesting to note that the dependence of the $\Gamma(k,k_1,k_2)$ function on the wave vectors of the second-sound waves $\Gamma\sim(\Pi_{i=1\ldots3}k_i)^{1/2}$ is typical of a wide class of problems of the nonlinear wave propagation, and the Burgers

equation appears in many problems in nonlinear physics. In principle, this makes it possible to use the second sound in superfluid helium as an object for model study of many of nonlinear processes in optics and acoustics, in plasma physics, etc.

Interesting applications of the Burgers equation are also found in the theory of turbulence.[10] The experiments with nonlinear second sound could be useful for developing this theory.

Short nonlinear second-sound pulses could be very useful in investigations of dynamic phenomena very close to the lambda point: when a monochromatic second sound is emitted by a heater to which a sinusoidal voltage is applied, a steady heat flux is created in its interior, and the value of this flux is comparable to the oscillating part of the flux within the wave. The existence of such stationary counterflow results in the creation of quantum vortices in the superfluid liquid. This process is most important at temperatures close to $T_\lambda$ because the threshold of the vortex creation is small. This means that in the case of sinusoidal excitation of the heater, the generated monochromatic second-sound waves propagate through a strongly disturbed liquid, in contrast to studies with short heat pulses. This makes it possible to correctly investigate the dynamic and relaxation processes in the superfluid near the phase transition temperature. In this sense, it would be more correct to use the $1D$ bipolar second-sound pulses, because their nonlinear evolution is relatively simple: the length of the pulse is fixed by the conditions of generation and at the final stage there exists only one parameter $\Delta T$, which changes with distance. This could improve the accuracy of interpretation of the experimental data.

Thus, the experiments with short second-sound pulse performed under microgravity conditions could give, in principle, more accurate information about the behavior of the superfluid near and far from the phase transition. This work was supported in part by INTAS Grant 93-3645.

*E-mail: german@issp.ac.ru

[1] L. D. Landau and E. M. Lifshits, *Fluid Mechanics*, Pergamon, London (1959).
[2] I. M. Khalatnikov, *An Introduction to Superfluidity*, Benjamin, New York (1965).
[3] A. Yu. Iznankin and L. P. Mezhov-Deglin, Sov. Phys. JETP **84**, 1378 (1983).
[4] I. Yu. Borisenko, V. B. Efimov, and L. P. Mezhov-Deglin, Sov. J. Low Temp. Phys. **14**, 1123 (1988).
[5] L. P. Mezhov-Deglin, A. Yu. Iznankin, and V. P. Mineev, JETP Lett. **32**, 217 (1980).
[6] L. S. Goldner, G. Ahlers, and R. Mehrotas, Phys. Rev. B **43**, 12864 (1991).
[7] S. K. Nemirovskii, Usp. Fiz. Nauk **160**, 51 (1990).
[8] R. K. Dodd, J. C. Eilbeck, J. D. Gibbon, and H. C. Morris, *Solitons and Nonlinear Wave Equations*, Academic Press, London (1982).
[9] I. M. Khalatnikov and V. L. Pokrovskii, Sov. Phys. JETP **71**, 1974 (1976).
[10] E. Balkovski, G. Falkovich, I. Kolokolov, and V. Lebedev, Preprint: chao-dyn/9603015.

This article was published in English in the original journal. It was edited by S. J. Amoretty.

# Testing critical point universality along the λ-line

J. A. Nissen,[1] D. R. Swanson,[1] Z. K. Geng,[1] V. Dohm,[2] U. E. Israelsson,[3] M. J. DiPirro,[4] and J. A. Lipa[1]

[1]*Stanford University, Stanford, California 94305, USA**
[2]*Institut für Theoretische Physik, Technische Hochschule Aachen, D-52056 Aachen, Germany*
[3]*Jet Propulsion Laboratory, California Institute of Technology, Pasadena, California 91109, USA*
[4]*Goddard Space Flight Center, Greenbelt, Maryland 20771, USA*
Fiz. Nizk. Temp. **24**, 122–126 (February 1998)

We are currently building a prototype for a new test of critical-point universality at the lambda transition in $^4$He, which is to be performed in microgravity conditions. The flight experiment will measure the second-sound velocity as a function of temperature at pressures from 1 to 30 bars in the region close to the lambda line. The critical exponents and other parameters characterizing the behavior of the superfluid density will be determined from the measurements. The microgravity measurements will be quite extensive, probably taking 30 days to complete. In addition to the superfluid density, some measurements of the specific heat will be made using the low-g simulator at the Jet Propulsion Laboratory. The results of the superfluid density and specific heat measurements will be used to compare the asymptotic exponents and other universal aspects of the superfluid density with the theoretical predictions currently established by renormalization group techniques. 
[S1063-777X(98)00602-1]

## INTRODUCTION

One of the major successes of the modern theory of continuous phase transitions is the calculation of exponents which characterize the singular behavior of thermodynamic properties near the transition temperature. Due to substantial theoretical difficulties, so far there exists no exact treatment of critical phenomena in three dimensions. Consequently the calculations of exponents are approximate in all cases of experimental interest. The renormalization-group (RG)[1] theory does, however, make a number of exact predictions concerning the nature of the critical exponents. One is that within broad limits the critical exponents are constants independent of microscopic interaction or of macroscopic thermodynamic parameters. They are said to be universal, depending only on the number of degrees of freedom of the order parameter and the number of spatial dimensions of the system. The transition from superfluid to normal fluid helium, the lambda transition, offers the best opportunity to verify this exact prediction with experiment. For example, near the lambda transition, the critical exponent $\zeta$ of the superfluid density, $\rho_s = \rho_0(P)t^{-\zeta}$, is predicted to be a universal constant close to 2/3, where $t = 1 - T/T_\lambda(P)$ is the reduced temperature measuring the distance from the transition temperature, $T_\lambda$. By contrast, the amplitude $\rho_0(P)$ is a nonuniversal quantity depending on the pressure, $P$, of the isobar on which $\rho_s(t)$ is measured. Along with the critical exponents, certain ratios of amplitudes of thermodynamic quantities are also predicted to be universal.[2] Most data are roughly consistent with the predicted universality, i.e., with constant values of the critical exponents and amplitude ratios. However, in virtually all systems of interest the level of testing is very weak. Even in the case of the lambda transition of helium, where the most advanced tests have been performed,[3] some anomalies have been detected.[4]

Unlike continuous transitions in other fluids, the lambda transition is not a single critical point but rather is a line of transitions obtained by varying the hydrostatic pressure. It is possible to measure the critical exponent of the superfluid density with exceptional ease and accuracy due to a unique wave motion termed second sound, in which the temperature of the liquid rather than its pressure oscillates. Over the years many measurements of the velocity of second sound have been made, but only recently have attempts been made to access the deep asymptotic region, close to the transition, where the theoretical predictions are most accurate. Now it is possible to operate with the reduced temperature as small as $10^{-8}$, a factor of 1000 less than in earlier experiments. Previous ground-based experiments[5] indicate that the critical exponent for the superfluid density can be measured to better than 1 part in $10^4$. This is about an order of magnitude better than is possible with any other exponent, for any known physical system. With care, perhaps even higher accuracy can be obtained.

Unfortunately, the presence of gravity acting on the experimental cell reduces the reliability of the analysis of the results. The effects of gravity can be cancelled to first order by measuring the temperature $T_\lambda$ at the middle of the cell, however, close to the transition, gravity plays a dominant role in determining the apparent velocity of the wave, even in small cells. For $t \lesssim 10^{-7}$ second-order effects become important. Specifically the term $\nabla\rho_s$ must be included in the differential equation describing second sound.[6] Further reduction in cell size, below about 1 mm height, is inhibited by the presence of finite effects which distort the singular behavior of interest. To obtain a more accurate reflection of the idealized fluid behavior it is necessary to substantially reduce the effect of gravity in the experiment by performing the experiment in microgravity conditions.

Great care must be exercised in the interpretation of such experiments. At higher pressures, non-asymptotic corrections

to the superfluid density become more important, leading to an effective exponent which varies with pressure.[7] Clearly it is very important to distinguish between this nonuniversal effect and a violation of universality. Fortunately, a correction scheme has been developed,[8] based on RG calculations, which can be used to separate the nonuniversal from the universal effects in a quantitative way. Its utility has already been demonstrated on existing data over a restricted temperature range.[9] Part of the project will include a theoretical effort to improve the accuracy of this approach and define its limits more clearly.

To apply the correction, supplementary measurements of specific heat, $C_p$, or thermal expansion, $\beta_p$, are needed at all pressures of interest. Measurements performed in the Jet Propulsion Laboratory's low-$g$ simulator of the expansivity at various pressures will provide the needed data for the correction terms to the asymptotic behavior. If a pressure dependence of the superfluid density exponent along the lambda line is established, this would constitute a substantial problem for condensed matter theory: one of the central results of the RG theory on which the modern view of phase transitions is built would have been violated. Agreement with theory would represent the strongest support yet obtained.

### 1. UNIVERSALITY

One of the major achievements of the RG theory[1] was the proof of the universality hypothesis[10] of the critical behavior and the specification of the characteristics of the universality classes. Critical points of different physical systems having the same dimensionality and the same number of degrees of freedom of the order parameter are predicted to belong to the same universality class with identical critical exponents, scaling functions and certain ratios of amplitudes of singular thermodynamic quantities.[2] These universal properties are predicted to be independent of the strength of the interaction and can be calculated by RG methods on the basis of a statistical distribution $p(\Psi)$ for the order parameter $\Psi$. For example, the lambda transition of $^4$He is governed by the two-component (complex) wave function $\Psi$ of the Bose condensate and should have universal properties that are identical with those of two-component spin systems. In particular, these properties should be independent of the pressure $P$ at which the lambda transition occurs. This prediction can be tested by measuring thermodynamic quantities such as the superfluid density $\rho_s$, the specific heat $C_p$, and the thermal expansion coefficient $\beta_p$. The latter is known[3] to exhibit the same critical behavior as $C_p$. In a highly quantitative analysis of critical phenomena, non-asymptotic corrections are inevitable because data must be taken a finite distance from the transition temperature. The amplitudes of the correction terms are predicted to be nonuniversal and are expected to increase with increasing pressure.[8,11] Thus the test of universality in the high-pressure region will be planned at the outset as an analysis including non-asymptotic correction terms. These terms contain both universal and nonuniversal parameters. More specifically, close to the transition temperature, $T_\lambda(P)$, RG theory predicts[12] that

$$\rho_s \doteq \rho_0 |t|^\nu (1 + a_\rho |t|^\Delta + \ldots) \tag{1}$$

where the critical exponent for the superfluid density, $\zeta$, can be shown to be equal to the critical exponent for the correlation length, $\nu$, by the Josephson relationship. Also,

$$C_p = B + \frac{A^\pm}{\alpha} |t|^{-\alpha} (1 + a_c^\pm |t|^\Delta + \ldots) \tag{2}$$

where $\alpha$ is the critical exponent for the heat capacity at constant pressure and the $\pm$ signs refer to $T > T_\lambda$ or $T < T_\lambda$, respectively. Within the RG calculation, the quantities $\rho_0$, $B$, $A^+$, $A^-$, as well as the correction amplitudes $a_\rho$, $a_c^+$, $a_c^-$ turn out to depend on the (pressure dependent) parameters of the statistical distribution $p(\Psi)$ whereas the critical exponents $\nu$, $\alpha$ and the correction exponent $\Delta$ are universal, i.e., independent of these parameters. Certain ratios of the nonuniversal amplitudes, however, are predicted to be universal as well, for example, $A^+/A^-$, $a_c^+/a_c^-$, $a_\rho/a_c^-$. The analysis consists of two steps: first, to extract from the data those quantities that are predicted to be universal, and to determine their pressure dependence; second, to compare the measured values of these quantities with those predicted by RG calculations. Such analyses have previously been performed[3] for the superfluid transition of $^4$He at a level of quality limited by the accuracy of the data[7,13] available about 20 years ago.

The representations of $\rho_s$ and $C_p$ according to (1) and (2) are approximate in the sense that there exists a whole series (Wegner series[14]) of additional correction terms of the form $t^{2\Delta}$, $t^{3\Delta}$, etc. along with other terms. An appropriate application of the RG method makes it possible to sum up this Wegner series and to represent the correction terms in a closed functional form.[8,9,15] This representation is more complete and more accurate than the standard form (1) and (2) while containing the same number of nonuniversal parameters. It includes accurate field-theoretic functions obtained via high-order perturbation theory and Borel resummation.[16] Part of the planned theoretical effort is to calculate not only the universal amplitude ratios but also the resummed functional form of the correction terms more accurately by means of the field-theoretic RG approach. This will provide a more reliable basis for the combined non-asymptotic analyses of the data for $\rho_s$ and $C_p$ (or $\beta_p$) and will allow one to perform a controlled analysis over a larger temperature range outside the small asymptotic region. Furthermore it is planned to study the effect of additional correction terms arising from a possible cut-off dependence of the statistical distribution $p(\Psi)$.

### 2. SECOND SOUND

The central part of the experiment is a cylindrical resonator filled with high purity liquid helium. The sample chamber forms a second-sound resonator with a quality factor, $Q$, typically over 1 000. The $Q$ is limited by losses in the fluid and the end walls. Second-sound detectors based on rf SQUID technology with sensitivities of less than $10^{-10}$ K/$\sqrt{\text{Hz}}$ are already in routine laboratory use. For a flight experiment the maximum signal/noise ratio is desirable to decrease the measuring time. For this reason the sensing element will be coupled to an improved sensitivity dc squid magnetometer. Also to be evaluated is the two-stage SQUID

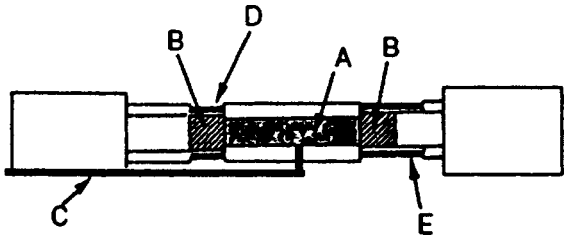


FIG. 1. Second-sound resonator: A) helium, B) paramagnetic salt, C) fill line, D) pickup coil, E) driving coil and astatic coil.

readout scheme being developed at Goddard, which promises even lower noise.[17] The second-sound resonator will utilize a magnetically driven paramagnetic salt as a low dissipation second-sound generator.

The resonator is attached to a high resolution paramagnetic salt thermometer and a superconducting pressure controller. The proposed experiment makes full use of the high resolution thermometry[18] developed primarily for the Lambda Point Experiment (LPE)[19] and the Confined Helium Experiment (CHEX)[20] flight programs. The present status of the high resolution thermometry is that the noise level is set by intrinsic thermal fluctuation phenomena. In the CHEX configuration this leads to a limiting resolution of about $10^{-10}$ K in a 1 Hz bandwidth. Integration over longer periods allows resolutions deep in the $10^{-12}$ range with the ultimate performance set by sensor and electronics drift. The pressure transducer is currently under development with separate NASA funding and has not yet been flown. It represents a significant development effort, but all elements of the device exist in other applications. The main parts of the sensor element are derived from the gravitational wave detector at Stanford where displacements of $10^{-17}$ m are monitored. This demonstrated sensitivity far exceeds our needs. Closed loop pressure control at resolutions of $10^{-9}$ has not yet been demonstrated, but bandwidth requirements are extremely modest, less than 1 Hz, so little difficulty is expected.

This assembly will be placed within a multi-stage thermal enclosure similar to that flown on the LPE. The only significant change in this part of the apparatus will be the use of a tighter thermal link between the cell and the inner stage of thermal isolation. This change will allow a faster response thermal control loop on the cell, and more rapid cooling for repeating temperature scans. The walls of the enclosure will be maintained near 1.7 K to allow operation of the sample chamber at various temperatures along the lambda line. This basic operating temperature will be maintained by using a superfluid helium cryostat with a long hold time (30–50 days) which is needed for completing the measurements at a number of different pressures.

To perform the experiment, the pressure is first set at the desired value by adjusting the reference pressure of the controller system using high pressure $^3$He gas. This level of pressure adjustment need only be done relatively crudely, say to an accuracy of about 1%. Once set, this pressure needs to be held constant to within about 1 part in $10^9$ using the internal controller. Next, the temperature of the cell is raised ever closer to the lambda point and the fundamental resonant frequency plus harmonics of the cavity are measured. Values in the range 1 to 500 Hz are expected. Frequency and temperature measurements are continued until the transition is reached, marked by loss of the signal. A number of temperature sweeps at a given pressure will be performed to check for errors in the data and to estimate the uncertainties in the results. Additional checks on the transition temperature will be made by observing the response of the cell to pulsed heat inputs applied with the second-sound generator. The pressure would then be reset and the measurement sequence repeated. In each resonant frequency measurement, the $Q$-curve of the resonator would be scanned to improve the accuracy of the determination of the central frequency.

It should be noted that second-sound measurements have already been made to within 20 nK of the transition in ground experiments.[5,21] Thus there is no additional need to demonstrate feasibility of the basic measurement technique. The problem is to reduce the huge gravitational distortion that makes such experiments difficult to interpret. Only a layer of the sample about 0.2 mm thick can be considered to be that close to the transition; the rest is further away due to the shift in $T_\lambda(P)$ caused by the hydrostatic head. In space, the effective thickness of this layer will grow to about 10 cm, filling the whole resonator. This measurement would also give new information on a second parameter of interest, the damping coefficient of the thermal wave. The behavior of this quantity near the transition is of importance in the testing of the theory of dynamic critical phenomena.

### 3. EXPANSIVITY

To perform the tests of the universality prediction for the superfluid density it is necessary to have information on the heat capacity behavior (or $\beta_p$) over a limited range. We plan to use the low-$g$ simulator at JPL for these measurements. The volume over which the effective gravity environment can be reduced to the 0.01 g level in the simulator is limited to about 0.5 cubic centimeter. Due to the necessarily small sample volume we believe the highest quality data can be obtained by performing expansion coefficient measurements, which relate directly to heat capacity data. Following Mueller *et al.*,[13] the expansion coefficient measurements will be performed using a standard ''hot volume'' technique in which the sample helium in the low-gravity simulator is connected via a small capillary to a second volume containing a high resolution pressure gauge. The temperature of the hot volume chamber is changed in response to a small change in the sample volume temperature such that the pressure is held constant. The expansion coefficient is calculated from the applied change in temperature in the sample cell and the calculated change in density of the hot volume as deduced from it's change in volume. A pressure regulation of 0.15 mbar has been demonstrated routinely with this technique corresponding to a temperature noise in the sample chamber of about 0.3 nK at a pressure of 10 bar and 3 nK at a pressure of 1 bar. We plan to take data from 1 bar up to 30 bar. Due to the very large magnetic field present in the low-$g$ simulator, temperatures are measured using melting curve thermometry.[22] The demonstrated resolution of these thermometers is about 3 nK in a 1-Hz bandwidth. The proposed

measurement technique would thus be limited by thermometer noise in all but the very lowest pressure range studied.

## CONCLUSION

The results from the experiment described here would become a major new test of the theory of second-order phase transitions in condensed matter. The measurements would probe the applicability of the universality prediction to an unprecedented degree, and possibly to the maximum extent feasible with known technology. If the prediction is found to fail, it would be a major blow to current ideas on the origins of second-order transitions, and would mean that critical phenomena are more complicated than the RG theory suggests. If it is found to be valid, this theoretical framework, for which K. Wilson received the Nobel Prize in 1982, would be placed on a much sounder footing of supporting experimental evidence. As a secondary result, new data would be obtained on the behavior of the second sound damping coefficient very near the transition, as an aid to the developing theory of dynamic critical phenomena. The experiment is expected to be available for launch in the second half of 2002.

We wish to thank the Office of Life and Microgravity Science and Applications of NASA for its support with contract JPL 960613.

*E-mail: joel@chex.stanford.edu

[1] K. G. Wilson and J. Kogut, Phys. Rep. **C12**, 76 (1974); M. E. Fisher, Rev. Mod. Phys. **46**, 597 (1974).
[2] V. Privman, P. C. Hohenberg, and A. Aharony, in Phase Transitions and Critical Phenomena 14, C. Domb and J. Lebowitz (Eds.), Academic Press, NY (1991), p. 1.
[3] A. Singsaas and G. Ahlers, Phys. Rev. B **30**, 5103 (1984); G. Ahlers, Rev. Mod. Phys. **52**, 482 (1980); T. Takada and T. Watanabe, J. Low Temp. Phys. **41**, 221 (1980); F. M. Gasparini and M. R. Moldover, Phys. Rev. B **12**, 93 (1975); also, Ref. 12.
[4] F. M. Gasparini and A. A. Gaeta, Phys. Rev. B **12**, 1466 (1978); see also: J. A. Lipa, Q. Li, T. C. P. Chui, and D. Marek, Nucl. Phys. B **5A**, 31 (1988).
[5] M. J. Adriaans, D. R. Swanson, and J. A. Lipa, Physica 194–196, 733 (1994).
[6] D. R. Swanson, T. C. P. Chui, and J. A. Lipa, Phys. Rev. B **46**, 9043 (1992).
[7] D. S. Greywall and G. Ahlers, Phys. Rev. A **7**, 2145 (1973).
[8] V. Dohm, Z. Phys. B **60**, 61 (1985); J. Low Temp. Phys. **69**, 51 (1987).
[9] R. Schloms and V. Dohm, Europhys. Lett. **3**, 413 (1987).
[10] L. P. Kadanoff, in *Critical Phenomena*, Proc. of the Enrico Fermi Int. School of Physics **51**, M. S. Green (Ed.), Academic Press, New York (1971), p. 100.
[11] V. Dohm, in Proc. of the 17th Int. Conf. on Low Temp. Phys., U. Eckera, A. Schmid, W. Weber, and H. Wuehl (Eds.), North Holland (1984), p. 953.
[12] R. Schloms and V. Dohm, Phys. Rev. B **42**, 6142 (1990).
[13] K. H. Mueller, G. Ahlers, and F. Pobell, Phys. Rev. B **14**, 2096 (1976).
[14] F. Wegner, Phys. Rev. B **5**, 4529 (1972).
[15] V. Dohm and R. Schloms, unpublished.
[16] R. Schloms and V. Dohm, Nucl. Phys. **B328**, 639 (1989).
[17] M. DiPirro, P. J. Shirron, and J. G. Tuttle, Proc. 1994 Microgravity Low Temp. Phys. Workshop, p. 374 (1994).
[18] T. C. P. Chui, D. Swanson, M. J. Adriaans, J. A. Nissen, and J. A. Lipa, Phys. Rev. Lett. **69**, 3005 (1992).
[19] J. A. Lipa, D. R. Swanson, J. A. Nissen, T. C. P. Chui, and U. E. Israelsson, Phys. Rev. Lett. **76**, 944 (1996).
[20] X. Qin, J. A. Nissen, D. R. Swanson, P. R. Williamson, D. A. Stricker, J. A. Lipa, T. C. P. Chui, and U. E. Israelsson, Cryogenics **36**, 781 (1996).
[21] M. J. Adriaans, Thesis, Stanford University (1994).
[22] L. S. Goldner, N. Mulders, and G. Ahlers, Proc. Int. Symp. Temp. (1992).

This article was published in English in the original journal.

# Hydrodynamic impulse and energy of vortex tangle in superfluid turbulent He-II

S. K. Nemirovskii and V. A. Lushnikov

*Institute of Thermophysics, Lavrentyeva Are. 1, 630090 Novosibirsk, Russia**
Fiz. Nizk. Temp. **24**, 127–131 (February 1998)

The average hydrodynamic impulse (or Lamb impulse) $\mathbf{J}_V$ in the counterflowing, superfluid, turbulent He-II and the kinetic energy $E$, which is associated with the chaotic vortex filaments, are calculated. These quantities are defined as averages of the classical quantities taken over the stochastic vortex loop distribution. The averaging procedure was performed by using the Gaussian model of the chaotic vortex tangle elaborated earlier. Calculations show that the quantity $\mathbf{J}_V$ has only a component in the direction of external counterflow velocity (created, e.g., by a heater). As for the energy, it is shown that besides the usual local contribution, the quantity $E$ includes additional terms due to a long-range interaction. Some dynamic properties of the turbulent He-II due to the impulse and energy of the vortex configuration, such as suppression of the superfluid density and decrease in the velocity of the second sound that propagates in the superfluid turbulent He-II, are discussed.  [S1063-777X(98)00702-6]

## 1. INTRODUCTION

It is widely appreciated that a chaotic tangle of quantized vortex filaments [vortex tangle (VT)] or superfluid turbulence (ST) appears in the superfluid component whenever the velocity of flow (or counterflow; see Fig. 1) exceeds a fairly small, critical value (see, e.g., Ref. 1). The presence of a vortex tangle essentially changes the hydrodynamic properties of superfluid helium (see, e.g., Refs. 2 and 3). Accordingly, the phenomena are studied in the framework of so-called phenomenological theory (PT) which was pioneered by Feynman[4] and Vinen[5] and greatly modified by Schwarz.[6] The PT describes ST in terms of the total length of vortex lines or vortex line density (VLD) $\mathscr{L}(t)$ and of the structure parameters of the VT. Knowledge of these quantities allows us to calculate some of the hydrodynamic characteristics of superfluid turbulent He-II such as mutual friction, sound attenuation, etc. There exist many other physical quantities connected with the distribution of the filaments and with their interaction, which is related to other physical phenomena that cannot be expressed in terms of the PT. The relevant phenomena should be covered by appropriate stochastic theory of chaotic vortex filaments. Of course, the most honest way to develop such a theory is to study stochastic dynamics of vortex filaments on the basis of the equations of motion with a source of chaos. However, due to extremely involved dynamics of vortex lines this method seems to be almost hopeless. We would like to offer another approach. The main idea and main strategy are the following. Despite the fact that phenomenological theory deals with average quantity $\mathscr{L}(t)$, this approach, supplemented by experimental results and by some speculations, gives some information concerning the arrangement of the VT. We know that the VT consists of closed loops [labelled by $\mathbf{s}_j(\xi)$; see Fig. 2], which are uniformly distributed in space and which have the total length $\mathscr{L}(t)$ per unit volume. From acoustical experiments it follows that filaments are distributed in an anisotropic manner, and that quantitative characteristics of this anisotropy can be expressed by some structure parameters (see Refs. 1, 3, and 6). Besides this ordinary anisotropy, there is a more subtle anisotropy connected with the average polarization of the vortex loops. Furthermore, there is some proof that average curvature of the vortex lines is of the order of the inverse interline space and the coefficient of this proportionality was obtained in the numerical simulations made by Schwarz.[6] The master idea of my proposal is to construct a trial distribution function (TDF) in the space of the vortex loops of the most general form, which satisfies all of the established properties of the VT. We assume that this trial distribution function will enable us to calculate any physical quantities due to the VT.

In this paper we calculate the average hydrodynamic impulse (or Lamb impulse) $\mathbf{J}_V$ in the counterflowing, superfluid, turbulent He-II and the average kinetic energy $E$ which is associated with the chaotic vortex filaments.

## 2. CONSTRUCTION OF THE TRIAL DISTRIBUTION FUNCTION

According to general prescriptions, the average of any quantity $\langle \mathscr{B}(\{\mathbf{s}_j(\xi_j)\})\rangle$, which depends on the vortex loop configurations, is

$$\langle \mathscr{B}(\{\mathbf{s}_j(\xi_j)\})\rangle = \sum_{\{\mathbf{s}_j(\xi_j)\}} \mathscr{B}(\{\mathbf{s}_j(\xi_j)\})\mathscr{P}(\{\mathbf{s}_j(\xi_j)\}). \qquad (1)$$

Here $\mathscr{P}(\{\mathbf{s}_j(\xi_j)\})$ is the probability of the vortex tangle to have a particular configuration $\{\mathbf{s}_j(\xi_j)\}$. The meaning of summation over all vortex loop configurations $\Sigma_{\{\mathbf{s}_j(\xi_j)\}}$ in Eq. (1) will be clear from further analysis.

We make the usual assumption in statistical physics that all configurations corresponding to the same macroscopic state have equal probabilities. Thus, the probability $\mathscr{P}(\{\mathbf{s}_j(\xi_j)\})$ for vortex tangle to have a particular configuration $\{\mathbf{s}_j(\xi_j)\}$ should be proportional to $1/N_{\text{allowed}}$, where $N_{\text{allowed}}$ is the number of allowed configurations, which, of course, is infinite:

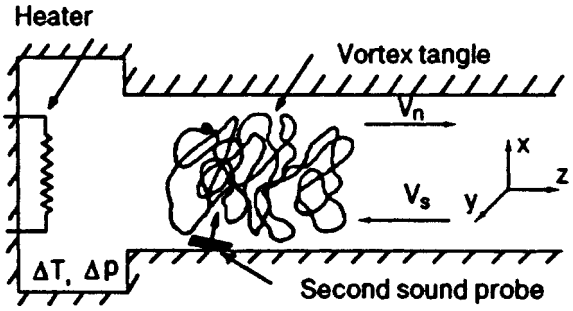


FIG. 1. Turbulent counterflow in He-II. The normal component flows from the heater carrying a heat flux $q=STV_n$; the superfluid component flows toward the heater. Total mass flow $\mathbf{J}=\rho_n\mathbf{V}_n+\rho_s\mathbf{V}_n=0$. Also shown are the axes used in this paper; the $z$ axis is directed along the normal velocity $\mathbf{V}_n$, the $x$ and $y$ axes are arbitrary; however, symmetry between $x$ and $y$ is assumed. Usual measured quantities are the temperature drop or/and pressure, attenuation, and velocity of the second sound that propagates at different angles through the counterflow, shape of heat pulses, etc.

$$\mathscr{P}(\{\mathbf{s}_j(\xi_j)\})\propto\frac{1}{N_{\text{allowed}}}. \tag{2}$$

*By ''allowed configurations'' $N_{\text{allowed}}$ we mean only the configurations that lead to the correct values for all average quantities known from experiment and numerical simulations.*

Formally, it can be expressed as a path integral in the space of three-dimensional (closed) curves supplemented with some constraints connected to the properties of the VT:

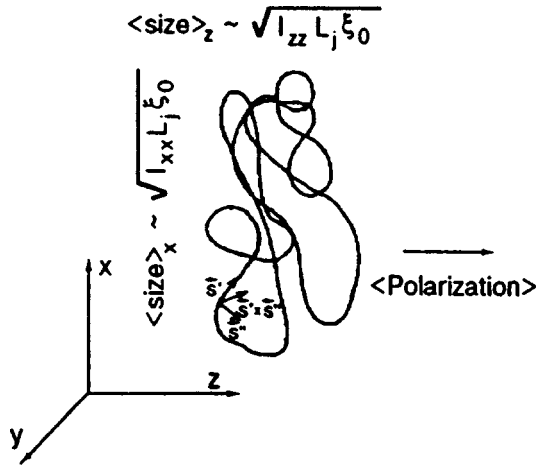


FIG. 2. A snapshot of the average vortex loop obtained from analysis of the statistical properties. The position of the vortex line element is described as $\mathbf{s}_j(\xi_j)$, where $\xi_j$ is the arc length, $\mathbf{s}_j'(\xi_j)=d\mathbf{s}_j(\xi_j)/d\xi_j$ is the tangent vector, unit vector along the vortex line; $\mathbf{s}_j''(\xi_j)=d^2\mathbf{s}_j(\xi_j)/d\xi_j^2$ is the local curvature vector; vector production $\mathbf{s}_j'(\xi_j)\times\mathbf{s}_j''(\xi_j)$ is binormal, which is responsible for the mutual orientation of the tangent vector and the vector of curvature. Close ($\Delta\xi\ll R$, where $R$ is the mean curvature) parts of the line are separated in $3D$ space by a distance $\Delta\xi$. The distant parts ($R\ll\Delta\xi$) are separated in $3D$ space by a distance $(2\pi R\Delta\xi)^{1/2}$ (with a correction due to the closeness). The latter property reflects a random walk structure of the vortex loops. As a whole, the loop is not isotropic and has a ''pancake'' shape. In addition, it has a total polarization $\langle\int\mathbf{s}_j'(\xi_j)\times\mathbf{s}_j''(\xi_j)d\xi_j\rangle$, forcing the loop to drift along the vector $\mathbf{V}_n$ and to produce nonzero superfluid mass flow in the $z$ direction (Sec. 3).

$$N_{\text{allowed}}\propto\prod_j\int\mathscr{D}(\{\mathbf{s}_j(\xi)\})\cdot\text{constants}\{\mathbf{s}_j(\xi)\}. \tag{3}$$

The constraints entering this relation are expressed by delta functions that give fixed properties of the VT. For instance, the constraint $\delta((\mathbf{s}_j'(\xi)^2-1)$ shows that the parameter $\xi$ is the arc length. However, this condition leads to an intractable theory. We will use a trick known from the theory of polymer chains (see, e.g., Ref. 7); namely, we will relax the rigorous condition and change the delta function by continuous (Gaussian) distribution of the link length with the same value of integral. This trick leads to the expression for the number of allowed configurations

$$N_{\text{allowed}}\propto\prod_j\int\mathscr{D}(\{\mathbf{s}_j(\xi)\})\exp\left(-\lambda_1\int_0^{\mathscr{L}}\left|\mathbf{s}'\right|^2d\xi\right). \tag{4}$$

In the same manner we are able to introduce other known properties of the VT structure. The detailed calculations will be published elsewhere.[8] We can now write the final expression for the probability of configurations

$$N_{\text{allowed}}\propto\int\mathscr{D}\{\mathbf{s}(\kappa)\}\exp(-\mathscr{L}\{\mathbf{s}(\kappa)\}). \tag{5}$$

Here $\mathbf{s}(\kappa)$ is a one-dimensional Fourier transform[1)] of the variable $\mathbf{s}(\xi)$, and the Lagrangian $\mathscr{L}\{\mathbf{s}(\kappa)\}$ is

$$\mathscr{L}\{\mathbf{s}(\kappa)\}=\sum_{\kappa\neq0}\mathbf{s}_x^{\alpha}(\kappa)\Lambda^{\alpha\beta}(\kappa)\mathbf{s}_x^{\beta}(\kappa). \tag{6}$$

In practice, to calculate various averages it is convenient to work with the characteristic (generating) functional (CF), which is defined as the average

$$W(\{\mathbf{P}_j(\kappa)\})=\left\langle\exp\left(-\sum_j\sum_{\kappa\neq0}\mathbf{P}_j^{\mu}(\kappa)\mathbf{s}_j'^{\mu}(-\kappa)\right)\right\rangle.$$

Accordingly, our Lagrangian has a quadratic form [in $\mathbf{s}(\kappa)$]. Consequently, the trial distribution function is a Gaussian function, calculation of the CF can be made by using a full square procedure to give the result

$$W(\{\mathbf{P}_j(\kappa)\})=\exp\left(-\sum_j\sum_{\kappa\neq0}\mathbf{P}_j^{\mu}(\kappa)N_j^{\mu\nu}(\kappa)\mathbf{P}_j^{\nu}(-\kappa)\right). \tag{7}$$

The elements of the matrix $N_j^{\mu\nu}(\kappa)$ are specified from calculation of the total length, anisotropy coefficient, curvature, and polarization. Their explicit form is written in Ref. 8. The typical shape of the averaged curve is shown in Fig. 2.

Thus we reached our goal and have written the expression for the trial CF, which enables us to calculate any average vortex filament configuration.

### 3. HYDRODYNAMIC IMPULSE OF THE VORTEX TANGLE

As an illustration of the developed theory we would like to discuss hydrodynamic impulse of vortex tangle $\mathbf{J_V}$ which is defined as

$$\mathbf{J_V}=\left\langle\frac{\rho_s\overline{\kappa}}{2}\sum_j\int\mathbf{s}_j(\xi_j)\times\mathbf{s}_j'(\xi_j)d\xi_j\right\rangle. \tag{8}$$

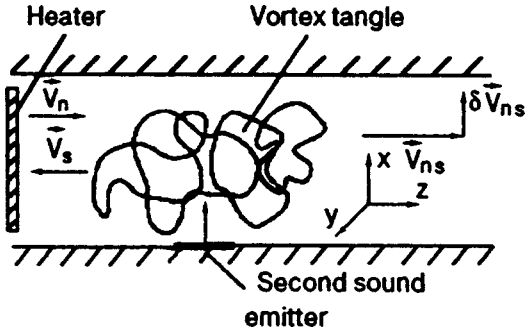


FIG. 3. Illustration of the transverse experiment. Small perpendicular deviation $\delta\mathbf{V}_{ns}$ of the counterflow velocity $\mathbf{V}_{ns}$ changes the orientation of polarization of the vortex tangle, whereas the vortex line density and mean curvature do not change in the first order in $\delta\mathbf{V}_{ns}$.

The quantity $\mathbf{J}_\mathbf{V}$ is closely related to the momentum of the fluid (see Ref. 9). The averaged $\langle \mathbf{s}_j(\xi_j)\times\mathbf{s}_j'(\xi_j)\rangle$ is immediately evaluated by CF (7) to give the result

$$\mathbf{J}_\mathbf{V}^z = -\left[\frac{\rho\tilde{\kappa}I_l\alpha_v}{\rho_n c_2^2\beta_v}\right]\rho_s\mathbf{V}_s. \tag{9}$$

Note that the coefficient includes no fitting parameters but only the characteristics known from the phenomenological theory (see Ref. 6). The relation (9) shows that the vortex tangle induces the superfluid current directed against the external superfluid current. This should be expected since there is a preferable polarization of the vortex loops. In the experiments this additional superfluid current manifests itself as a suppression of the superfluid density. This effect is a $3D$ analog of the well-known Kosterlitz–Thouless effect except that distribution of the vortex lines is not calculated but is written with reference to the experimental data.

Since superfluid density enters the expression for second-sound velocity, it seems attractive to detect it using transverse second sound testing (Fig. 3). To do this, we must first evaluate transverse change of the $\rho_s$ and, secondly, develop the theory to match it to the nonstationary case. The general theory asserts that while applying a harmonic external second-sound field, suppression of superfluid density becomes a function of frequency $\omega$ in the form

$$\Delta\rho_s^x(\omega) = \left(\frac{\delta\mathbf{J}_V^x}{\delta\mathbf{V}_s^x}\right)_{\text{transv}} \frac{1}{1+i\omega\tau_J}. \tag{10}$$

Here the transverse $(\delta\mathbf{J}_V^x/\delta\mathbf{V}_s^x)_{\text{transv}}$ is half that given by relation (9). The quantity $\tau_J$ is the time of relaxation of the superfluid current $J_V$, which can be found from dynamical considerations. Expressing $d\mathbf{J}_V^x/dt$ with the help of the equation of motion of the vortex line elements and then evaluating various averages by our trial distribution function, we obtain the following final result for the change of the second-sound velocity.

Performing all of the described procedures, we find that the relative change is

$$\Delta u_2/u_2 = -f(T)(\mathbf{V}_{ns}^4/\omega^2). \tag{11}$$

Here the function $f(T)$ consists of the structure parameters of the vortex tangle

$$f(T) = \frac{4\rho\tilde{\kappa}I_l^2\alpha^2(4-I_{xx})^2}{\rho_n c_2^4\beta^3}. \tag{12}$$

Decreasing the second-sound velocity in the counterflowing He-II has been actually observed about two decades ago by Vidal *et al.*[10] To the best of our knowledge, there was only an attempt to consider this effect theoretically by Mehl,[11] who explained the change in the second-sound velocity by introducing the imaginary part into the Hall–Vinen constant. However, aside from some numerical disagreement, the Mehl's theory did not explain the strong $\mathbf{V}_{ns}$ dependence in the experimental data. Let us compare our result (11) with Vidal's experiment. Using the data on the structure parameters, we find that, e.g., at the temperature 1.44 K the value of the function $f(T)$ is about $620\ \text{s}^2/\text{cm}^4$. Using the frequency $\omega = 4.3$ rad/s in Ref. 10 and $V_{ns} = 2$ cm/s, we find that $\Delta u_2/u_2 \approx 4\times10^{-4}$, which is very close to the observed value.

#### 4. ENERGY OF THE VORTEX TANGLE

In this section we calculate the average energy of the stochastic vortex loop distributed according to the distribution function (5). The general expression associated with the linear vortices can be written as follows (see, e.g., Ref. 9):

$$E = \left\langle \frac{1}{2}\int \rho_s\mathbf{v}_s^2 d^3\mathbf{r}\right\rangle = \left\langle \frac{\rho_s\kappa^2}{8\pi}\sum_{j,i}\int_0^{L_i}\int_0^{L_j}\frac{\mathbf{s}_i'(\xi_i)\mathbf{s}_j'(\xi_j)}{|\mathbf{s}_i(\xi_i)-\mathbf{s}_j(\xi_j)|}\,d\xi_i d\xi_j\right\rangle. \tag{13}$$

In $3D$ Fourier space the average energy $E$ (13) can be rewritten as

$$E = \left\langle \frac{\rho_s\kappa^2}{2}\sum_{i,j}\int_{\mathbf{k}}\frac{d^3\mathbf{k}}{(2\pi)^3\mathbf{k}^2}\int_0^{L_i}\int_0^{L_j}\mathbf{s}_j'(\xi_i)\mathbf{s}_j'(\xi_j) \times d\xi_i d\xi_j\,\exp\big(i\mathbf{k}(\mathbf{s}_i(\xi_i)-\mathbf{s}_j(\xi_j))\big)\right\rangle. \tag{14}$$

Comparing (14) and (7), it is possible to express the energy $E$ in terms of the characteristic functional:

$$\langle E\rangle = \frac{\rho_s\kappa^2}{2}\sum_{i,j}\int_{\mathbf{k}}\frac{d^3\mathbf{k}}{(2\pi)^3\mathbf{k}^2}\int_0^{L_i}\int_0^{L_j}d\xi_i d\xi_j \times\frac{\delta^2 W}{i\,\delta\mathbf{P}_i^\alpha(\xi_i)\,i\,\delta\mathbf{P}_j^\alpha(\xi_j)}\,\exp[i\mathbf{k}(s_i(0)-s_j(0))]. \tag{15}$$

Here the set of $\mathbf{P}_n(\xi_n')$ in CF $W(\{\mathbf{P}_n(\xi_n')\})$ is again determined with the help of the $\theta$-functions

$$\mathbf{P}_i(\xi_i') = \mathbf{k}\theta(\xi_i')\,\theta(\xi_i-\xi_i'), \quad \mathbf{P}_j(\xi_j') = \mathbf{k}\theta(\xi_j')\,\theta(\xi_j-\xi_j'),$$
$$\mathbf{P}_n(\xi_n) = 0, \quad n\neq i,j. \tag{16}$$

The relation (16) implies that we choose in the integrand in the exponent of CF only the points lying in the interval from 0 to $\xi_i$ on the $i$-curve and from 0 to $\xi_j$ on the $j$-curve. In the evaluation of self-energy of the same loop, $i=j$, one has to distinguish the points $\xi_i$, and assume them to be, e.g., $\xi_i'$ and $\xi_i''$. Further results concern the case of the only loop of length $L$. Omitting cumbersome calculations, we write the final result in the form

$$E=\frac{\rho\kappa^2 L}{4\pi}\ln\frac{R}{a_0}+\frac{\rho\kappa^2 L}{4\pi}\left(1-\frac{2}{\sqrt{4}}(f_2-f_1)\right)\ln\frac{R}{a_0}$$
$$+\frac{\rho\kappa^2 L}{4\pi}\left[\frac{2f_3}{(\sqrt{\pi}-1)^{1/2}\pi^{5/2}c_{23}^2}I_l^2+\frac{f_2}{\pi^{3/2}(\sqrt{\pi}-1)^{1/2}}\right], \tag{17}$$

where the quantities $f$ are expressed in terms of the structure parameters of the VT as follows:

$$f_1(\beta)=[2(3-\beta^2)]^{1/2}\frac{\arcsin\beta}{\beta}, \tag{19}$$

$$f_2(\beta)=\frac{1}{[2(3-\beta^2)]^{1/2}}$$
$$\times\left(-\sqrt{1-\beta^2}+(2-\beta^2)\frac{\arcsin\beta}{\beta}\right), \tag{20}$$

$$f_3(\beta)=[2(3-\beta^2)]^{3/2}\left(\frac{\sqrt{1-\beta^2}}{\beta^2}-\frac{\arcsin\beta}{\beta^3}\right),$$

$$\beta=\sqrt{(I_x-I_z)/I_x}. \tag{21}$$

Let us examine expression (17). The first term on its right side is the energy per unit length of the straight vortex filament (see, e.g., Ref. 1) multiplied by its length. In this form it is frequently used in the theory of superfluid turbulence (see, e.g., Ref. 3). But there are additional terms. The second term is also logarithmically large. We assume that this contribution comes from accidental self-crossing of remote (along the line) parts of the vortex filament. The third and fourth terms result from long-range interaction; they are smaller (about 10%) than the logarithmic terms. The third term is of special interest. It appears due to the polarization of the vortex loop and its presence implies that there is some elasticity of the vortex tangle in the $\mathbf{V}_{ns}$ direction. The results of the previous section show that the presence of the VT leads to the appearance of a correction of the superfluid density. Therefore, combination of the longitudinal elasticity and inertia of the ''joint'' mass should lead to the appearance of elastic waves, $3D$ analog of the Tkachenko waves.

## 5. CONCLUSION

Based on the trial distribution function in the space of vortex loops comprising a superfluid turbulence in He-II a hydrodynamic impulse, as well as energy of vortex tangle. Some dynamic properties of the turbulent He-II, due to the impulse and energy of vortex configuration such as suppression of the superfluid density and decrease in the velocity of the second sound that, propagate in the superfluid turbulent He-II, have been discussed.

This work was funded in part by the Russian Fund for Fundamental Research, Grant No. 96-02-19414.

*E-mail: nemirov@otani.thermo.nsk.su

[1)]We used $1D$ Fourier transform $\mathbf{s}_j(\kappa)$ of curves $\mathbf{s}_j(\xi)$ since various properties of the VT, such as the mean curvature, polarization, anisotropy, etc., are expressed via the derivatives of $\mathbf{s}_j(\xi)$ of different orders.

[1] R. J. Donnely, *Quantized Vortices in Helium II*, Cambridge University Press (1991).
[2] J. T. Tough, in *Progress in Low Temperature Physics*, D. F. Brewer (Ed.), North Holland (1982), p. 133.
[3] S. K. Nemirovskii and W. Fiszdon, Rev. Mod. Phys. **67**, No. 1, 37 (1995).
[4] R. P. Feynman, in *Progress in Low Temperature Physics*, C. J. Gorter (Ed.), North Holland (1955), vol. 1, p. 17.
[5] W. F. Vinen, Proc. R. Soc. London, Ser. A **240**, 114 (1957); *ibid.* **240**, 128 (1957); *ibid.* **242**, 493 (1957); *ibid.* **243**, 400 (1958).
[6] K. W. Schwarz, Phys. Rev. B **18**, 245 (1978); *ibid.* **31**, 5782 (1985); *ibid.* **38**, 2398 (1988).
[7] M. Doi and S. F. Edwards, *The Theory of Polymer Dynamics*, Clarendon Press, Oxford (1986).
[8] S. K. Nemirovskii, Czech. J. Phys. Vol. 46 (Suppl. S1) (1996); Phys. Rev. B (submitted).
[9] G. K. Batchelor, *An Introduction to Fluid Mechanics*, Cambridge University Press (1967).
[10] F. C. Vidal, C. R. Acad Sci. **B275**, 609 (1972).
[11] J. B. Mehl, Phys. Rev. A **10**, 601 (1974).

This article was published in English in the original journal. It was edited by S. J. Amoretty.

# Helium flow in a confined region caused by heating under zero gravity: approaches based on molecular kinetics and mechanics of continuous media

A. A. Gorbunov and V. I. Polezhaev

*Institute for Problems in Mechanics, Russian Academy of Sciences, 117526 Moscow, Russia**

A. P. Kryukov and I. N. Shishkova

*Moscow Power Engineering Institute, 111250 Moscow, Russia***
Fiz. Nizk. Temp. **24**, 132–135 (February 1998)

Helium flow in an enclosure caused by sudden heating of the enclosure walls is considered. Boltzmann's equation and complete time-dependent Navier–Stokes equations with appropriate boundary conditions are integrated numerically. It is shown that the results of calculations obtained by using these methods for a steady-state flow are close. © *1998 American Institute of Physics.* [S1063-777X(98)00802-0]

## INTRODUCTION

Heat- and mass transfer at low temperatures can take place under the conditions when the temperature of a heating surface differs considerably from the temperature of a cryogen in contact with this surface. Film boiling of helium is an example of such a process. Film boiling is observed in superfluid helium (HeII) for large values of heat flux. The temperature of the heater and HeII differ by one or even two orders of magnitude in this case. Such conditions are responsible for considerable deviations from equilibrium and complicate an analysis of corresponding transport processes.

In this communication, we analyze heat transfer in the vapor region confined by surfaces with considerably differing temperatures. The molecular-kinetic approach based on the solution of Boltzmann's equation can be used for this purpose. Although this method is cumbersome, it is free of limitations associated with the extent of departure from equilibrium in transport processes.[1,2] At the same time, methods and mathematical apparatus have been developed for problems of mechanics and heat transfer in a continuous compressible medium.[3] These approaches were successfully tested and used for a number of problems.[1–5] Our main task is to determine the extent of matching of the results obtained by different methods and to find the region of applicability of these methods for helium flow in an enclosure.

## FORMULATION OF THE PROBLEM

Let us consider an enclosure confined between two parallel planes (henceforth referred to as enclosure walls) and filled with a stationary gas under zero gravity conditions. We denote the temperature and density of the gas by $T_m$ and $\rho_m$. For definiteness, we refer to these planes as the left and right wall, assume that the walls are rigid and unpenetrable, and suppose that, starting from a certain instant of time, the temperatures of the left and right walls in the absence of heat sources in the bulk have the values $T_l = 4$ K and $T_r = 2$ K, respectively.

In the space containing the enclosure, we introduce a system of Cartesian coordinates whose origin lies on the left wall, and the $x$-axis is directed to the right wall. If we consider a fragment of the enclosure confined additionally by a pair of parallel planes, we assume that one of the additional planes (referred to as the lower wall) passes through the $x$-axis, and the $y$-axis is directed towards the other additional plane (referred to as the upper wall). We denote by $L$ the separation between the left and right walls and by $H$ the separation between the upper and lower walls.

In the two-dimensional case, we assume that the upper and lower walls are also rigid and impermeable and that a linear temperature distribution is maintained at these walls.

Further, assuming for simplicity that $L = H$ and $T_r = T_m$, we put $\rho_m = 0.76$ kg/m$^3$ and $T_m = 2$ K for density and temperature scales, respectively and choose $L = 0.5 \times 10^{-6}$m for the scale of length.

## BASIC EQUATIONS AND METHODS OF SOLUTION

### Molecular-Kinetic Approach

Boltzmann's kinetic equation (BKE) in a time-dependent two-dimensional problem has the form

$$\frac{\partial f}{\partial t} + \xi_x \frac{\partial f}{\partial x} + \xi_y \frac{\partial f}{\partial y} = J, \tag{1}$$

where $f = f(\xi, x, y, t)$ is the molecular velocity distribution function, $\xi$ the velocity vector of a particle (helium atom), $x$ and $y$ are the coordinates along the $x$- and $y$-axes, $t$ is the time, and

$$J = \int_\Omega ( f' f_1' - f f_1) |\xi - \xi_1| b \, d\Omega$$

denotes the collision integral. In writing the expression for the collision integral, we have used the notation introduced by Kogan.[6]

The solution of Eq. (1) leads to the molecular velocity distribution function. Macroscopic parameters (such as density, temperature, pressure, mass and energy fluxes) are determined as moments of the distribution function.

We believe that the method of direct numerical solution of Boltzmann's equation used here is one of the most rigorous methods. A detailed description of this method can be found, for example, in Ref. 1.

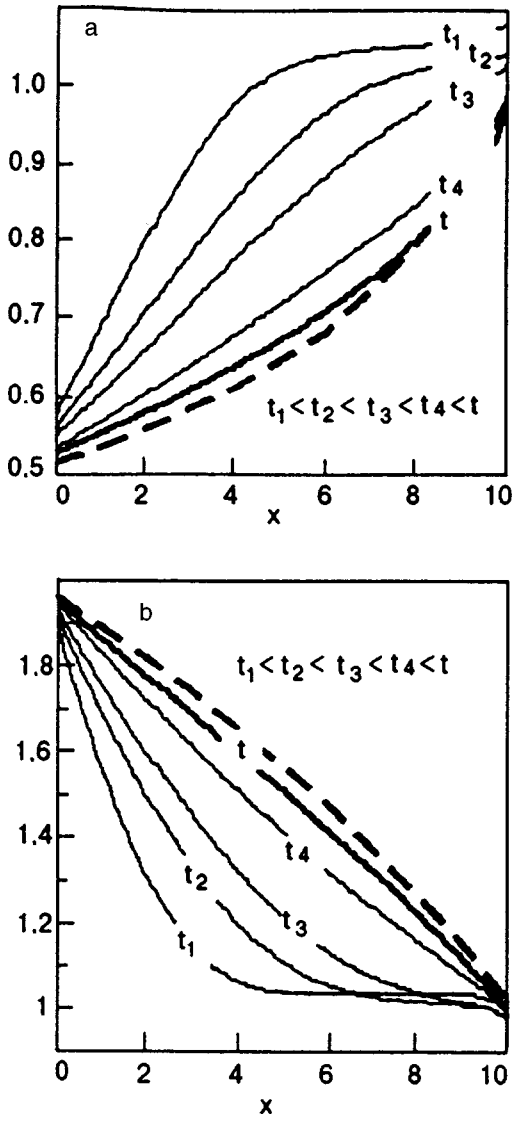


FIG. 1. Time variation of density (a) and temperature (b) profiles for a film of thickness $10L$ for $H \gg L$: direct numerical solution of BKE (solid curves) and moments method of solution of BKE (dashed curves).

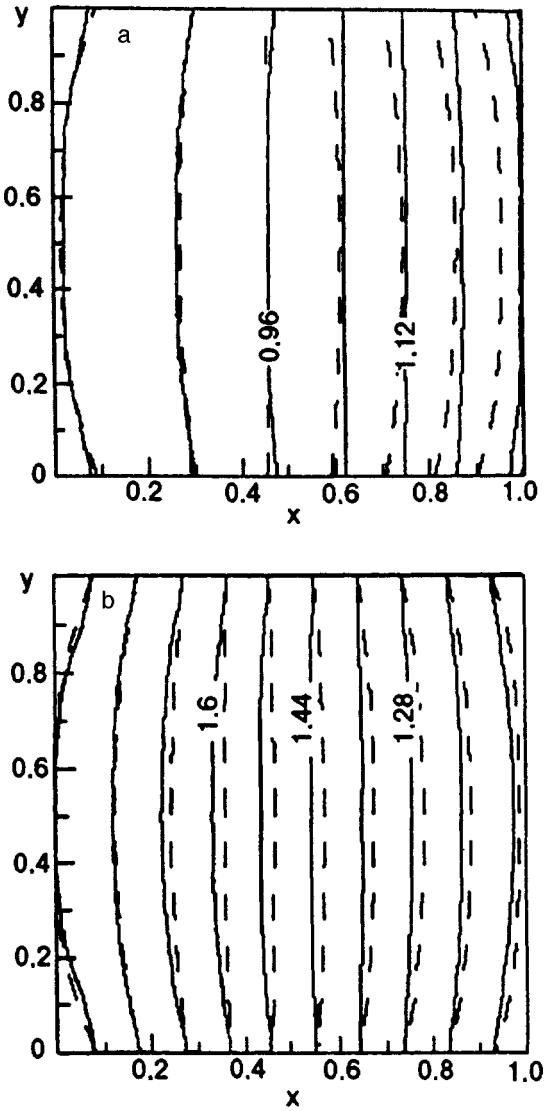


FIG. 2. Isolines of density (a) and temperature (b) for a steady-state flow: molecular-kinetic approach (solid curves) and the approach based on continuous media mechanics (dashed curves).

In formulating the boundary conditions, we assume that complete energy accommodation of molecules takes place at the enclosure walls, and the molecules are reflected diffusely. Thus, the distribution function for reflected particles is a semi-Maxwellian with zero transport velocity. The density of such a distribution is determined from the zero- flow condition, i.e., from the condition of equality of impinging and reflected mass fluxes. The intermolecular interaction potential is taken as for elastic spheres.

#### Approach Based on Continuous Media Mechanics

We shall describe the flow of the gas by the system of dynamic equations for a viscous gas, including the Navier–Stokes equations of motion, the energy balance equation, and the continuity equation, assuming that the equation of state for the gas is determined by the Clapeyron formula (see, for example, Ref. 7).

For simplicity, we consider the one-dimensional case and write the dimensionless system of dynamic equations for a viscous gas for the appropriate choice of scales of dimensional variables and corresponding normalization in the form

$$\frac{\partial U}{\partial t} + L_c(U)\frac{\partial U}{\partial x} + \frac{1}{\mathrm{Re}_c} L_w(U)\frac{\partial U}{\partial x} + \frac{1}{\mathrm{Re}_c^2} L_d(U)\frac{\partial^2 U}{\partial x^2} = 0, \quad (2)$$

where $t$ is the time, $U$ the vector of required variables whose components are the velocity and normalized Napierian logarithms of dimensionless density and temperature, the matrix $L_c(U)$ defines convective derivatives, the matrix $L_w(U)$ specifies the wave and dissipative properties, the matrix $L_d(U)$ characterizes diffusion, and $\mathrm{Re}_c$ is Reynolds number for the velocity of sound.

The initial and boundary conditions for velocity and temperature follow from the formulation of the problem, and the value of density at the boundary is determined from the continuity equation.

The system of Eqs. (2) can be solved numerically by the method based on the finite-difference approximation of this system (see Refs. 3 and 5).

## DISCUSSION OF RESULTS

The results of solution of one-dimensional problems for a steady-state flow show that the coordinate dependences of density and temperature obtained on the basis of molecular-kinetic approach and the approach based on the mechanics of continuous media are close.

The molecular-kinetic approach allows us to analyze flows with evaporation–condensation along with the solution of problems with impenetrable interfaces. Figure 1 illustrates the solution of such a problem in which the right wall is the superfluid helium–vapor interface.

Figure 2 shows isolines for temperature [Fig. 2(a)] and density [Fig. 2(b)] fields for a gas with a steady-state flow in the cavity under investigation for two-dimensional problems. Solid curves correspond to the molecular-kinetic approach, while the dashed curves correspond to the approach based on the mechanics of continuous media. It can be seen that these methods give virtually identical results.

A comparison of the results of the solution of one- and two-dimensional problems shows that in spite of the small size of enclosures in the flows under investigation, both the molecular kinetic method and the equations for a continuous medium can be used for an analysis of such regions. The equations for a continuous medius are solved with the boundary conditions obtained by molecular-kinetic methods (e.g., the values of temperature jumps at phase boundaries).

In conclusion, we can propose the following recommendations for an analysis of heat transfer in gaseous helium under strongly nonequilibrium conditions.

(1) At the initial stage of the solution of the problem, temperature jumps at interfaces should be determined with the help of the molecular-kinetic method. In the case of small and moderate values of heat fluxes, there is no need to obtain new kinetic solution since the well-known tested relations can be used (see, for example, Ref. 8).
(2) The internal region of the flow can be analyzed to a high degree of accuracy by using the methods of mechanics of continuous media.
(3) Under strongly nonequilibrium conditions, the kinetic approach becomes essential. Thus, for large heat fluxes observed, for example, for boiling of superfluid helium, calculations without kinetic solutions can lead to considerable errors. Some problems such as that involving evaporation–condensation cannot be formulated correctly without using the molecular-kinetic approach.

This research was carried out under the RFFI project No. 97–01–00124 and the project TM–16 of the contract NAS 15–10110 between NASA and Russian Space Agency.

*E-mail: polezh@ipmnet.ru
**E-mail: kryukov@kryos.mpei.ac.ru

[1] V. V. Aristov and F. G. Tcheremissine, *Direct Numerical Solution of the Boltzmann Kinetic Equation* [in Russian], Computing Center of Russian Academy of Sciences, Moscow (1992).
[2] V. V. Aristov, A. P. Kryukov, F. G. Tcheremissine, and I. N. Shishkova, Zh. Vychisl. Mat. Mat. Fiz. **30**, 1093 (1991).
[3] V. I. Polezhaev, Izv. Akad. Nauk SSSR, MZhG, No. 2, 103 (1967).
[4] A. P. Kryukov and I. N. Shishkova, *Book of Abstracts, 20th Int. Symp. on Rarefied Gas Dynamics*, Beijing, China, August 19–23 (1996).
[5] A. A. Gorbunov, Izv. RAN, MZhG, No. 3, Seminars (1997).
[6] M. N. Kogan, *Rarefied Gas Dynamics* [in Russian], Nauka, Moscow (1967).
[7] L. G. Loitsyanskii, *Fluid Mechanics* [in Russian], Nauka, Moscow (1987).
[8] T. M. Muratova and D. A. Labuntsov, Teplofiz. Vys. Temp. **7**, 959 (1969).

Translated by R. S. Wadhwa

# Adsorption of gaseous helium near $T_\lambda$ at low pressures

G. V. Kachalin, A. P. Kryukov, and S. B. Nesterov

*Moscow Power Engineering Institute (Technical University), 111250 Moscow, Russia*[*]
Fiz. Nizk. Temp. **24**, 136–139 (February 1998)

Cryosorption of helium isotopes ($^3$He and $^4$He) on thin layers of solid argon at low gas pressures in the bulk is studied experimentally upon a change in the layer temperature from 4.2 to 2 K. It is shown that the sorption isostere for $^4$He displays anomalous behavior near the temperature $T_\lambda$ of transition of liquid $^4$He into superfluid state. An abrupt change in pressure is observed for a $^4$He film thickness corresponding approximately to two monolayers. In experiments on cryosorption of gaseous $^3$He on an argon layer for a $^3$He film thickness corresponding approximately to one monolayer, the pressure in the bulk varies monotonically over the entire temperature interval. © *1998 American Institute of Physics.* [S1063-777X(98)00902-5]

## INTRODUCTION

A large number of works have been published in recent years on the properties of thin helium layers adsorbed on various porous substances like glass, silicagels, aerogels, and zeolites.[1–8] However, the adsorption of gaseous helium on a solid surface has not been studied extensively for a low initial pressure of gaseous helium.

The present paper aims at studying the behavior of sorption isosteres for helium isotopes on argon cryolayers at temperatures close to the point $T_\lambda$ of transition of liquid $^4$He into superfluid state.

## EXPERIMENTAL TECHNIQUE

Experiments on studying the cryosorption of helium near $T_\lambda$ were carried out on a high-vacuum setup on which measurements could be made at low temperatures. The schematic diagram of the experimental set-up is shown in Figs. 1(a) and 1(b).

The main element of the setup is a cryoblock consisting of a commercial helium cryostat KG-60/300-1 and containing a vacuum module. The vacuum module is a copper sphere of diameter 270 mm and wall thickness 1 mm [Fig. 1(a)] or a cylinder with a detachable cryopanel [Fig. 1(b)].

The use of a spherical module is dictated by the need to ensure a uniform deposition of the sorbent layer on the surface of the cryopanel. However, on account of the hydrostatic pressure under terrestrial conditions, the lambda transition in the upper part of the sphere occurs at a slightly higher temperature than in the lower part. Such a temperature difference along the cryopanel can be avoided by using a cylindrical module with a plane cryopanel. However, a uniform deposition of the sorbent cannot be ensured in this case. A brief analysis carried out by us reveals that a uniform sorbent layer can be deposited near the lambda point under ideal isothermal conditions not only in our experiments, but in principle if precise temperature measurements are made in a spherical module under zero gravity conditions.

The vacuum module is evacuated preliminarily through the connecting tube from an external station consisting of a turbomolecular pump VMN-150 and a mechanical pump 2NVR-5DM. Liquid helium is then introduced into the cryostat, and its level in the bath is controlled by level indicators made of a superconducting wire.

The sorbent (argon in the present case) cryolayer is formed as a result of condensation of the gas on the inner surface of the vacuum module. The gas is supplied through the inlet tube equipped with an atomizer consisting of three layers of a 64-$\mu$m mesh, which allows the formation of a cryolayer of uniform thickness. Gaseous helium is let in after the formation of a cryolayer of given thickness. The helium concentration is determined in relative units $C=(V_{\mathrm{He}}/V_{\mathrm{Ar}})\cdot 100\%$, where $V_{\mathrm{He}}$ and $V_{\mathrm{Ar}}$ denote the volume of gaseous helium and argon respectively under normal conditions.

After the equilibrium pressure has been established in gaseous helium over the cryolayer, the sorption isostere is determined at 4.2 K, i.e., the dependence $\ln P=f_c(1/T)$ (where $P$ is the helium pressure over the cryolayer and $T$ is the temperature of the cryolayer) is investigated for a constant helium concentration in the bulk of the module. The pressure $P$ is determined with the help of ionization pressure transducers LM-3-2, and the bath temperature $T$ is varied by pumping vapor of liquid helium surrounding the vacuum module. The value of $T$ is determined from the saturated vapor pressure of liquid helium which is measured by a mercury cup manometer, and is controlled by the readings of resistance thermometers fastened to the outer wall of the vacuum chamber.

The sorption isostere in $\ln P$ vs. $T^{-1}$ coordinates is a straight line whose slope gives the value of the heat of sorption.

## DISCUSSION OF EXPERIMENTAL RESULTS

Figure 2 shows the experimental dependences $\lg P=f_c(1/T)$ obtained while measuring the sorption of helium isotopes $^3$He and $^4$He on argon cryolayers formed under identical conditions (spherical module).

It can be seen from the figure that near the phase transition point $T_\lambda=2.172$ K of $^4$He into superfluid state in the outer bath, the pressure $P$ of gaseous $^4$He over the cryolayer decreases abruptly by a factor of $\sim 2$ (see the isostere for $C=10.16\%$).

In the same temperature interval, the pressure of gaseous $^3$He varies monotonically with decreasing temperature, and

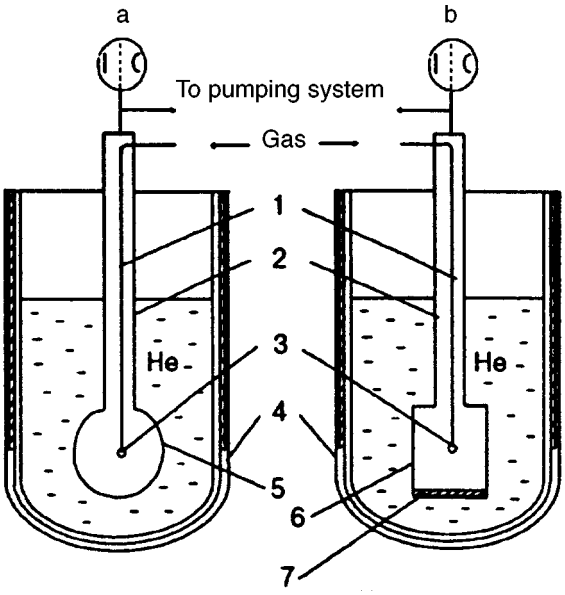


FIG. 1. Spherical (a) and cylindrical (b) experimental modules. gas inlet tube (*1*), connecting pipeline (*2*), atomizer (*3*), helium cryostat (*4*), hollow sphere (*5*), hollow cylinder (*6*), and cryopanel (*7*).

hence the sorption isostere of $^3$He for $C=4.81\%$ is described by a straight line. Thus an analysis of Fig. 2 reveals that the observed pressure jump is characteristic of the system argon–$^4$He for $C=10.16\%$.

In order to interpret the obtained experimental data, we must know the properties of the absorbing substrate, including the helium concentration $C$ for which a helium monolayer is formed on the surface of solid argon, i.e., the capacity of the monolayer. In order to determine the latter, we used the Langmuir equation, the Brunauer–Emmett–Teller (BET) equation, and the Dubinin–Radushkevich–Kaganer (DRK) equation.[9–12] The knowledge of the monolayer capacity is essential for understanding the processes occurring at the surface of a cryolayer upon a decrease in temperature.

TABLE I. Helium concentration $C$ in argon for which a monolayer of helium is formed at the solid argon surface.

| | Concentration, % | |
|---|---|---|
| Equation | $^4$He | $^3$He |
| DRK | 4.94 | 5.3 |
| Langmuir | 6.09 | 4.81 |
| BET | 5.84 | 4.81 |

In the concentration range 3.40–5.87% for $^4$He and 4.00–4.81% for $^3$He, all three equations (Langmuir, BET and DRK) describe the experimental dependences $P(T)$ quite satisfactorily.

Calculated values of the capacity of argon monolayer for sorption of $^4$He and $^3$He are presented in Table I. It can be seen that the values of the monolayer capacity $C_m$ determined by various methods for $^4$He and $^3$He on argon are quite close and lie in the range 4.94–6.09% for $^4$He and 4.81– 5.30% for $^3$He. It follows hence that the thickness of $^4$He film on argon surface under conditions when a pressure discontinuity is observed on the straight line $\ln P=f(1/T)$ in the vicinity of $T_\lambda$ corresponds to about two monolayers.

The abrupt decrease in the pressure of gaseous $^4$He in the working volume as a result of cooling of the liquid below $T_\lambda$ can be explained as follows.

It is well known[5] that even thin films of helium formed on a solid surface as a result of sorption are quite mobile in contrast to the adsorbed layers of other gases. It was shown by McCormick *et al.*[6] that an argon layer deposited on a copper surface has a very high thermal conductivity and effectively removes the heat released during adsorption of helium. Studies by Chan *et al.*[7] revealed that the temperature of transition to the superfluid state for helium contained in the pores of sorbents like aerogel is 2.167 K, i.e., close to the value of $T_\lambda$ for the bulk liquid. According to the experimental results presented in a recent publication by Kubota *et al.*,[8]

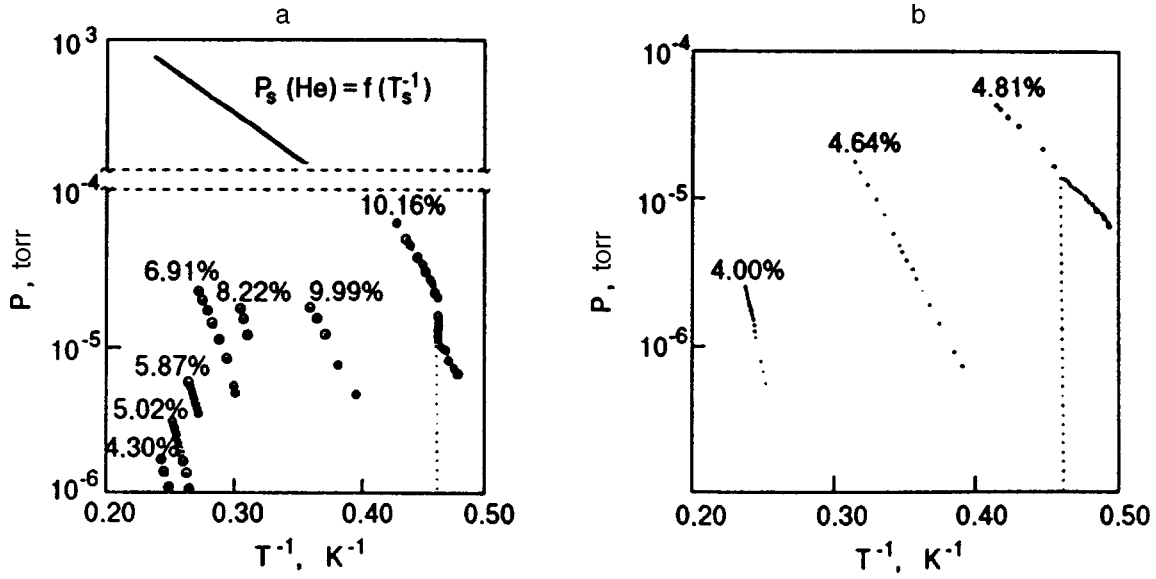


FIG. 2. Isosteres of sorption of $^4$He (a) and $^3$He (b) on argon cryolayer for various helium concentrations $C$(%).

the thermal conductivity of unsaturated helium films on the surface of porous glass increases sharply (by four orders of magnitude) upon an increase in the concentration of $^4$He atoms at the surface or a decrease in the substrate temperature. In particular, such a jump is observed[8] at about 1.1 K for a concentration of 34.7 $\mu$mole He/m$^2$.

In the light of the experimental data presented above, a sharp decrease in the pressure of gaseous $^4$He over the argon layer upon a cooling of the working volume below $T_\lambda$ can be attributed to a considerable increase in the mobility of helium film adsorbed on the argon surface and penetration of helium into tiny pores. This increases the sorption capacity of the sorbent layer and hence to a displacement of dynamic equilibrium towards decreasing volume concentration of $^4$He atoms in the gas above the cryolayer. A practically constant value of slope of the isosteres before and after the pressure jump indicates that the heat of sorption remains unchanged after filling of the microscopic pores.

## CONCLUSIONS

(1) During cryosorption of $^4$He on a layer of solid argon, the sorption isosteres display anomalous behavior in the region of phase transition of the liquid in the bulk, which is manifested in the form of an abrupt variation in the pressure over the cryolayer. Analysis of the data in coordinates of Langmuir, Brunauer–Emmett–Teller and Dubinin–Radushkevich–Kaganer equations shows that the anomalous behavior is observed for a helium film thickness of about two monolayers.

(2) During cryosorption of $^3$He on a layer of solid argon formed under identical conditions for a capacity of about one monolayer, no sharp variation is observed in pressure over the cryolayer in the vicinity of $T_\lambda$ for $^4$He in the bulk.

This research was carried out under the project TM-16 in accordance with the contract NAS 15-10110 between NASA and the Russian Space Agency.

*E-mail: kryukov@kryos.mpei.ac.ru

[1] L. S. Gurevich, S. B. Nesterov, A. P. Kryukov, and A. I. Bychkov, Plasma Devices Op. **1**, 247 (1991).
[2] S. B. Nesterov and A. P. Kryukov, Vopr. At. Nauki Tekhn., Ser. Termoyad. Sintez, **134**(?) (1994).
[3] E. Wallen, J. Vac. Sci. Technol. **15(2)**, 265 (1997).
[4] S. B. Nesterov and A. P. Kryukov, Vacuum (to be published).
[5] F. D. Manchester, Rev. Mod. Phys. **39**, 383 (1967).
[6] W. D. McCormick, D. L. Goodstein, and J. G. Dash, Phys. Rev. **168**, 249 (1968).
[7] M. H. W. Chan, K. I. Blum, S. Q. Murphy *et al.*, Phys. Rev. Lett. **61**, 1950 (1988).
[8] M. Kubota, T. Yano, T. Iida *et al.*, Czech. J. Phys. **46**, 437 (1996).
[9] I. Langmuir, J. Am. Chem. Soc. **40**, 1361 (1918).
[10] S. Brunauer, P. H. Emmett, and E. Teller, J. Am. Chem. Soc. **60**, 309 (1938).
[11] M. M. Dubinin and L. V. Radushkevich, Proc. Acad. Sci. USSR **55**, 327 (1947).
[12] M. G. Kaganer, Proc. Acad. Sci. USSR **116**, 603 (1957).

Translated by R. S. Wadhwa